NASA CR-159088

Analysis of Vibratory Excitation of Gear Systems as a Contributor to Aircraft Interior Noise

by

William D. Mark

February 1979

Prepared Under Contract No. NAS1-14611

by

Bolt Beranek and Newman Inc.
Cambridge, Mass. 02238

for

NASA

National Aeronautics and
Space Administration
Langley Research Center
Hampton, VA 23665

NASA CR 159088

Technical Memorandum No. 502

ANALYSIS OF VIBRATORY EXCITATION OF GEAR SYSTEMS AS A CONTRIBUTOR TO AIRCRAFT INTERIOR NOISE

William D. Mark

February 1979

Contract No. NAS1-14611 - 16

Prepared by:

Bolt Beranek and Newman Inc.
50 Moulton Street
Cambridge, MA 02138

Prepared for:

National Aeronautics and Space Administration
Langley Research Center
Hampton, Virginia 23665

1. Report No.	2. Government Accession No.	3. Recipient's Catalog No.
NASA CR-159088		

4. Title and Subtitle	5. Report Date
Analysis of Vibratory Excitation of Gear Systems as a Contributor to Aircraft Interior Noise	February 1979
	6. Performing Organization Code
7. Author(s)	8. Performing Organization Report No.
William D. Mark	TM 502
	10. Work Unit No.
9. Performing Organization Name and Address	
Bolt Beranek and Newman Inc. 50 Moulton Street Cambridge, MA 02138	11. Contract or Grant No. NAS1-14611
	13. Type of Report and Period Covered Contract Report 1978-79
12. Sponsoring Agency Name and Address	
National Aeronautics and Space Administration Langley Research Center Hampton, VA 23665	14. Sponsoring Agency Code

15. Supplementary Notes

Project Manager, Dr. David Stephens
NASA Langley Research Center
Hampton, VA 23665

16. Abstract

Sound radiation ultimately arising from gearboxes is a major contributor to helicopter and turboprop cabin noise. Application of the transfer function approach to predict the resulting interior noise contribution requires gearbox vibration sources and paths to be characterized in the frequency domain. In previous work [J. Acoust. Soc. Am., 63 (1978), pp. 1409-1430], the frequency domain characterization of the vibratory excitation of a generic pair of meshing gears was shown to require the Fourier-series coefficients of the static transmission error of that pair. Static transmission error spectrum contributions at tooth-meshing harmonics were shown to be attributable to elastic tooth deformations and the average deviation of gear teeth faces from perfect involute surfaces with uniform spacing, whereas spectrum contributions at other gear rotational harmonics were shown to be attributable to deviations of individual tooth faces from the average face of uniformly spaced teeth. The present work continues this analysis by representing tooth-face deviations from perfect involute surfaces in terms of Legendre polynomials which may be directly interpreted in terms of tooth-spacing errors, mean and random deviations associated with involute slope and fullness, lead mismatch and crowning, and analogous higher-order components. The contributions of these components to the spectrum of the static transmission error is discussed and illustrated using a set of measurements made on a pair of helicopter spur gears. The general methodology presented is applicable to both spur and helical gears.

17. Key Words (Suggested by Author(s))	18. Distribution Statement
Acoustics, Noise, Vibrations, Aircraft Noise, Helicopter Noise, Interior Noise, Transmission Noise, Gearbox Noise, Gear Noise, Static Transmission Error, Gears, Transmissions.	

19. Security Classif. (of this report)	20. Security Classif. (of this page)	21. No. of Pages	22. Price*
Unclassified	Unclassified	89	

* For sale by the National Technical Information Service, Springfield, Virginia 22161

ABSTRACT

Sound radiation ultimately arising from gearboxes is a major contributor to helicopter and turboprop cabin noise. Application of the transfer function approach to predict the resulting interior noise contribution requires gearbox vibration sources and paths to be characterized in the frequency domain. In previous work [J.Acoust. Soc. Am., 63 (1978), pp. 1409-1430], the frequency domain characterization of the vibratory excitation of a generic pair of meshing gears was shown to require the Fourier-series coefficients of the static transmission error of that pair. Static transmission error spectrum contributions at tooth-meshing harmonics were shown to be attributable to elastic tooth deformations and the average deviation of gear teeth faces from perfect involute surfaces with uniform spacing, whereas spectrum contributions at other gear rotational harmonics were shown to be attributable to deviations of individual tooth faces from the average face of uniformly spaced teeth. The present work continues this analysis by representing tooth-face deviations from perfect involute surfaces in terms of Legendre polynomials which may be directly interpreted in terms of tooth-spacing errors, mean and random deviations associated with involute slope and fullness, lead mismatch and crowning, and analogous higher-order components. The contributions of these components to the spectrum of the static transmission error is discussed and illustrated using a set of measurements made on a pair of helicopter spur gears. The general methodology presented is applicable to both spur and helical gears.

TABLE OF CONTENTS

LIST OF FIGURES

LIST OF FIGURES *(Cont.)*

page

LIST OF FIGURES *(Cont.)*

page

INTRODUCTION

For some time, it has been recognized that sound radiation ultimately arising from the gearbox is a major contributor to helicopter interior noise. Many analyses of interior noise measurements have shown that the dominant frequencies are those associated with the meshing action of the gears — i.e., the so-called tooth-meshing harmonics and their sidebands. Hence, one approach to reducing helicopter interior noise is to reduce the vibratory excitation caused by the imperfect meshing action of the gears. Such an approach requires a thorough understanding of this source of vibratory excitation — which is the subject of the present report.

Consider a pair of rotating gears that transmit torque, and assume for simplicity that one member of the pair rotates at an exactly uniform speed. The mating gear will have a small jitter superimposed on its mean rotational speed, where this jitter arises from the nonconjugate action of the imperfect loaded teeth. This unsteady motion component is the dominant ultimate source of the vibratory excitation and noise arising from the gearbox [*1*].

The static transmission error describes this source of vibratory excitation. In Ref. 1, a method is explained for writing the equations of motion of gear systems using the static transmission error as the input. Such equations are most conveniently solved in the frequency domain. Since the static transmission error is periodic, it is described in the frequency domain by its Fourier-series coefficients, which therefore are of primary interest.

Expressions for these Fourier-series coefficients are given in Ref. 1 in terms of the mean surface of the tooth faces on a gear, deviations of the individual tooth-face surfaces from this mean surface, and a general tooth-pair stiffness characterization. These Fourier-series coefficients — and the corresponding power spectra of the individual tooth-face deviation components — are expressed in terms of general series expansions of the tooth-face surfaces and the tooth-stiffness characterization. The present report extends the work carried out in Ref. 1 by further developing these series expansions in terms of general orthogonal functions, and then specializing the results to expansions in two-dimensional Legendre polynomials, which are uniquely suited for the description of the deviations of tooth faces from perfect involute (conjugate) surfaces.

After completion of these general results, the Fourier-series coefficients and power spectra of the various static transmission error components are developed from a set of tooth-spacing accuracy measurements and profile measurements made from a pair of helicopter spur gears. Some of these results are then compared with results that would have been obtained with helical gears of comparable quality – bringing into focus the very substantial noise reduction achieved through the use of helical gears.

Acknowledgements. I am indebted to Bell Helicopter Textron for supplying tooth-spacing accuracy measurements and profile measurements for the Applications portion of this work. The cooperation of Mr. Charles E. Braddock, Senior Transmission Project Engineer, was particularly helpful. The computer programming required for the work was carried out by Mr. Raymond W. Fischer of BBN. Discussions with Dr. Fred R. Kern have been helpful in various stages of the work. The report was typed by Ms. Carolyn Gianino and the art work was done by Ms. Laura Selvitella.

HARMONIC ANALYSIS OF STATIC TRANSMISSION ERROR USING ORTHOGONAL EXPANSIONS

Orthogonal Expansions in Tooth Coordinates

Consider the expansion of an arbitrary function $F_C(y,z)$ in a set of orthogonal functions $\Psi_{Cm}(y,z)$; i.e.,

$$F_C(y,z) = \sum_m a_m \Psi_{Cm}(y,z) \ , \tag{1}$$

where y,z are the Cartesian tooth coordinates described in Sec. I.C of Ref. 1 and illustrated by the tooth shown in the upper right-hand corner of Fig. 4 of the same reference. In later sections, the expansion of Eq. (1) will be used to represent local tooth-pair stiffnesses $K_{TC}(y,z)$ and stiffness-weighted deviations of tooth faces from perfect involute surfaces. We shall assume that the expansion functions $\Psi_{Cm}(y,z)$ have been normalized so that their mean-square values are unity – i.e.,

$$\frac{1}{A'} \iint_{\Omega_C} \Psi_{Cm}(y,z)\Psi_{Cm'}(y,z)dydz = \delta_{mm'} \ , \tag{2}$$

where A' denotes the area of the region Ω_C in the y,z plane where the expansion functions are defined, and $\delta_{mm'}$ is Kronecker's delta. Since A' has the dimension of length squared, we see from Eq. (2) that the functions $\Psi_{Cm}(y,z)$ must be dimensionless. Thus, the expansion coefficients a_m in Eq. (1) have the same dimension as $F_C(y,z)$.

If we multiply Eq. (1) by $\Psi_{Cm'}(y,z)/A'$, integrate both sides of the resulting expression over Ω_C, and use Eq. (2), we obtain

$$a_m = \frac{1}{A'} \iint_{\Omega_C} F_C(y,z)\Psi_{Cm}(y,z)dydz, \tag{3}$$

which determines each expansion coefficient a_m as a function of $F_C(y,z)$. Squaring Eq. (1), we obtain

$$F_C^2(y,z) = \sum_m \sum_{m'} a_m a_{m'} \Psi_{Cm}(y,z)\Psi_{Cm'}(y,z). \tag{4}$$

Then, dividing Eq. (4) by A', integrating both sides of the resulting expression over Ω_C, and using Eq. (2), we have

$$\frac{1}{A'} \iint_{\Omega_C} F_C^2(y,z)\,dy\,dz = \sum_m a_m^2 \quad , \tag{5}$$

provided that the expansion functions form a complete set. According to Eq. (5), for each value of m, a_m^2 directly measures the contribution of the term $a_m\Psi_{Cm}(y,z)$ in Eq. (1) to the mean-square value of $F_C(y,z)$ defined by the left-hand side of Eq. (5). This property, which is a consequence of the normalization of Eq. (2), greatly facilitates interpretation of numerical values of the expansion coefficients.

Expansions in Legendre polynomials

We shall see later that the Legendre polynomials are a particularly useful set of functions to use in our orthogonal expansions. For the expansion functions in Eq. (1), let us take

$$\Psi_{Cm}(y,z) = \Psi_{yk}(y)\Psi_{z\ell}(z) \quad , \tag{6}$$

where

$$\Psi_{yk}(y) \triangleq (2k+1)^{\frac{1}{2}} P_k(2y/F), \qquad -(F/2)<y<(F/2) \tag{7}$$

$$\Psi_{z\ell}(z) \triangleq (2\ell+1)^{\frac{1}{2}} P_\ell(2z/D), \qquad -(D/2)<z<(D/2) \quad , \tag{8}$$

where $P_k(x)$ and $P_\ell(x)$ are Legendre polynomials as defined, for example, in Ref. 2. Thus, for the $\Psi_{Cm}(y,z)$ defined by Eqs. (6) to (8), the expansion region Ω_C is the rectangular domain y,z indicated in Eqs. (7) and (8).

Equations (6) to (8) imply a mapping of the Legendre indices k and ℓ onto the single index m. One such mapping is illustrated in Fig. 1. From the normalization of the Legendre polynomials — e.g., p. 175 of Ref. 2 — it follows directly that

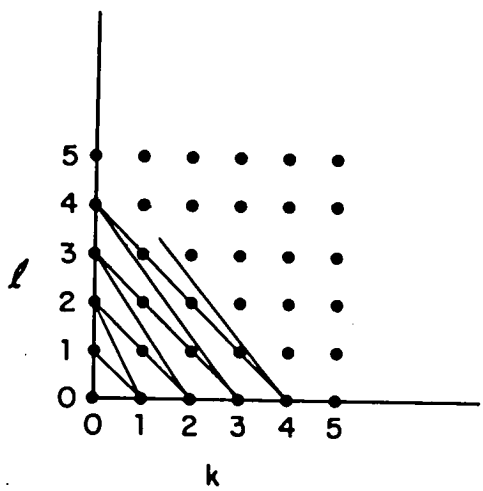

k	ℓ	m
0	0	0
0	1	1
1	0	2
0	2	3
1	1	4
2	0	5
0	3	6
1	2	7
2	1	8
3	0	9

FIGURE 1. MAPPING OF LEGENDRE INDICES k AND ℓ ONTO THE SINGLE INDEX m. THE ORDERING OF THE MAPPING FOLLOWS THE INDICATED PATH.

$$\frac{1}{FD}\int_{-D/2}^{D/2}\int_{-F/2}^{F/2}[\Psi_{yk}(y)\Psi_{z\ell}(z)]^2 dydz = 1 \ ; \tag{9}$$

hence, the definitions of Eqs. (6) to (8) satisfy the normalization condition implied by Eq. (2). For some of the work to follow, it will be convenient to have expressions analogous to Eqs. (1), (3), and (5) written directly in terms of the Legendre polynomials of Eqs. (6) to (8) using the double indices k,ℓ:

$$F_C(y,z) = \sum_{k=0}^{\infty}\sum_{\ell=0}^{\infty} a_{k\ell}\Psi_{yk}(y)\Psi_{z\ell}(z) \tag{10}$$

$$a_{k\ell} = \frac{1}{FD}\int_{-D/2}^{D/2}\int_{-F/2}^{F/2} F_C(y,z)\Psi_{yk}(y)\Psi_{z\ell}(z)dydz \tag{11}$$

$$\frac{1}{FD}\int_{-D/2}^{D/2}\int_{-F/2}^{F/2} F_C^2(y,z)dydz = \sum_{k=0}^{\infty}\sum_{\ell=0}^{\infty} a_{k\ell}^2 . \tag{12}$$

One of the main reasons for our use of Legendre polynomials in the series representation of $F_C(y,z)$ is the fact that the two-dimensional Fourier transform of Eq. (10) can be expressed simply in terms of known functions. Using a caret to denote the Fourier transform of a function as in Ref. 1, we can express the Fourier transforms of the Legendre expansion functions of Eqs. (7) and (8) as

$$\begin{aligned}\hat{\Psi}_{yk}(g_1) &\triangleq \int_{-\infty}^{\infty}\Psi_{yk}(y)\exp(-i2\pi g_1 y)dy \\ &= (2k+1)^{\frac{1}{2}}(F/2)\hat{P}_k(Fg_1/2) \\ &= (-i)^k F(2k+1)^{\frac{1}{2}} j_k(\pi F g_1)\end{aligned} \tag{13}$$

and

$$\hat{\Psi}_{z\ell}(g_2) \triangleq \int_{-\infty}^{\infty} \Psi_{z\ell}(z)\exp(-i2\pi g_2 z)dz$$

$$= (2\ell+1)^{\frac{1}{2}}(D/2)\hat{P}_{\ell}(Dg_2/2)$$

$$= (-i)^{\ell}D(2\ell+1)^{\frac{1}{2}}j_{\ell}(\pi Dg_2) \qquad (14)$$

where, for n = k and ℓ, we have defined

$$\hat{P}_n(g) \triangleq \int_{-\infty}^{\infty} P_n(x)\exp(-i2\pi gx)dx \ . \qquad (15)$$

In arriving at Eqs. (13) and (14), we have used Eq. (1) on p. 122 of Ref. 3 and the definition

$$j_n(x) \triangleq [\pi/(2x)]^{\frac{1}{2}}J_{n+1/2}(x) \ , \qquad (16)$$

where $j_n(x)$ is the spherical Bessel function of the first kind of order n as defined on p. 437 of Ref. 4 in terms of the Bessel functions $J_{n+1/2}(x)$ of the first kind of order n+1/2. From Eqs. (1), (10), (13), and (14) we obtain the desired representation of the two-dimensional Fourier transform of $F_C(y,z)$ expressed in terms of the expansion coefficients defined by Eqs. (3) and (11):

$$\hat{F}_C(g_1,g_2) \triangleq \int_{-\infty}^{\infty} F_C(y,z)\exp[-i2\pi(g_1y+g_2z)]dydz$$

$$= \sum_m a_m \hat{\Psi}_{Cm}(g_1,g_2)$$

$$= \sum_{k=0}^{\infty}\sum_{\ell=0}^{\infty} a_{k\ell}\hat{\Psi}_{yk}(g_1)\hat{\Psi}_{z\ell}(g_2)$$

$$= FD\sum_{k=0}^{\infty}\sum_{\ell=0}^{\infty}(-i)^{k+\ell}a_{k\ell}[(2k+1)(2\ell+1)]^{\frac{1}{2}}j_k(\pi Fg_1)j_{\ell}(\pi Dg_2). \qquad (17)$$

Fourier-Series Coefficients of Reciprocal Mesh Stiffness and Load-Dependent Component of Static Transmission Error

Equation (77) of Ref. 1 provides a general expression for the Fourier-series coefficients of the reciprocal mesh stiffness $1/K_T(x)$ in terms of the ratios $\alpha_{Kn}/\bar{K}_T$ as indicated by Eq. (87) of Ref. 1. When tooth contact takes place over the entire rectangular face region

$$-(F/2) < y < (F/2)$$

$$-(D/2) < z < (D/2)$$

as illustrated in the upper right-hand corner of Fig. 4 of Ref. 1, we may use Eq. (17) to develop an expression for the Fourier-series coefficients of $1/K_T(x)$. In this application of the preceding results, we identify $F_C(y,z)$ with the local stiffness of a pair of teeth per unit length of line of contact $K_{TC}(y,z)$ expressed in the Cartesian tooth coordinates defined by Eqs. (15), (16), and (19) of Ref. 1. When we write the expansion coefficients of Eq. (11) as

$$a_{k\ell} = \frac{1}{FD} \int_{-D/2}^{D/2} \int_{-F/2}^{F/2} K_{TC}(y,z)\Psi_{yk}(y)\Psi_{z\ell}(z)dydz \ , \tag{18}$$

where $\Psi_{yk}(y)$ and $\Psi_{z\ell}(z)$ are defined by Eqs. (7) and (8) respectively, we obtain from Eq. (17) the two-dimensional Fourier transform of $K_{TC}(y,z)$ defined by Eq. (82) of Ref. 1:

$$\hat{K}_{TC}(g_1,g_2) = FD \sum_{k=0}^{\infty} \sum_{\ell=0}^{\infty} (-i)^{k+\ell} a_{k\ell}[(2k+1)(2\ell+1)]^{\frac{1}{2}} \times$$

$$j_k(\pi F g_1) j_\ell(\pi D g_2). \tag{19}$$

Since

$$j_0(0) = 1 \tag{20a}$$

and

$$j_n(0) = 0, \qquad n = 1,2,\cdots \tag{20b}$$

(Ref. 4, p. 437), we have from Eq. (19)

$$\hat{K}_{TC}(0,0) = FDa_{00} \quad . \tag{21}$$

Therefore, from Eqs. (19), (21), and Eq. (86) of Ref. 1, it follows that

$$(\alpha_{Kn}/\bar{K}_T) = \sum_{k=0}^{\infty} \sum_{\ell=0}^{\infty} (-i)^{k+\ell} (a_{k\ell}/a_{00})[(2k+1)(2\ell+1)]^{\frac{1}{2}}$$

$$\times j_k[n\pi FL/(A\Delta)]j_\ell(n\pi L/\Delta). \tag{22}$$

The Fourier-series coefficients of $1/K_T(x)$ can be approximated to any desired degree of accuracy by combining Eq. (22) with Eqs. (76), (77), and (87) of Ref. 1. For cases where M in Eq. (77) of Ref. 1 is taken larger than unity, we see from Eqs. (76), (77), and (87) that one or more discrete convolutions of $\alpha_{Kn}/\bar{K}_T$ with itself are required. These convolutions generally will have to be carried out numerically.

For the case where M is taken to be unity, the Fourier-series coefficients of $1/K_T(x)$ may be approximated using Eq. (77) of Ref. 1 by

$$\alpha_{(1/K)n} \approx (\bar{K}_T)^{-1}[2(\alpha_{Kn}/\bar{K}_T)^{[0]} - (\alpha_{Kn}/\bar{K}_T)^{[1]}]$$

$$= (\bar{K}_T)^{-1}[2\delta_{n,0} - (\alpha_{Kn}/\bar{K}_T)] \tag{23}$$

where Eqs. (87) and (76) of Ref. 1 have been used, and where $\delta_{n,0}$ is Kronecker's delta. To obtain an expression for $\bar{K}_T$ for use in Eq. (23), we combine Eq. (21) with Eq. (85) of Ref. 1 to obtain

$$\bar{K}_T = a_{00}(FL/\Delta)\sec\psi_b$$

$$= \bar{K}_{TC}(FL/\Delta)\sec\psi_b \quad , \tag{24}$$

where $\bar{K}_{TC} \equiv a_{00}$ is the average value of the local tooth-pair stiffness:

$$\bar{K}_{TC} \triangleq \frac{1}{FD} \int_{-D/2}^{D/2} \int_{-F/2}^{F/2} K_{TC}(y,z)\,dydz \ , \tag{25}$$

as may be seen from Eqs. (7), (8), and (18) evaluated for k=0, ℓ=0, and from the fact that $P_0(x) \equiv 1$.

Our desired expression for the Fourier-series coefficients α_{Wn} of the load dependent component $\zeta_W(x)_0$ of the static transmission error is obtained, according to Eq. (68) of Ref. 1, by multiplying the total mesh loading W_0 by the Fourier-series coefficients of $1/K_T(x)$. According to Eqs. (22) and (23), for M = 1 this expression is

$$\alpha_{Wn} = (W_0/\bar{K}_T)\Bigg\{ 2\delta_{n,0} - \sum_{k=0}^{\infty} \sum_{\ell=0}^{\infty} (-i)^{k+\ell} (a_{k\ell}/a_{00}) \times$$

$$[(2k+1)(2\ell+1)]^{\frac{1}{2}} j_k[n\pi FL/(A\Delta)]\, j_\ell(n\pi L/\Delta)\Bigg\} \tag{26}$$

where $\bar{K}_T$ is given by Eqs. (24) and (25).

Discussion. The spherical Bessel functions in Eq. (26) depend on two dimensionless parameters, L/Δ and $FL/(A\Delta)$, which will appear repeatedly throughout the remainder of the paper. The parameter L/Δ is the profile or transverse contact ratio whereas $FL/(A\Delta)$ is the axial contact ratio [*5,6*]. According to Fig. 2 of Ref. 1, L/Δ is the length L of the path of contact divided by the tooth spacing Δ, both measured on a line defined by the intersection of a plane normal to the gear axes (transverse plane [*5,6*]) and the plane of contact. Furthermore, according to Eq. (D5) of Ref. 1, we have $A = L/\tan\psi_b$. If we denote by Δ_a the tooth spacing in the axial direction measured in the plane of contact (axial pitch [*6*]) then from Fig. 2 of Ref. 1 we see that

$$\tan\psi_b = \Delta/\Delta_a \ , \tag{27}$$

hence, we have

$$FL/(A\Delta) = F/\Delta_a \tag{28}$$

which is the ratio of the face width to the axial pitch – i.e., the axial contact ratio (Ref. 6, p. 211). For helical gears, the axial contact ratio can be interpreted as the *average* number of teeth in contact across their full depth D, as illustrated in the upper right-hand corner of Fig. 4 of Ref. 1. For spur gears, the transverse contact ratio can be interpreted as the *average* number of teeth in full contact across the gear face.

Table 1 gives *approximate* percentage errors in the expressions for reciprocal mesh stiffness – Eqs. (71) to (74) of Ref. 1 – as a function of the truncation parameter M and the contact ratio. In interpreting Table 1, the contact ratio chosen should be the larger of L/Δ or $FL/(A\Delta)$. For a typical spur gear transverse contact ratio of $(L/\Delta) = 1.5$, it may be seen from Table 1 that the value of $M = 1$ used in deriving Eq. (26) provides adequate accuracy for most vibration excitation calculations. For helical gears with larger (axial) contact ratios, the accuracy of Eq. (26) is better than that for the spur gear case. From Table 1, we see that the formulas for reciprocal mesh stiffness given by Eqs. (72) to (74) of Ref. 1 all yield an error of about one percent for the contact ratios cited in connection with those equations. The method used to calculate Table 1 is described in Appendix A of this report.

TABLE I. - APPROXIMATE PERCENTAGE ERRORS IN CALCULATION OF RECIPROCAL MESH STIFFNESS AS A FUNCITON OF CONTACT RATIO AND TRUNCATION PARAMETER M.

Contact Ratio	M		
	1	2	3
1.5	11.1	3.7	1.23
2.5	4.0	0.8	0.16
5.0	1.0	0.1	0.01

Application of Eq. (26) to helical gears involves a doubly infinite summation over the indices k and ℓ. This summation arises from expansion of the local tooth-pair stiffness $K_{TC}(y,z)$ in the two-dimensional Legendre series of Eq. (10), where the expansion coefficients are given by Eq. (18). From deflection measurements made on spur and helical gears – e.g., Figs. 5 to 8 of Ref. 7 and Fig. 10 of Ref. 8 (Part 2) – we would expect excellent accuracy in our expansion of $K_{TC}(y,z)$ when the summation over the profile (transverse) index ℓ is truncated at $\ell=4$. Such a truncation will result in a least-squares fourth-degree polynomial approximation of the function $K_{TC}(y,z)$ in the variable

z. For helical gears, the number of terms required in the summation over k for a given accuracy requirement will depend on the ratio F/D — as this ratio increases, it can be seen from tooth deflection measurements (Refs. 8-10) that an increasing number of terms will be required.

For application of Eq. (26) to spur gears, we note from Eq. (C4) of Ref. 1 — or from Fig. 4 of the same reference — that for zero helix angles we have (L/A) = 0. Thus, using Eqs. (20a) and (20b) we see that Eq. (26) reduces *in the case of spur gears* to

$$\alpha_{Wn} = (W_0/\bar{K}_T)\left[2\delta_{n,0} - \sum_{\ell=0}^{\infty}(-i)^{\ell}(a_{0\ell}/a_{00})(2\ell+1)^{\frac{1}{2}}j_{\ell}(n\pi L/\Delta)\right] , \quad (29)$$

which involves only a single summation over ℓ. Using the fact that $P_0(x) \equiv 1$, we see from Eqs. (7) and (18) that *for spur gears* the expansion coefficients in Eq. (29) can be expressed as

$$a_{0\ell} = \frac{1}{D}\int_{-D/2}^{D/2}\left[\frac{1}{F}\int_{-F/2}^{F/2} K_{TC}(y,z)dy\right]\Psi_{z\ell}(z)dz , \quad (30)$$

which depends only on the "axial average" of the local tooth-pair stiffness $K_{TC}(y,z)$ — see the sketch in the upper right-hand corner of Fig. 4 of Ref. 1.

We can obtain additional insight into Eq. (29) by recognizing that, to a first order of approximation, we can assume that $K_{TC}(y,z)$ is a constant. In this case — as may be seen from Eqs. (8) and (30) — Eq. (29) reduces to

$$\alpha_{Wn} \simeq (W_0/\bar{K}_T)[2\delta_{n,0} - j_0(n\pi L/\Delta)] , \quad (31)$$

where (Ref. 4, p. 438), we have

$$j_0(n\pi L/\Delta) = \frac{\sin(n\pi L/\Delta)}{n\pi L/\Delta} . \quad (32)$$

According to Eq. (32), if L/Δ is an integer we have $j_0(n\pi L/\Delta)=0$ for $n=1,2,3,\cdots$; hence, from Eq. (31) it follows that if L/Δ is an integer, we have $W_n=0$ for $n = 1,2,3,\cdots$ — i.e., the tooth deformation contributions to the harmonics of the static transmission error at the tooth-meshing frequencies vanish. Reductions

in gear noise for integral contact ratios have been observed experimentally — e.g., Fig. 9 of Ref. 11. However, for *accurate* spur gear calculations, terms at least through $\ell=4$ should be retained in the expansion of the local stiffness $K_{TC}(y,z)$; in addition, terms at least through M=3 should be retained in Eq. (77) of Ref. 1.

In the case of helical gears when we assume that $K_{TC}(y,z)$ is a constant, Eq. (26) reduces to

$$\alpha_{Wn} \approx (W_0/\bar{K}_T)\{2\delta_{n,0}-j_0[n\pi FL/(A\Delta)]j_0(n\pi L/\Delta)\} , \tag{33}$$

as may be seen from Eqs. (7), (8), and (18). From Eqs. (32) and (33), we see that if L/Δ is an integer, we have $\alpha_{Wn} = 0$ for $n = 1,2,3,\cdots$ in this case also; moreover, since

$$j_0[n\pi FL/(A\Delta)] = \frac{\sin[n\pi FL/(A\Delta)]}{n\pi FL/(A\Delta)} , \tag{34}$$

it follows that if $FL/(A\Delta)$ is an integer, we also have $\alpha_{Wn} = 0$ for the tooth-meshing harmonics $n = 1,2,3,\cdots$. Thus, in the helical gear case when $K_{TC}(y,z)$ is assumed to be a constant we require that *either* L/Δ or $FL/(A\Delta)$ be an integer for the vanishing of the tooth deformation contribution to the tooth-mesing harmonics.

These integral contact ratio criteria can be understood with the aid of Fig. 2, which illustrates the zone of contact, as shown in Fig. 2 of Ref. 1, but for cases of integral transverse and axial contact ratios $(L/\Delta) = 2$ and $(FL/A\Delta) = 3$. From Fig. 2, we see that if either contact ratio is an integer, there is no fluctuation in the total length of lines of contact within the zone of contact as the gears rotate. Consequently, if the local tooth-pair stiffness per unit length of line of contact $K_{TC}(y,z)$ is a constant, then when either the transverse or the axial contact ratio is a constant there is no variation in the total stiffness of the mesh as the gears rotate. Hence, for this case, the tooth deformation component of the static transmission error is the constant value

$$\alpha_{W0} \approx W_0/\bar{K}_T , \tag{35}$$

as may be seen from Eqs. (20a) and (33). Notice that the value of the d-c component given by Eq. (35) also is predicted from the more general form of α_{Wn} given by Eq. (26) — as one may see from Eqs. (20a) and (20b).

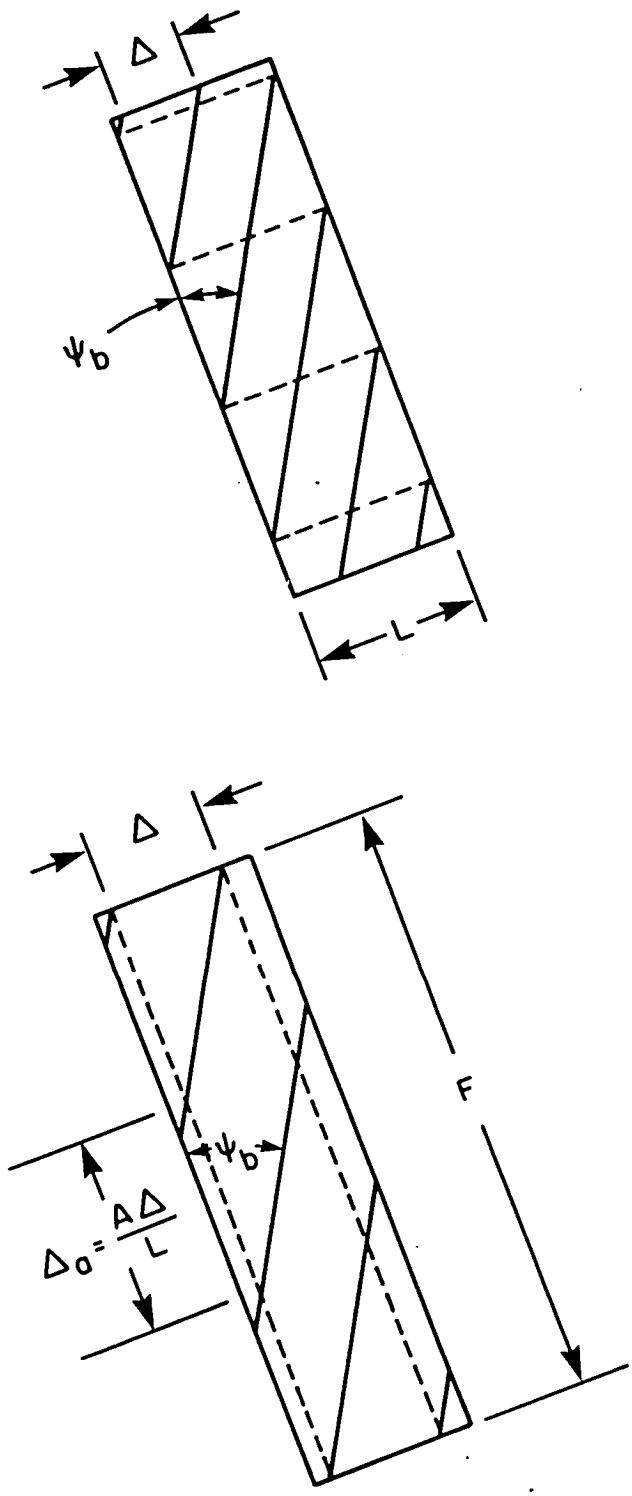

FIGURE 2. BASE PLANE ZONES OF CONTACT WITH NONFLUCTUATING TOTAL LENGTH OF LINES OF CONTACT. ZONE OF CONTACT IN UPPER SKETCH SATISFIES $(L/\Delta) = 2$. ZONE OF CONTACT IN LOWER SKETCH SATISFIES $(FL/A\Delta) = 3$.

For accurate calculations involving helical gears with axial contact ratios less than 5, values of M larger than unity should be used in Eq. (77) of Ref. 1, as indicated by Eqs. (72) to (74) of Ref. 1 and Table 1; moreover, additional terms beyond k=0 and ℓ=0 should be used in the summations in Eq. (26), as we have indicated above.

Finally, we note – e.g., from Eq. (16) and Eq. (37.4) on p. 139 of Ref. 12 – that as $x \to \infty$, the spherical Bessel functions $j_n(x)$ have the asymptotic form

$$j_m(x) = x^{-1}\cos[x-(m+1)\pi/2] + O(1/x^2), \qquad x \to \infty. \tag{36}$$

It follows from Eqs. (26) and (36) that for large n, the envelope of α_{Wn} decays as $1/n^2$. However, for sufficiently large n this result will break down due to the fact that the zones of contact on the faces of real gears have rounded corners.

Harmonic Analysis of Mean and Random Components of Static Transmission Error Caused by Deviations of Tooth Faces from Perfect Involute Surfaces

Orthogonal expansions of deviations of tooth-faces from perfect involute surfaces

Let us consider expansion of the stiffness-weighted mean and random deviations of the tooth faces from perfect involute surfaces:

$$m_{KC}^{(\cdot)}(y,z) = \sum_m a_m^{(\cdot)} \Psi_{KCm}(y,z) \tag{37}$$

and

$$\varepsilon_{KCj}^{(\cdot)}(y,z) = \sum_m b_{j,m}^{(\cdot)} \Psi_{KCm}(y,z) \ , \tag{38}$$

which are Eqs. (126) and (131) of Ref. 1. The mean deviations $m_{KC}^{(\cdot)}(y,z)$ and their expansion coefficients are independent of tooth number j, whereas the random deviations $\varepsilon_{KCj}^{(\cdot)}(y,z)$ and their expansion coefficients generally differ from tooth to tooth and therefore depend on j. We shall use the same expansion functions $\Psi_{KCm}(y,z)$ for both the mean and the random deviations:

$$\Psi_{KCm}(y,z) \triangleq \bar{K}_{TC}\Psi_{Cm}(y,z) \ , \tag{39}$$

where

$$\bar{K}_{TC} \triangleq \frac{1}{A'} \iint_{\Omega_C} K_{TC}(y,z)\,dydz \tag{40}$$

is the average value of the local tooth-pair stiffness and A' is the area of the tooth contact region Ω_C.

In the case of the mean deviations $m_{KC}^{(\cdot)}(y,z)$ of Eq. (37), if we identify $m_{KC}^{(\cdot)}(y,z)/\bar{K}_{TC}$ with the function $F_C(y,z)$ in Eq. (1), we see from Eqs. (37) and (39) that we may apply the general results of Eqs. (1) to (5) to the present situation – i.e.,

$$a_m^{(\cdot)} = \frac{1}{A'} \iint_{\Omega_C} \left[m_{KC}^{(\cdot)}(y,z)/\bar{K}_{TC} \right] \Psi_{Cm}(y,z)\,dydz \tag{41}$$

$$\frac{1}{A'} \iint_{\Omega_C} \left[m_{KC}^{(\cdot)}(y,z)/\bar{K}_{TC} \right]^2 dydz = \sum_m \left(a_m^{(\cdot)} \right)^2 . \tag{42}$$

Similarly, in the case of the random deviations of Eq. (38), if we identify $\varepsilon_{KCj}^{(\cdot)}(y,z)/\bar{K}_{TC}$ with $F_C(y,z)$ in Eq. (1), we have

$$b_{j,m}^{(\cdot)} = \frac{1}{A'} \iint_{\Omega_C} \left[\varepsilon_{KCj}^{(\cdot)}(y,z)/\bar{K}_{TC} \right] \Psi_{Cm}(y,z)\,dydz \tag{43}$$

and

$$\frac{1}{A'} \iint_{\Omega_C} \left[\varepsilon_{KCj}^{(\cdot)}(y,z)/\bar{K}_{TC} \right]^2 dydz = \sum_m \left(b_{j,m}^{(\cdot)} \right)^2 , \tag{44}$$

where in Eqs. (42) and (44) we have assumed that the functions $\Psi_{Cm}(y,z)$ form a complete set.

In the discussion of Eq. (2), we pointed out that the expansion functions $\Psi_{Cm}(y,z)$ must be dimensionless. Furthermore, since area A' has the dimension of length squared, it follows from Eq. (40) that $\bar{K}_{TC}$ and $K_{TC}(y,z)$ have the same dimension (force divided by length squared). Thus, from Eq. (48) of Ref. 1 and Eq. (41), we see that the expansion coefficients $a_m^{(\cdot)}$ have the same dimension (length) as the nonweighted mean tooth deviations $m_C^{(\cdot)}(y,z)$; furthermore, from Eq. (51) of Ref. 1 and Eq. (43), we see that the $b_{j,m}^{(\cdot)}$ have the same dimension (length) as the nonweighted random tooth deviations $\varepsilon_{Cj}^{(\cdot)}(y,z)$. Consequently, we see from Eq. (42) that, for each value of m, $(a_m^{(\cdot)})^2$ is a direct measure of the contribution of the term $a_m^{(\cdot)}\Psi_{KCm}(y,z)$ in Eq. (37) to the stiffness-weighted mean-square value of the mean tooth-face deviations $m_C^{(\cdot)}(y,z)$. Similarly, we see from Eq. (44) that $(b_{j,m}^{(\cdot)})^2$ is a direct measure of the contribution of the term $b_{j,m}^{(\cdot)}\Psi_{KCm}(y,z)$ in Eq. (38) to the stiffness-weighted mean-square value of the random tooth-face deviations $\varepsilon_{KCj}^{(\cdot)}(y,z)$. Notice from Eqs. (48) and (51) of Ref. 1 and Eqs. (40) to (44) above that when the local tooth-pair stiffness $K_{TC}(y,z)$ is a constant, the values of the expansion coefficients $a_m^{(\cdot)}$ and $b_{j,m}^{(\cdot)}$ become independent of the tooth-pair stiffness.

The results of Eqs. (37) to (44) — together with the material in Sec. II.E of Ref. 1 — provide a general set of formulas for the contributions to the Fourier-series coefficients of the mean and random components of the static transmission error caused by tooth-face devaitions from perfect involute surfaces. These results also provide formulas for the power spectrum of the component of the static transmission error caused by random tooth-face deviations from perfect involute surfaces.

Legendre polynomial expansions of tooth-face deviations

To apply the above results to specific sets of expansion functions $\Psi_{Cm}(y,z)$, m = 0,1,2,···, the functions $\hat{\Psi}_{Km}(g)$ and $\hat{\phi}_m(g)$ must be evaluated using Eqs. (123) and (124) of Ref. 1. In the case of the Legendre expansion functions defined by Eqs. (6) to (8), it follows from Eqs. (13), (14), and (39) that the functions $\hat{\Psi}_{Km}(g)$ of Eq. (124) of Ref. 1 may be expressed as

$$\hat{\underset{\sim}{\Psi}}_{Km}(g) = (L/D)\sec \Psi_b \; \bar{K}_{TC} \; \hat{\Psi}_{Cm}[(L/A)g, (L/D)g]$$

$$= \bar{K}_T \Delta (-i)^{k+\ell}[(2k+1)(2\ell+1)]^{\frac{1}{2}} j_k(\pi g FL/A)_{j\ell}(\pi gL) \ , \qquad (45)$$

where Eq. (125) of Ref. 1 and Eq. (24) have been used, and where a mapping of the indices k and ℓ onto the index m, such as that illustrated in Fig. 1, is implied by our subscript notation.

When Eq. (45) is combined with Eq. (123) of Ref. 1, we obtain a general expression for $\hat{\phi}_m(g)$ in terms of the Fourier-series coefficients $\alpha_{(1/K)n}$ of the reciprocal mesh stiffness. It was pointed out in Sec. IC that, when the truncation parameter M is taken larger than unity, the discrete convolutions required to compute the $\alpha_{(1/K)n}$ by Eq. (22), and Eqs. (76), (77), and (87) of Ref. 1, generally will have to be carried out numerically. However, when M is taken to be unity, the Fourier-series coefficients $\alpha_{(1/K)n}$ are given by the right-hand side of Eq. (26) after division by W_0, as may be seen from Eq. (68) of Ref. 1. Combining the resulting expression for $\alpha_{(1/K)n}$ with Eq. (45), and Eq. (123) of Ref. 1, we obtain for $\hat{\phi}_m(g) = \hat{\phi}_{k\ell}(g)$, *when M = 1:*

$$\hat{\phi}_{k\ell}(g) = (-i)^{k+\ell}[(2k+1)(2\ell+1)]^{\frac{1}{2}}\Bigg[j_k(\pi g FL/A) j_\ell(\pi gL) -$$

$$\sum_{\substack{n'=-\infty \\ \text{except} \\ n'=0}}^{\infty} \Bigg(\Bigg\{ \sum_{k'=0}^{\infty} \sum_{\ell'=0}^{\infty} (-i)^{k'+\ell'} (a_{k'\ell'}/a_{00})[(2k'+1)(2\ell'+1)]^{\frac{1}{2}} \times$$

$$j_{k'}(n'\pi FL/A\Delta) j_{\ell'}(n'\pi L/\Delta) \Bigg\} j_k[(\Delta g - n')\pi FL/A\Delta] j_\ell[(\Delta g - n')\pi L/\Delta] \Bigg) \Bigg] \qquad (46)$$

where $a_{k'\ell'}$ and a_{00} are the expansion coefficients for $K_{TC}(y,z)$ given by Eq. (18), and where Eqs. (20a) and (20b) have been used. The number of terms required in the double summation over k' and ℓ', and the approximate error involved in the truncation M=1, were discussed in an earlier section.

The function $\hat{\phi}_{k\ell}(g)$ plays a central role in the remainder of our analysis. The first term $j_k(\pi gFL/A)j_\ell(\pi gL)$ within the brackets in Eq. (46) arises from the dc component $\alpha_{(1/K)0}$ of of the reciprocal mesh stiffness, whereas the terms $\sum_{\substack{n'=-\infty \\ \text{except} \\ n'=0}}^{\infty} (\cdots)$ arise from the fluctuating components of the reciprocal mesh stiffness. See Eq. (123) of Ref. 1.

In the case of spur gears, we have (L/A) = 0 as noted earlier. Thus, using Eqs. (20a) and (20b), we see that Eq. (46) reduces *for spur gears* to

$$\hat{\phi}_{0\ell}(g) = (-i)^{\ell}(2\ell+1)^{\frac{1}{2}}\left[j_\ell(\pi gL) - \sum_{\substack{n'=-\infty \\ \text{except} \\ n'=0}}^{\infty} \left(\left\{ \sum_{\ell'=0}^{\infty} (-i)^{\ell'}(a_{0\ell'}/a_{00})(2\ell'+1)^{\frac{1}{2}} j_{\ell'}(n'\pi L/\Delta) \right\} \times j_\ell[(\Delta g - n')\pi L/\Delta] \right) \right] , \tag{47a}$$

$$\hat{\phi}_{k\ell}(g) = 0, \qquad k = 1,2,3,\cdots , \tag{47b}$$

where $a_{0\ell}$ is given by Eq. (30). In view of the accuracy limitations associated with the approximation M=1 in the case of spur gears, Eq. (47) must be regarded as a rough approximation only. See Table 1.

Fourier-series coefficients of mean deviation components

After replacing the summation index m in Eq. (130) of Ref. 1 by the dual indices k and ℓ, we can express the Fourier-series coefficients of the mean tooth-face deviation components of the transmission error by

$$\alpha_{mn}^{(\cdot)} = \sum_{k=0}^{\infty} \sum_{\ell=0}^{\infty} a_{k\ell}^{(\cdot)} \hat{\phi}_{k\ell}(n/\Delta) , \tag{48}$$

where $\hat{\phi}_{k\ell}(n/\Delta)$ can be evaluated from Eq. (46) by setting $g = n/\Delta$ whenever the accuracy provided by taking $M = 1$ is adequate. An expression for the coefficients $a_{k\ell}^{(\cdot)}$ in Eq. (48) can be obtained by combining Eqs. (6) and (41) with Eq. (48) of Ref. 1:

$$a_{k\ell}^{(\cdot)} = \frac{1}{FD} \int_{-D/2}^{D/2} \int_{-F/2}^{F/2} [K_{TC}(y,z)/\bar{K}_{TC}]\, m_C^{(\cdot)}(y,z) \Psi_{yk}(y) \Psi_{z\ell}(z) dy dz \ , \tag{49}$$

where $\Psi_{yk}(y)$ and $\Psi_{z\ell}(z)$ are the normalized Legendre polynomials defined by Eqs. (7) and (8), and where $m_C^{(\cdot)}(y,z)$ is the unloaded mean deviation of the tooth faces on gear $(\cdot)$ from perfect involute surfaces as defined by Eq. (49) of Ref. 1.

In the case of spur gears, we see from Eq. (47b) that Eq. (48) reduces to

$$\alpha_{mn}^{(\cdot)} = \sum_{\ell=0}^{\infty} a_{0\ell}^{(\cdot)}\, \hat{\phi}_{0\ell}(n/\Delta) \ , \tag{50}$$

where $\hat{\phi}_{0\ell}(n/\Delta)$ can be evaluated from Eq. (47a). From Eq. (49), we see that the expansion coefficients required in Eq. (50) can be expressed as

$$a_{0\ell}^{(\cdot)} = \frac{1}{D} \int_{-D/2}^{D/2} \left\{ \frac{1}{F} \int_{-F/2}^{F/2} [K_{TC}(y,z)/\bar{K}_{TC}]\, m_C^{(\cdot)}(y,z) dy \right\} \Psi_{z\ell}(z) dz \ , \tag{51}$$

where we have used the fact that $P_0(x) \equiv 1$.

Fourier-series coefficients and power spectra of random deviation components

The Fourier-series coefficients of the random components of the transmission error can be expressed in a manner similar to that above by replacing the summation index m in Eq. (134) of Ref. 1 by the indices k and ℓ:

$$\alpha_{rn}^{(\cdot)} = \sum_{k=0}^{\infty} \sum_{\ell=0}^{\infty} B_{k\ell}^{(\cdot)}(n) \hat{\phi}_{k\ell}(n/N^{(\cdot)}\Delta) \ , \tag{52}$$

where $\hat{\phi}_{k\ell}(n/N^{(\cdot)}\Delta)$ can be evaluated from Eq. (46) by setting $g = n/N^{(\cdot)}\Delta$ whenever the accuracy provided by taking M=1 is adequate. The expansion coefficients $B_{k\ell}^{(\cdot)}(n)$ in Eq. (52) are given in this case by Eq. (135) of Ref. 1 after substitution of the indices k,ℓ for the index m:

$$B_{k\ell}^{(\cdot)}(n) = \frac{1}{N^{(\cdot)}} \sum_{j=0}^{N^{(\cdot)}-1} b_{j,k\ell}^{(\cdot)} \exp(-i2\pi nj/N^{(\cdot)}) \ . \tag{53}$$

An expression for the coefficients $b_{j,k\ell}^{(\cdot)}$ in Eq. (53) can be obtained by combining Eqs. (6) and (43) with Eq. (51) of Ref. 1:

$$b_{j,k\ell}^{(\cdot)} = \frac{1}{FD} \int_{-D/2}^{D/2} \int_{-F/2}^{F/2} [K_{TC}(y,z)/\bar{K}_{TC}] \ \varepsilon_{Cj}^{(\cdot)}(y,z) \ \Psi_{yk}(y) \ \Psi_{z\ell}(z) dydz \ , \tag{54}$$

where $\Psi_{yk}(y)$ and $\Psi_{z\ell}(z)$ are the normalized Legendre polynomials defined by Eqs. (7) and (8), and $\varepsilon_{Cj}^{(\cdot)}(y,z)$ is the random component of the deviations of the tooth faces of gear (•) from perfect involute surfaces as defined by Eq. (50) of Ref. 1.

In the case of spur gears, Eqs. (52) and (54) reduce to

$$\alpha_{rn}^{(\cdot)} = \sum_{\ell=0}^{\infty} B_{0\ell}^{(\cdot)}(n) \ \hat{\phi}_{0\ell}(n/N^{(\cdot)}\Delta) \tag{55}$$

and

$$b_{j,0\ell}^{(\cdot)} = \frac{1}{D} \int_{-D/2}^{D/2} \left\{ \frac{1}{F} \int_{-F/2}^{F/2} [K_{TC}(y,z)/\bar{K}_{TC}] \ \varepsilon_{Cj}^{(\cdot)}(y,z) dy \right\} \Psi_{z\ell}(z) dz \ , \tag{56}$$

which follow from Eqs. (47b) and (7), and the fact that $P_0(x) \equiv 1$.

Formulas for the power spectra of the random components of the transmission error for a given gear are given by Eqs. (137) to (140) of Ref. 1. Application of the formulas to the present situation implies a mapping of k and ℓ onto m such as that illustrated in Fig. 1. These formulas can be evaluated from the set of coefficients $b^{(\cdot)}_{j,k\ell}$ given by Eq. (54), or Eq. (56) for spur gears, and the functions $\hat{\phi}_{k\ell}(g)$ given by Eq. (46) and evaluated at $g = n/N^{(\cdot)}\Delta$.

Discussion

For a generic pair of meshing gears there are three components to the deterministic contribution of the static transmission error — the tooth deformation component and the component from each of the two gears caused by the mean deviation of its tooth faces from perfect involute surfaces as indicated by Eq. (61) of Ref. 1. Each of these three components is a periodic function of x with period Δ. Consequently, each Fourier-series coefficient of the total deterministic contribution to the static transmission error is given by the sum of the Fourier-series coefficients from each of the three above-mentioned deterministic components as indicated by Eq. (65) of Ref. 1:

$$\alpha_{mn} = \alpha_{Wn} + \alpha^{(1)}_{mn} + \alpha^{(2)}_{mn} \quad . \tag{57}$$

Expressions for α_{Wn} and $\alpha^{(\cdot)}_{mn}$, $(\cdot) = (1)$ or (2), are given, e.g., by Eqs. (26) and (48).

In addition, for each pair of meshing gears there are two components to the random contribution of the transmission error as indicated by Eq. (62) of Ref. 1. The Fourier-series coefficients $\alpha^{(\cdot)}_{rn}$ of each of these random components are given by Eq. (52). The harmonic components of each of these two random components generally occur at different frequencies — e.g., when the numbers of teeth on the two meshing gears are prime to one another, the random components of the transmission error from each of two meshing gears have no nonzero harmonics that occur at the same frequencies [*1*].

The rates of convergence of the series in Eqs. (48) and (52) are governed, respectively, by the rates of convergence of the expansions in Eqs. (37) and (38) when the expansion functions $\Psi_{Cm}(y,z)$ in Eq. (39) are chosen to be the Legendre polynomials of Eqs. (6) to (8). Dividing Eqs. (37) and (38) by the mean stiffness $\overline{K}_{TC}$, then using Eqs. (6) to (8), (39), and Eqs. (48) and (51) of Ref. 1, we obtain

$$[K_{TC}(y,z)/\bar{K}_{TC}]m_C^{(\cdot)}(y,z) =$$

$$\sum_{k=0}^{\infty}\sum_{\ell=0}^{\infty} a_{k\ell}^{(\cdot)}[(2k+1)(2\ell+1)]^{\frac{1}{2}}\, P_k(2y/F)P_\ell(2z/D) \qquad (58)$$

$$[K_{TC}(y,z)/\bar{K}_{TC}]\varepsilon_{Cj}^{(\cdot)}(y,z) =$$

$$\sum_{k=0}^{\infty}\sum_{\ell=0}^{\infty} b_{j,k\ell}^{(\cdot)}[(2k+1)(2\ell+1)]^{\frac{1}{2}}\, P_k(2y/F)P_\ell(2z/D)\ , \qquad (59)$$

where we have used double subscripts $k\ell$ instead of single subscripts m, as before, and where the expansion coefficients are given by Eqs. (49) and (54). The first three Legendre polynomials are [2]

$$P_0(x) = 1$$

$$P_1(x) = x$$

$$P_2(x) = \frac{1}{2}(3x^2-1). \qquad (60)$$

For the purpose of interpreting the various low-order terms in Eqs. (58) and (59), if we assume that the local tooth-pair stiffness is a constant — i.e., $K_{TC}(y,z) = \bar{K}_{TC}$ — then we may identify these low-order terms with qualitative "error" descriptions used in the gear-engineering literature [*6,13*]. In this interpretation, the left-hand sides of Eqs. (58) and (59) represent, respectively, the mean and random deviations of the tooth faces from perfect involute surfaces. When we assume that $K_{TC}(y,z) = \bar{K}_{TC}$, the term k = 0, ℓ = 0 in Eq. (58) represents a constant displacement of every tooth on a given gear — i.e., a rigid body rotation of the gear. However, since the terms in Eq. (59) depend on tooth number j, the term k = 0, ℓ = 0 in Eq. (59) represents the pitch error of the jth tooth — i.e., the tooth-spacing error. According to the sketch in the upper right-hand corner of Fig. 4 of Ref. 1, the index k in Eqs. (58) and (59) is the lead "error" index; whereas the index ℓ is the

profile "error" index. Consequently, the terms k = 0, ℓ = 1 in Eqs. (58) and (59) represent involute slope deviations from perfect involute surfaces, since in this case the right-hand sides of Eqs. (58) and (59) are linear functions of the variable z illustrated in Fig. 4 of Ref. 1. Direct extension of this line of reasoning yields the following interpretations, *which are valid when we assume that* $K_{TC}(y,z) = \bar{K}_{TC}$*:*

$k = 0,\ \ell = 0$	*tooth-spacing deviations*
$k = 0,\ \ell = 1$	*pure involute slope deviations*
$k = 1,\ \ell = 0$	*pure lead mismatch deviations*
$k = 0,\ \ell = 2$	*pure involute hollow (fullness) deviations*
$k = 1,\ \ell = 1$	*combined lead mismatch-involute slope deviations*
$k = 2,\ \ell = 0$	*pure lead hollow (crowning) deviations.*

From the above interpretations and their extensions to the higher-order Legendre polynomials we may estimate the number of terms required for adequate engineering approximations in Eqs. (58) and (59), and hence the number of terms required in Eqs. (48) and (52) and in their respective spur gear counterparts, Eqs. (50) and (55). Furthermore, from the truncated sums of the squares of the expansion coefficients, we can use Eqs. (42) and (44) to determine the mean-square errors involved in truncations of the expansions in Eqs. (58) and (59).

Each term in the summations of Eqs. (48) and (52) contains two factors — an expansion coefficient and the function $\hat{\phi}_{k\ell}(g)$. The expansion coefficients characterize the stiffness-weighted derivations of the tooth faces from perfect involute surfaces, whereas the function $\hat{\phi}_{k\ell}(g)$ is independent of these deviations. Since these stiffness-weighted deviations [together with the load-dependent component of Eq. (26)] determine the vibratory excitation, we may regard each term in Eqs. (48) and (52) as a kind of transfer relationship that governs the vibratory excitation — the expansion coefficients characterize the "inputs" and the function $\hat{\phi}_{k\ell}(g)$, which is common to both Eq. (48) and Eq. (52), characterizes the effect of the meshing action of the gear pair on the inputs. The product of one of these expansion coefficient inputs and $\hat{\phi}_{k\ell}(g)$ yields the

mesh-attenuated input. Similar conclusions can be drawn from the power-spectrum representation of the random component described by Eq. (140) of Ref. 1.

It is appropriate to use the term *"mesh transfer function"* to describe each of the various terms $\hat{\phi}_{k\ell}(g)$. These mesh transfer functions depend only on the local tooth-pair stiffness and the nominal design parameters of the gear mesh, as may be seen from Eq. (46) for the case where M=1. This transfer function interpretation of $\hat{\phi}_{k\ell}(g)$ is further supported by the fact that every $\hat{\phi}_{k\ell}(g)$ is dimensionless. Further discussion of the mesh transfer functions $\hat{\phi}_{k\ell}(g)$ is provided in the next major section of this report.

Alternative expansion method of tooth-face deviations from perfect involute surfaces

We shall see later that from a certain theoretical point of view with important practical implications a set of expansion functions $\Psi_{KCm}(y,z)$ different from that indicated by Eq. (39) is preferable for representing the deviations of tooth faces from perfect involute surfaces. Let us consider now, instead of the set of expansion functions in Eq. (39), the set defined by

$$\Psi_{KCm}(y,z) \triangleq K_{TC}(y,z)\ \Psi_{Cm}(y,z)\ , \tag{61}$$

for use in representing the stiffness-weighted mean and random tooth-face deviations by Eqs. (37) and (38) respectively. The set of functions $\Psi_{Cm}(y,z)$ in Eqs. (39) and (61) are assumed to be the same; however, in Eq. (39) we have weighted the expansion functions with the average tooth-pair stiffness defined by Eq. (40), whereas in Eq. (61) this average stiffness has been replaced by the local tooth-pair stiffness which is a function of the tooth-face coordinates y,z. Notice that when $K_{TC}(y,z)$ is a constant value, Eq. (61) becomes identical with Eq. (39).

By comparing Eqs. (37) and (38) with Eqs. (48) and (51) of Ref. 1, we see that when the expansion functions $\Psi_{KCm}(y,z)$ are defined as in Eq. (61) the expansions of Eqs. (37) and (38) are equivalent to expansions of the nonstiffness-weighted mean and random deviations directly in terms of the functions $\Psi_{Cm}(y,z)$ — i.e.,

$$m_C^{(\cdot)}(y,z) = \sum_m a_m^{(\cdot)}\ \Psi_{Cm}(y,z) \tag{62}$$

and

$$\varepsilon_{Cj}^{(\cdot)}(y,z) = \sum_m b_{j,m}^{(\cdot)} \Psi_{Cm}(y,z) \ . \tag{63}$$

We may again apply the general results of Eqs. (1) to (5) to the expansions of Eqs. (62) and (63). By identifying $F_C(y,z)$ with $m_C^{(\cdot)}(y,z)$ and $\varepsilon_{Cj}^{(\cdot)}(y,z)$ in succession, we see from Eqs. (3) and (5) that our expansion coefficients for the mean deviation $m_C^{(\cdot)}(y,z)$ are

$$a_m^{(\cdot)} = \frac{1}{A'} \iint_{\Omega_C} m_C^{(\cdot)}(y,z) \Psi_{Cm}(y,z)dydz \ , \tag{64}$$

which satisfy

$$\frac{1}{A'} \iint_{\Omega_C} [m_C^{(\cdot)}(y,z)]^2 dydz = \sum_m (a_m^{(\cdot)})^2 \ , \tag{65}$$

whereas our expansion coefficients for the random deviations $\varepsilon_{Cj}^{(\cdot)}(y,z)$ are

$$b_{j,m}^{(\cdot)} = \frac{1}{A'} \iint_{\Omega_C} \varepsilon_{Cj}^{(\cdot)}(y,z) \Psi_{Cm}(y,z)dydz \ , \tag{66}$$

which satisfy

$$\frac{1}{A'} \iint_{\Omega_C} [\varepsilon_{Cj}^{(\cdot)}(y,z)]^2 dydz = \sum_m (b_{j,m}^{(\cdot)})^2 \ . \tag{67}$$

When the expansion functions $\Psi_{Cm}(y,z)$ are chosen to be the Legendre polynomials as in Eqs. (6) and (8), the expansion coefficients of Eqs. (64) and (66) take the form of Eq. (11) when $F_C(y,z)$ is identified with $m_C^{(\cdot)}(y,z)$ and $\varepsilon_{Cj}^{(\cdot)}(y,z)$, respectively.

In addition to the expansion coefficients $a_m^{(\cdot)}$ and $b_{j,m}^{(\cdot)}$, the functions $\hat{\phi}_m(g)$ are required for evaluation of the Fourier-series coefficients of the mean and random deviation components of the tooth faces, and for the power spectrum of the random components as may be seen from Eqs. (130), (134), and (140) of Ref. 1. From Eqs. (123), (124), and (125) of Ref. 1, we see that to evaluate $\hat{\phi}_m(g)$, we require the two-dimensional Fourier transform $\hat{\Psi}_{KCm}(g_1,g_2)$ of $\Psi_{KCm}(y,z)$, which in the case of Eq. (61) is expressed as

$$\hat{\Psi}_{KCm}(g_1,g_2) = \int_{-\infty}^{\infty}\int_{-\infty}^{\infty} K_{TC}(y,z)\ \Psi_{Cm}(y,z) \times \exp[-i2\pi(g_1y+g_2z)]dydz \ . \qquad (68)$$

Thus, when $\Psi_{KCm}(y,z)$ is chosen to take the form of Eq. (61), $\hat{\Psi}_{KCm}(g_1,g_2)$ depends on the functional behavior of the local tooth-pair stiffness $K_{TC}(y,z)$ and therefore cannot be expressed in closed form for a *generic* tooth-pair stiffness function. In contrast, when $\Psi_{KCm}(y,z)$ was chosen to take the form of Eq. (39), $\hat{\Psi}_{KCm}(g_1,g_2)$ could be expressed using Eqs. (13) and (14) as a function proportional to the product of two spherical Bessel functions [when $\Psi_{Cm}(y,z)$ was chosen to have the form of Eqs. (6) to (8)]. This simplification resulted in the relatively simple expression for $\hat{\underset{\sim}{\Psi}}_{Km}(g)$ given by Eq. (45) that, in turn, permitted us to obtain the general expression for $\hat{\phi}_{k\ell}(g)$ given by Eq. (46). However, for *specific* tooth-pair stiffness functions $K_{TC}(y,z)$, use of the expansion functions $\Psi_{KCm}(y,z)$ defined by Eq. (61) is practical when it is anticipated that the functions $\hat{\phi}_m(g)$ are to be evaluated numerically at the required values of $g = n/N^{(\cdot)}\Delta$, $n = 0, \pm1, \pm2, \cdots$.

Constant Tooth-Pair Stiffness Formulas

In this section, we summarize the special cases of the formulas derived in the preceding sections that apply to situations where the local tooth-pair stiffness per unit length of line of contact is assumed to be a constant – i.e., $K_{TC}(y,z) = \bar{K}_{TC}$, where $\bar{K}_{TC}$ is defined by Eq. (40). For these situations, the stiffness-weighted expansion functions given by Eqs. (39) and (61) are identical, and the alternative expansion method outlined in the preceding section reduces identically to the

method described earlier in the paper. In all of the considerations in this section, it is assumed that tooth contact takes place over the rectangular tooth-face region shown in the upper right-hand corner of Fig. 4 of Ref. 1. Formulas for spur gears are reduced in a separate section from those derived for helical gears.

Constant tooth-pair stiffness formulas for helical gears

Fourier-series coefficients of mesh stiffness and load-dependent component. Equations (68), (77), and (87) of Ref. 1 provide a set of formulas for the Fourier-series coefficients of the load-dependent component $\zeta_W(x)_0$ of the static transmission error in terms of the Fourier-series coefficients α_{Kn} of the instantaneous total mesh stiffness $K_T(x)$ divided by the time-averaged stiffness $\bar{K}_T$. For the case where $K_{TC}(y,z) = \bar{K}_{TC}$, we see from Eqs. (22), (32), and (34) that these latter normalized Fourier-series coefficients reduce to

$$(\alpha_{Kn}/\bar{K}_T) = \frac{\sin(n\pi FL/A\Delta)}{n\pi FL/A\Delta} \frac{\sin(n\pi L/\Delta)}{n\pi L/\Delta} , \tag{69}$$

where the vanishing of all coefficients $a_{k\ell}$ in Eq. (22) except a_{00} follows directly from the orthogonality of the two-dimensional Legendre expansion functions $\Psi_{yk}(y)\Psi_{z\ell}(z)$ given by Eqs. (6) to (8), the fact that $\Psi_{y0}(y)\Psi_{z0}(z) = 1$, and the expression for $a_{k\ell}$ given by Eq. (18) with $K_{TC}(y,z) = \bar{K}_{TC}$. For the case where M=1 in our approximation of the reciprocal mesh stiffness given by Eq. (71) of Ref. 1, it follows from Eqs. (23) and (69), and Eq. (68) of Ref. 1 that when $K_{TC}(y,z) = \bar{K}_{TC}$, the Fourier-series coefficients of the load-dependent component $\zeta_W(x)_0$ can be expressed as

$$\alpha_{Wn} \approx (W_0/\bar{K}_T) \left[2\delta_{n,0} - \frac{\sin(n\pi FL/A\Delta)}{n\pi FL/A\Delta} \frac{\sin(n\pi L/\Delta)}{n\pi L/\Delta} \right] ; \tag{70}$$

hence, since $(\sin x/x) = 0$ at $x = 0$, Eq. (70) is equivalent to

$$\alpha_{W0} \approx W_0/\bar{K}_T \tag{71a}$$

$$\alpha_{Wn} \approx - (W_0/\bar{K}_T) \frac{\sin(n\pi FL/A\Delta)}{n\pi FL/A\Delta} \frac{\sin(n\pi L/\Delta)}{n\pi L/\Delta} , \quad n \neq 0. \tag{71b}$$

In the above formulas, W_0 is the total (constant) force transmitted by the mesh as illustrated in Fig. 1 of Ref. 1, and $\bar{K}_T$ is the time-averaged value of the *total* mesh stiffness defined by Eq. (56) of Ref. 1, which is related to the tooth-pair stiffness per unit length of line of contact $\bar{K}_{TC}$ by Eq. (24).

Mesh transfer functions. When $K_{TC}(y,z) = \bar{K}_{TC}$, all expansion coefficients $a_{k\ell}$ of $K_{TC}(y,z)$ given by Eq. (18) vanish except a_{00} as indicated above. For this case, the mesh transfer functions $\hat{\phi}_{k\ell}(g)$ given by Eq. (46) for M=1 reduce to

$$\hat{\phi}_{k\ell}(g) = (-i)^{k+\ell}[(2k+1)(2\ell+1)]^{\frac{1}{2}}\{j_k(\pi gFL/A)j_\ell(\pi gL) - \sum_{\substack{n'=-\infty \\ \text{except} \\ n'=0}}^{\infty} j_0(n'\pi FL/A\Delta)j_0(n'\pi L/\Delta)j_k[(\Delta g-n')\pi FL/A\Delta]j_\ell[(\Delta g-n')\pi L/\Delta]\}. \tag{72}$$

Fourier-series coefficients of mean deviation components. Equation (48) expresses the Fourier-series coefficients of the mean deviation transmission error component $\zeta_m^{(\cdot)}$ from gear $(\cdot)$ in terms of the expansion coefficients $a_{k\ell}^{(\cdot)}$ and the mesh transfer functions $\hat{\phi}_{k\ell}(n/\Delta)$. In situations where $K_{TC}(y,z) = \bar{K}_{TC}$, we see from Eq. (58) that the $a_{k\ell}^{(\cdot)}$ are the expansion coefficients of the mean deviation $m_C^{(\cdot)}(y,z)$ of the tooth faces of gear $(\cdot)$ from perfect involute surfaces (without any stiffness weighting) as defined by Eq. (49) of Ref. 1 — i.e.,

$$m_C^{(\cdot)}(y,z) = \sum_{k=0}^{\infty}\sum_{\ell=0}^{\infty} a_{k\ell}^{(\cdot)}[(2k+1)(2\ell+1)]^{\frac{1}{2}}P_k(2y/F)P_\ell(2z/D) , \tag{73}$$

where, from Eqs. (7), (8), and (49), we see that the expansion coefficients are obtained from $m_C^{(\cdot)}(y,z)$ by

$$a_{k\ell}^{(\cdot)} = \frac{[(2k+1)(2\ell+1)]^{\frac{1}{2}}}{FD}\int_{-D/2}^{D/2}\int_{-F/2}^{F/2} m_C^{(\cdot)}(y,z)P_k(2y/F)P_\ell(2z/D)dydz \tag{74}$$

where $P_k(x)$ and $P_\ell(x)$ are the Legendre polynomials as defined in Ref. 2 and Eq. (60). From Eq. (48) of Ref. 1 and Eq. (42), we see that when $K_{TC}(y,z) = \bar{K}_{TC}$, the expansion coefficients $a_{k\ell}^{(\cdot)}$ of Eq. (74) satisfy

$$\frac{1}{FD}\int_{-D/2}^{D/2}\int_{-F/2}^{F/2}[m_C^{(\cdot)}(y,z)]^2 dydz = \sum_{k=0}^{\infty}\sum_{\ell=0}^{\infty}(a_{k\ell}^{(\cdot)})^2 \quad . \tag{75}$$

Therefore, the squares of the *expansion coefficients* $a_{k\ell}^{(\cdot)}$ are direct measures of the contributions of the various terms in Eq. (73) to the mean-square value of $m_C^{(\cdot)}(y,z)$ given by the left-hand side of Eq. (75).

In addition to the expansion coefficients given by Eq. (74), our expression, Eq. (48), for the Fourier-series coefficients of the mean deviation component requires the mesh transfer functions $\hat{\phi}_{k\ell}(g)$ evaluated at $g = n/\Delta$ — which we find from Eq. (72) to be for the case M=1:

$$\hat{\phi}_{k\ell}(n/\Delta) = (-i)^{k+\ell}[(2k+1)(2\ell+1)]^{\frac{1}{2}}\{j_k(n\pi FL/A\Delta)j_\ell(n\pi L/\Delta)$$

$$-\sum_{\substack{n'=-\infty \\ \text{except} \\ n'=0}}^{\infty} j_0(n'\pi FL/A\Delta)j_0(n'\pi L/\Delta)j_k[(n-n')\pi FL/A\Delta]j_\ell[(n-n')\pi L/\Delta]\}. \tag{76}$$

Let us consider $\hat{\phi}_{00}(n/\Delta)$:

$$\hat{\phi}_{00}(n/\Delta) = \frac{\sin(n\pi FL/A\Delta)}{n\pi FL/A\Delta}\,\frac{\sin(n\pi L/\Delta)}{n\pi L/\Delta}$$

$$-\sum_{\substack{n'=-\infty \\ \text{except} \\ n'=0}}^{\infty} \frac{\sin(n'\pi FL/A\Delta)}{n'\pi FL/A\Delta}\,\frac{\sin(n'\pi L/\Delta)}{n'\pi L/\Delta}\,\frac{\sin[(n-n')\pi FL/A\Delta]}{(n-n')\pi FL/A\Delta}\,\frac{\sin[(n-n')\pi L/\Delta]}{(n-n')\pi L/\Delta}\ , \tag{77}$$

where we have used the fact that $j_0(x) = (\sin x)/x$ as noted earlier. In Appendix B, it is shown that the most important term within the summation in Eq. (77) is the term n'=n. Retaining only this one "correction term" gives

$$\hat{\phi}_{00}(n/\Delta) = \begin{cases} 1, & n = 0 \\ 0, & n \neq 0 \end{cases} , \tag{78}$$

since at $x = 0$, we have $(\sin x)/x = 1$.

Although the derivation of Eqs. (77) and (78) involved several approximations, the result given by Eq. (78) is exact. To verify the validity of Eq. (78), consider the harmonic n = 0 first. Since $P_0(x) = 1$, we see from Eq. (73) that the contribution to $m_C^{(\cdot)}(y,z)$ arising from the term $a_{00}^{(\cdot)}$ is simply $a_{00}^{(\cdot)}$ – i.e., the same constant value added uniformly to the face of every tooth on gear (·). To interpret this result, we have from Eqs. (9) to (11) of Ref. 1 or equivalently from summing Eq. (8c) of Ref. 1 over all tooth pairs j in contact:

$$W = \sum_j W_j(x)$$

$$= \sec \psi_b \sum_j \int_{y_A}^{y_B} K_{Tj}(x,y)[\zeta(x) - \eta_j^{(1)}(x,y) - \eta_j^{(2)}(x,y)]dy \ . \tag{79}$$

For either of the gears (1) or (2) in contact, the tooth surface deviations $\eta_j^{(\cdot)}$ are the superposition of mean and random components as may be seen from Eq. (50) of Ref. 1. Hence, the addition of a mean component $a_{00}^{(\cdot)}$ to the deviations $\eta_j^{(\cdot)}$ of every tooth j on either gear (1) or gear (2) must give rise to the addition of the same constant value $a_{00}^{(\cdot)}$ to the transmission error $\zeta(x)$ within the brackets in Eq. (79) if the load W is to remain unchanged. But the addition of a constant value $a_{00}^{(\cdot)}$ to $\zeta(x)$ results in an increment of the same value $a_{00}^{(\cdot)}$ to the dc

Fourier-series coefficient $\alpha_{m0}^{(\cdot)}$ as may be seen from Eq. (67) of Ref. 1 when n = 0. Examination of this same dc contribution in Eq. (48) from the term $a_{00}^{(\cdot)}$ gives $a_{00}^{(\cdot)} = a_{00}^{(\cdot)}\hat{\phi}_{00}(0)$ after substitution of $a_{00}^{(\cdot)}$ for $\alpha_{m0}^{(\cdot)}$ in the left-hand side. We therefore must have $\hat{\phi}_{00}(0) = 1$ as indicated by Eq. (78). Furthermore, we have seen from Eq. (79) that the addition of a constant value $a_{00}^{(\cdot)}$ to the deviations $\eta_j^{(\cdot)}$ of every tooth on a gear is equivalent to adding the same *constant* value to the transmission error $\zeta(x)$; hence, the only nonzero Fourier-series coefficient arising from $a_{00}^{(\cdot)}$ is the dc term $\alpha_{m0}^{(\cdot)} = a_{00}^{(\cdot)}$. Thus, from Eq. (48), we must have $\hat{\phi}_{00}(n/\Delta) = 0$ for $n \neq 0$ — also as indicated by Eq. (78).

Conversely, we see that adding a constant value to $\zeta(x)$ within the brackets in Eq. (79) is equivalent to adding the same constant value to either $\eta_j^{(1)}(x,y)$ on $\eta_j^{(2)}(x,y)$ for every value of j if the load W is to remain unchanged. It therefore follows from the orthogonality of our expansion functions of the mean deviation components $m_C^{(\cdot)}(y,z)$ in Eq. (73) that the only tooth deviation components that can give rise to the dc component $\alpha_{m0}^{(\cdot)}$ of the transmission error are the constant deviations $a_{00}^{(\cdot)}$ of the teeth on gears (1) and (2). Hence, we must conclude from Eq. (48) that

$$\hat{\phi}_{k\ell}(0) = 0 \qquad \textit{whenever } k \textit{ and } \ell \textit{ are not both zero.} \qquad (80)$$

We shall see below that the above conclusions lead to important consequences with regard to "random" tooth-spacing errors. The results indicated by Eqs. (78) and (80) are valid for arbitrary tooth-pair stiffnesses per unit length of line of contact. These results — which separate pure tooth-spacing errors from other classes of errors — constitute the main reason why the expansion functions of Eq. (61) are theoretically preferable to those of Eq. (39) in cases where $K_{TC}(y,z)$ is not equal to the constant value $\bar{K}_{TC}$. The expansion functions of Eq. (61) are preferable in these cases because these expansion functions lead to the expansions, Eqs. (62) and (63), of the tooth-face deviations where the first terms m = 0 always can be made to represent pure tooth-spacing "errors". The expansion functions of Eq. (39) do not possess this property for arbitrary tooth-stiffness functions $K_{TC}(y,z)$, and as a result, for tooth-stiffness functions other than the constant value $K_{TC}(y,z) = \bar{K}_{TC}$, the properties of Eqs. (78) and (80) generally will not hold when the expansion functions of Eq. (39) are used.

Fourier-series coefficients and power spectra of random deviation components. Equation (52) expresses the Fourier-series coefficients of the random deviation transmission error component $\zeta_r^{(\cdot)}$ from gear $(\cdot)$ in terms of the mesh transfer functions $\hat{\phi}_{k\ell}(n/N^{(\cdot)}\Delta)$ and the discrete Fourier transforms $B_{k\ell}^{(\cdot)}(n)$ of the expansion coefficients $b_{j,k\ell}^{(\cdot)}$ as defined by Eq. (53). In situations where $K_{TC}(y,z) = \bar{K}_{TC}$, we see from Eq. (59) that the $b_{j,k\ell}^{(\cdot)}$ are the expansion coefficients of the random deviations $\varepsilon_{Cj}^{(\cdot)}(y,z)$ of the faces of gear $(\cdot)$ from perfect involute surfaces as defined by Eq. (50) of Ref. 1 – i.e.,

$$\varepsilon_{Cj}^{(\cdot)}(y,z) = \sum_{k=0}^{\infty} \sum_{\ell=0}^{\infty} b_{j,k\ell}^{(\cdot)} [(2k+1)(2\ell+1)]^{\frac{1}{2}} P_k(2y/F) P_\ell(2z/D) \ . \tag{81}$$

From Eqs. (7), (8), and (54), we may express the expansion co-coefficients in Eq. (81) in terms of $\varepsilon_{Cj}^{(\cdot)}(y,z)$ by

$$b_{j,k\ell}^{(\cdot)} = \frac{[(2k+1)(2\ell+1)]^{\frac{1}{2}}}{FD} \int_{-D/2}^{D/2} \int_{-F/2}^{F/2} \varepsilon_{Cj}^{(\cdot)}(y,z) P_k(2y/F) P_\ell(2z/D) dydz \ . \tag{82}$$

Furthermore, from Eq. (51) of Ref. 1 and Eq. (44), we see that when $K_{TC}(y,z) = \bar{K}_{TC}$, the expansion coefficients $b_{j,k\ell}^{(\cdot)}$ of Eq. (82) satisfy

$$\frac{1}{FD} \int_{-D/2}^{D/2} \int_{-F/2}^{F/2} [\varepsilon_{Cj}^{(\cdot)}(y,z)]^2 \, dydz = \sum_{k=0}^{\infty} \sum_{\ell=0}^{\infty} (b_{j,k\ell}^{(\cdot)})^2 \ . \tag{83}$$

Equations (137) to (140) of Ref. 1 express the discrete power spectrum $|\alpha_{rn}^{(\cdot)}|^2$ of the random deviation transmission error component from gear $(\cdot)$ in terms of the expansion coefficients $b_{j,k\ell}^{(\cdot)}$ and the mesh transfer functions $\hat{\phi}_{k\ell}(n/N^{(\cdot)}\Delta)$ –

where here a mapping of the index m onto the indices k and ℓ such as that illustrated by Fig. 1 is implied. *For a specific error component* designated by the index m or the *pair* of indices kℓ, the tooth-face random errors of gear (•) are characterized for this application by their mean-square values $\overline{(b_{k\ell}^{(\bullet)})^2}$ and autocorrelation coefficients $\rho_{k\ell}^{(\bullet)}(j)$ or discrete autospectra $S_{k\ell}^{(\bullet)}(n)$ as indicated by Eqs. (137) to (139) of Ref. 1:

$$\overline{(b_{k\ell}^{(\bullet)})^2} \triangleq \frac{1}{N^{(\bullet)}} \sum_{j=0}^{N^{(\bullet)}-1} (b_{j,k\ell}^{(\bullet)})^2 \quad , \tag{84}$$

$$\rho_{k\ell}^{(\bullet)}(j) \triangleq \left[\overline{(b_{k\ell}^{(\bullet)})^2}\right]^{-1} \frac{1}{N^{(\bullet)}} \sum_{j=0}^{N^{(\bullet)}-1} b_{j',k\ell}^{(\bullet)} b_{j'+j,k\ell}^{(\bullet)} \quad , \tag{85}$$

and

$$S_{k\ell}^{(\bullet)}(n) \triangleq \frac{1}{N^{(\bullet)}} \sum_{j=0}^{N^{(\bullet)}-1} \rho_{k\ell}^{(\bullet)}(j) \exp\left(\frac{-i2\pi nj}{N^{(\bullet)}}\right) \quad , \tag{86}$$

where $N^{(\bullet)}$ designates the number of teeth on gear (•). The contribution $|\alpha_{rn}^{(\bullet)}|_{k\ell}^2$ of *the single error component* designated by the pair of indices kℓ to the power spectrum $|\alpha_{rn}^{(\bullet)}|^2$ is then given by

$$|\alpha_{rn}^{(\bullet)}|_{k\ell}^2 \triangleq \overline{(b_{k\ell}^{(\bullet)})^2}\, S_{k\ell}^{(\bullet)}(n)\, |\hat{\phi}_{k\ell}(n/N^{(\bullet)}\Delta)|^2 \quad , \tag{87}$$

which arises from a single term m' = m" in the double summation in Eq. (140) of Ref. 1. When several random error components kℓ are present, cross-spectrum terms must be included to obtain all contributions to $|\alpha_{rn}^{(\bullet)}|^2$ as indicated by the double summation in Eq. (140) of Ref. 1 — unless these error components are uncorrelated in which case the cross-spectrum terms are zero.

Notice that Eq. (87) has the form of a power spectrum input-output relationship — e.g., Eq. (2.34) on p. 71 of Ref. 14. The input characterization is the mean-square error $\overline{(b_{k\ell}^{(\cdot)})^2}$ times the normalized tooth-error spectrum $S_{k\ell}^{(\cdot)}(n)$ — see Eqs. (84) to (87) — and the "system function" is the squared magnitude $|\hat{\phi}_{k\ell}(n/N^{(\cdot)}\Delta|^2$ of the mesh transfer function, which is independent of the tooth errors. The more general expression for $|\alpha_{rn}^{(\cdot)}|^2$ given by Eq. (140) of Ref. 1 has the form of the power spectrum of the output of a linear system to multiple random inputs — e.g., Eq. (5.42) on p. 149 of Ref. 15.

Modified forms of mesh transfer functions. Let us now consider the mesh transfer function $\hat{\phi}_{k\ell}(g)$ evaluated from Eq. (72) at values of $g = n/N^{(\cdot)}\Delta$:

$$\hat{\phi}_{k\ell}(n/N^{(\cdot)}\Delta) = (-i)^{k+\ell}[(2k+1)(2\ell+1)]^{\frac{1}{2}}\left\{j_k\left(\frac{n}{N^{(\cdot)}}\,\frac{\pi FL}{A\Delta}\right)j_\ell\left(\frac{n}{N^{(\cdot)}}\,\frac{\pi L}{\Delta}\right)\right.$$

$$\left. - \sum_{\substack{n'=-\infty \\ \text{except} \\ n'=0}}^{\infty} j_0(n'\pi FL/A\Delta)j_0(n'\pi L/\Delta)j_k\left[\left(\frac{n}{N^{(\cdot)}} - n'\right)\frac{\pi FL}{A\Delta}\right]j_\ell\left[\left(\frac{n}{N^{(\cdot)}} - n'\right)\frac{\pi L}{\Delta}\right]\right\} . \tag{88}$$

At the tooth-meshing harmonics, which occur at integral values of $p = n/N^{(\cdot)}$, it was pointed out earlier that the exact value of $\hat{\phi}_{00}(p/\Delta)$ is zero except for $p = 0$ where $\hat{\phi}_{00}(0) = 1$, and furthermore that $\hat{\phi}_{00}$ can be modified to yield this behavior by retaining only one "correction term" in the summation over n'. For the rotational harmonics represented by Eq. (88), this modification can take the form

$$\hat{\phi}_{00}(n/N^{(\cdot)}\Delta) \approx j_0\left(\frac{n}{N^{(\cdot)}}\,\frac{\pi FL}{A\Delta}\right)j_0\left(\frac{n}{N^{(\cdot)}}\,\frac{\pi L}{\Delta}\right)$$

$$- \sum_{\substack{n'=-\infty \\ \text{except} \\ n'=0}}^{\infty} \left\{\text{rect}[(n/N^{(\cdot)})-n']j_0(n'\pi FL/A\Delta)j_0(n'\pi L/\Delta)\right.$$

$$\left. \times\, j_0\left[\left(\frac{n}{N^{(\cdot)}} - n'\right)\,\frac{\pi FL}{A\Delta}\right]j_0\left[\left(\frac{n}{N^{(\cdot)}} - n'\right)\frac{\pi L}{\Delta}\right]\right\} , \tag{89}$$

where rect x is the rectangular function [p. 29 of Ref. 16] defined as

$$\text{rect } x = \begin{cases} 1, & |x| < \frac{1}{2} \\ 0, & |x| \geq \frac{1}{2} \end{cases} . \tag{90}$$

From Eq. (90) we see that for any rotational harmonic n, only one term in the summation in Eq. (89) can contribute — the term for which $|(n/N^{(\cdot)})-n'| < 1/2$. Moreover, when n falls in the range $|n/N^{(\cdot)}| \leq 1/2$, none of the terms in the summation in Eq. (89) contribute. It follows, therefore, that when Eq. (89) is evaluated at the tooth-meshing harmonics, which occur at integer values of $n/N^{(\cdot)}$, it satisfies exactly the condition of Eq. (78).

The right-hand side of Eq. (89) will display (small) discontinuities at values of n in the neighborhoods of $[(n/N^{(\cdot)})-n'] = 1/2$ for all n'. These discontinuities can be removed by replacing rect $[(n/N^{(\cdot)})-n']$ in Eq. (89) by a function that smoothly increases and decreases the weighting of each term. A function ideally suited for this purpose is

$$w_{00}[(n/N^{(\cdot)})-n'] \triangleq \frac{1}{2} \text{rect}\{\tfrac{1}{2}[(n/N^{(\cdot)})-n']\}(1+\cos\{\pi[(n/N^{(\cdot)})-n']\}). \tag{91}$$

When rect$[(n/N^{(\cdot)})-n']$ is replaced in Eq. (89) by Eq. (91), we see that whenever $n/N^{(\cdot)}$ is not an integer, we generally will have two terms in the summation over n' providing nonzero contributions. However, the condition of Eq. (78) still will be satisfied exactly.

Let us turn now to the general case where k and ℓ are not both zero. Here, except in the vicinity of g = 0 where Eq. (80) must be satisfied, we have no reason for not retaining all of the terms in Eq. (72). The requirement of Eq. (80) can be satisfied while avoiding discontinuous behavior by multiplying the summation in Eq. (72) by

$$w(\Delta g) \triangleq \begin{cases} \frac{1}{2}\,\mathrm{rect}(\Delta g/2)[1-\cos(\pi\Delta g)], & |\Delta g| < 1 \\ 1, & |\Delta g| \geq 1 \end{cases} \quad (92)$$

which increases smoothly from zero at $g = 0$ to unity at $|g| = 1/\Delta$, which is the position of the first tooth-meshing harmonic where no modification to the summation in Eq. (72) is sought. For values of $|g| \geq 1/\Delta$, Eq. (92) provides no modification to the summation in Eq. (72).

We may now collect the above modifications of Eq. (72) into a general formula that is applicable to both the mean and the random deviation components and that satisfies the requirements of Eqs. (78) and (80). Setting $n/N^{(\cdot)}$ equal to the product Δg in Eq. (91) gives

$$w_{00}(\Delta g - n') \triangleq \frac{1}{2}\,\mathrm{rect}[\tfrac{1}{2}(\Delta g - n')]\{1+\cos[\pi(\Delta g - n')]\} . \quad (93)$$

If we now define the general weighting function

$$w_{k\ell}(\Delta g, n') \triangleq \begin{cases} w_{00}(\Delta g - n'), & k = 0,\ \ell = 0 \\ w(\Delta g), & \text{otherwise} \end{cases} , \quad (94)$$

where $w(\Delta g)$ and $w_{00}(\Delta g - n')$ are defined by Eqs. (92) and (93) respectively, we then have for our general modification of Eq. (72):

$$\hat{\phi}_{k\ell}(g) \approx (-i)^{k+\ell}[(2k+1)(2\ell+1)]^{\frac{1}{2}}\Bigg(j_k(\pi gFL/A)j_\ell(\pi gL) - \sum_{\substack{n'=-\infty \\ \text{except} \\ n'=0}}^{\infty} \{w_{k\ell}(\Delta g, n')j_0(n'\pi FL/A\Delta)j_0(n'\pi L/\Delta) \times j_k[(\Delta g - n')\pi FL/A\Delta]j_\ell[(\Delta g - n')\pi L/\Delta]\}\Bigg), \quad (95)$$

which may be used to evaluate $\hat{\phi}_{k\ell}$ in Eqs. (48), (52), and (87).

Constant tooth-pair stiffness formulas for spur gears

Since helical gears become spur gears when the helix angle is zero, the above formulas can be reduced to the case of spur gears by setting (L/A) = 0 as indicated by Eq. (C4) of Ref. 1. The resulting spur gear formulas — which are applicable to the case $K_{TC}(y,z) = \bar{K}_{TC}$ — are summarized below. Formulas requiring transfer functions $\hat{\phi}_{k\ell}(g)$ must be regarded as rough approximations only when the approximations given below for the $\hat{\phi}_{k\ell}(g)$ are used, since these formulas have been evaluated from the approximation M = 1 in Eq. (71) of Ref. 1 — see Table 1.

Fourier-series coefficients of mesh stiffness and load-dependent component. For use in Eqs. (68), (77), and (87) of Ref. 1 for calculating the Fourier-series coefficients of the load-dependent component of the static transmission error, we have for spur gears instead of Eq. (69):

$$(\alpha_{Kn}/\bar{K}_T) = \frac{\sin(n\pi L/\Delta)}{n\pi L/\Delta} \quad . \tag{96}$$

For the case where M = 1 in our approximation of the reciprocal mesh stiffness given by Eq. (71) of Ref. 1, we may obtain from Eqs. (70) and (71) a rough approximation for the Fourier-series coefficients of the load-dependent component of the static transmission error applicable to the case of spur gears:

$$\alpha_{Wn} \approx (W_0/\bar{K}_T)\left[2\delta_{n,0} - \frac{\sin(n\pi L/\Delta)}{n\pi L/\Delta}\right], \tag{97}$$

or

$$\alpha_{W0} \approx W_0/\bar{K}_T \tag{98a}$$

$$\alpha_{Wn} \approx -(W_0/\bar{K}_T)\frac{\sin(n\pi L/\Delta)}{n\pi L/\Delta} \quad , \qquad n \neq 0. \tag{98b}$$

Mesh transfer functions. For spur gears, the mesh transfer function of Eq. (72) reduces to

$$\hat{\phi}_{0\ell}(g) = (-i)^{\ell}(2\ell+1)^{\frac{1}{2}}\left\{ j_{\ell}(\pi gL) - \sum_{\substack{n'=-\infty \\ \text{except} \\ n'=0}}^{\infty} j_0(n'\pi L/\Delta) j_{\ell}[(\Delta g - n')\pi L/\Delta] \right\} \tag{99a}$$

and

$$\hat{\phi}_{k\ell}(g) = 0, \quad k \neq 0. \tag{99b}$$

In view of the fact that the above result was obtained using the approximation M = 1, the above formula should be used for rough calculations only. Furthermore, the reduction of Eq. (95) to the case of spur gears [given below by Eq. (110)] will give results generally superior to those provided by Eq. (99).

Fourier-series coefficients of mean deviation components. Equation (50) expresses the Fourier-series coefficients of the mean deviation component of the transmission error from gear (•) in terms of the expansion coefficients $a_{0\ell}^{(\bullet)}$ and the mesh transfer function $\hat{\phi}_{0\ell}(n/\Delta)$. From Fig. 4 of Ref. 1 and Eqs. (73) and (74), we see that these expansion coefficients actually characterize the *axial average* $\bar{m}_C^{(\bullet)}(z)$ of the mean deviation $m_C^{(\bullet)}(y,z)$ of the tooth faces on gear (•) from perfect involute surfaces with zero helix angles — i.e.,

$$\bar{m}_C^{(\bullet)}(z) \triangleq \frac{1}{F} \int_{-F/2}^{F/2} m_C^{(\bullet)}(y,z)dy \ . \tag{100}$$

To show this, we divide Eq. (73) by F, integrate over y between -F/2 and F/2, and then use the orthogonality of the Legendre polynomials and the fact that $P_0(2y/F) = 1$ — thereby yielding

$$\bar{m}_C^{(\bullet)}(z) = \sum_{\ell=0}^{\infty} a_{0\ell}^{(\bullet)}(2\ell+1)^{\frac{1}{2}} P_{\ell}(2z/D) \ . \tag{101}$$

From Eqs. (74) and (100) and the fact that $P_0(2y/F) = 1$, we then have

$$a_{0\ell}^{(\cdot)} = \frac{(2\ell+1)^{\frac{1}{2}}}{D} \int_{-D/2}^{D/2} \bar{m}_C^{(\cdot)}(z)\, P_\ell(2z/D)dz \ . \tag{102}$$

Finally, by squaring both sides of Eq. (101), then dividing the resulting expression by D and integrating over z between -D/2 and D/2, and using the fact that

$$\frac{(2\ell+1)}{D} \int_{-D/2}^{D/2} [P_\ell(2z/D)]^2 dz = 1 \ , \tag{103}$$

we see that the expansion coefficients $a_{0\ell}^{(\cdot)}$ must satisfy

$$\frac{1}{D} \int_{-D/2}^{D/2} [\bar{m}_C^{(\cdot)}(z)]^2 dz = \sum_{\ell=0}^{\infty} (a_{0\ell}^{(\cdot)})^2 . \tag{104}$$

Equations (50) and (100) to (104) show that the axial average $\bar{m}_C^{(\cdot)}(z)$ of the mean deviation $m_C^{(\cdot)}(y,z)$ of the tooth faces on gear (·) is the appropriate *tooth profile metric* for computation of the Fourier-series coefficients of the mean deviation transmission error components in the case of spur gears. See Fig. 4 of Ref. 1.

Fourier-series coefficients and power spectra of random deviation components. In the case of spur gears, Eq. (55) expresses the Fourier-series coefficients of the random deviation transmission error component from gear (·) in terms of the mesh transfer functions $\hat{\phi}_{0\ell}(n/N^{(\cdot)}\Delta)$ and the discrete Fourier transforms $B_{0\ell}^{(\cdot)}(n)$ of the expansion coefficients $b_{j,0\ell}^{(\cdot)}$ as defined by Eq. (53). In this case, we see from Eqs. (81) and (82) that the expansion coefficients $b_{j,0\ell}^{(\cdot)}$ characterize the *axial average* $\bar{\varepsilon}_{Cj}^{(\cdot)}(z)$ of the random deviation component $\varepsilon_{Cj}^{(\cdot)}(y,z)$ from tooth face j on gear (·) — i.e.,

$$\bar{\varepsilon}_{Cj}^{(\cdot)}(z) \triangleq \int_{-F/2}^{F/2} \varepsilon_{Cj}^{(\cdot)}(y,z)dy \ . \tag{105}$$

That is, from Eqs. (81) and (82) we may show in a manner completely analogous to that used above for the mean deviation component that $\bar{\varepsilon}_{Cj}^{(\cdot)}(z)$ is given in terms of the expansion coefficients $b_{j,0\ell}^{(\cdot)}$ by

$$\bar{\varepsilon}_{Cj}^{(\cdot)}(z) = \sum_{\ell=0}^{\infty} b_{j,0\ell}^{(\cdot)}(2\ell+1)^{\frac{1}{2}} P_\ell(2z/D) \ , \tag{106}$$

where the $b_{j,0\ell}^{(\cdot)}$ are obtained using

$$b_{j,0\ell}^{(\cdot)} = \frac{(2\ell+1)^{\frac{1}{2}}}{D} \int_{-D/2}^{D/2} \bar{\varepsilon}_{Cj}^{(\cdot)}(z) \ P_\ell(2z/D)dz \ , \tag{107}$$

and where the $b_{j,0\ell}^{(\cdot)}$ satisfy

$$\frac{1}{D} \int_{-D/2}^{D/2} \left[\bar{\varepsilon}_{Cj}^{(\cdot)}(z)\right]^2 dz = \sum_{\ell=0}^{\infty} (b_{j,0\ell})^2 . \tag{108}$$

Hence, in the case of spur gears, the axial averages $\bar{\varepsilon}_{Cj}^{(\cdot)}(z)$ of the random deviation components $\varepsilon_{Cj}^{(\cdot)}(y,z)$ of the tooth faces on gear $(\cdot)$ are the appropriate metrics for computation of the Fourier-series coefficients of the rotational harmonics of the transmission error from gear $(\cdot)$.

Equations (137) to (140) of Ref. 1 express the discrete power spectrum $|\alpha_{rn}^{(\cdot)}|^2$ of the random deviation transmission error component for spur gears as well as for helical gears. However, in the case of spur gears, the *one-dimensional* sequence of expansion coefficients $b_{j,0\ell}^{(\cdot)}$, $\ell = 0,1,2,\cdots$ characterizes the

errors on tooth j as noted above; hence, for spur gears we may directly replace the index m in Eqs. (137) to (140) of Ref. 1 by the index ℓ. For a specific error component designated by the index ℓ, Eqs. (84) to (87) apply to the spur gear case also by setting k = 0 as above. As in the helical gear case, when several random error components, 0ℓ are present, cross-spectrum terms must be included to obtain all contributions to $|\alpha_{rn}^{(\cdot)}|^2$ as indicated by Eq. (140) of Ref. 1 unless these various random error components are uncorrelated.

Modified forms of mesh transfer functions. In the case of spur gears, the first form of our modified mesh transfer function for tooth-spacing errors is obtained from Eq. (89) by setting (L/A) = 0:

$$\hat{\phi}_{00}(n/N^{(\cdot)}\Delta) \approx j_0\left(\frac{n}{N^{(\cdot)}}\frac{\pi L}{\Delta}\right)$$

$$-\sum_{\substack{n'=-\infty \\ \text{except} \\ n'=0}}^{\infty}\left\{\text{rect}[(n/N^{(\cdot)})-n']j_0(n'\pi L/\Delta)j_0\left[\left(\frac{n}{N^{(\cdot)}}-n'\right)\frac{\pi L}{\Delta}\right]\right\}, \qquad (109)$$

where the rect function is defined by Eq. (90). As in the case of Eq. (89), Eq. (109) will display small discontinuities at values of n in the neighborhoods of $|(n/N^{(\cdot)})-n'| = \frac{1}{2}$ for all n'. These discontinuities will be more pronounced for spur gears than for helical gears. To remove these discontinuities, we can substitute for the rect function in Eq. (109) the weighting function of Eq. (91). When this substitution is made, and when appropriate adjustment is made for the behavior of $\hat{\phi}_{k\ell}(g)$ near g = 0 as in the helical gear case, our general form of modified mesh transfer function given by Eq. (95) reduces in the case of spur gears [k=0 and (L/A)=0] to

$$\hat{\phi}_{0\ell}(g) \approx (-i)^{\ell}(2\ell+1)^{\frac{1}{2}}\left(j_\ell(\pi gL)\right.$$

$$\left.-\sum_{\substack{n'=-\infty \\ \text{except} \\ n'=0}}^{\infty}\{w_{0\ell}(\Delta g,n')j_0(n'\pi L/\Delta)j_\ell[(\Delta g-n')\pi L/\Delta]\}\right) \qquad (110a)$$

and

$$\hat{\phi}_{k\ell}(g) = 0, \qquad k \neq 0 , \tag{110b}$$

where the weighting function $w_{0\ell}(\Delta g,n')$ is defined by Eq. (94). Equation (110) is the preferred form of $\hat{\phi}_{0\ell}(g)$ applicable for rough calculations involving spur gears for all situations requiring the mesh transfer functions.

APPLICATION

We now illustrate the above techniques by predicting the various components of the static transmission error spectrum from a set of measurements made on a mating pair of spur gears. Effects of variations in the axial contact ratios of helical gears also are illustrated. Gear parameters required in the computations are listed below in Table II.

TABLE II. - GEAR PARAMETERS

	Gear (1)	Gear (2)
Number of Teeth	50	53
Pressure Angle	0.3491 rad (20°)	0.3491 rad (20°)
Outside Diameter	0.1328 m (5.230 in.)	0.1405 m (5.530 in.)
Pitch Diameter	0.1270 m (5.000 in.)	0.1346 m (5.300 in.)
Base Circle Diameter	0.1193 m (4.698 in.)	0.1265 m (4.980 in.)

From the above parameters, we must compute L, Δ, and D. From Eqs. (D11) and (D12) of Ref. 1, we find $L^{(1)}$ = 0.007457 m (0.2936 in.), $L^{(2)}$ = 0.007503 m (0.2954 in.); hence, $L' = L^{(1)}+L^{(2)}$ = 0.01496 m (0.5890 in.). However, the above computation does not account for tip rounding. Subtracting 0.00132 m (0.0520 in.) from the above value of L' to get the true value of path of contact length L illustrated in Fig. D-1 of Ref. 1, we obtain

$$L = 0.01364 \text{ m } (0.5370 \text{ in.}). \quad (111)$$

The base pitch Δ is $2\pi R_b/N$ where R_b is the base circle radius and N is the number of teeth — both quantities taken on the same gear. Using the above parameters from either gear, we find

$$\Delta = 0.007498 \text{ m } (0.2952 \text{ in.}). \quad (112)$$

Finally, using Eq. (C8) of Ref. 1, $D = L\sin\phi$, where ϕ is the pressure angle, we find

$$D = 0.004665 \text{ m } (0.1837 \text{ in.}). \quad (113)$$

Mesh-Attenuated Tooth-Spacing Error Spectra

Figures 3 to 14 display the steps involved in computing the discrete power spectra $|\alpha_{rn}^{(\cdot)}|_{00}^2$ from the tooth-spacing errors of gears (1) and (2), where $|\alpha_{rn}^{(\cdot)}|_{00}^2$ is defined by Eq. (87) with $k = 0$ and $\ell = 0$.

Tooth-spacing errors

Figures 3 and 6 show the tooth-spacing errors of gears (1) and (2). The abscissa of Figs. 3 and 6 is tooth number j and the ordinate is tooth-spacing error measured in micrometers (mu m). Two sets of data are shown in each figure. The lower curve in each figure displays the accumulated tooth-spacing errors, which are the errors in tooth-face positions measured as a function of tooth number on the base circle from the position of an arbitrary tooth designated as tooth number zero. The lower curves are discontinuous because only one accumulated tooth-spacing error is associated with each tooth on a gear. Notice — e.g., in the case of Fig. 3, which applies to the 50 tooth gear — that tooth numbers 0 and 50 have the same accumulated errors because they are the same tooth. The upper curves in Figs. 3 and 6 are tooth-to-tooth errors in tooth spacing. Therefore, these upper curves display the magnitudes of the jumps in the lower curves. The accumulated error curves shown in Figs. 3 and 6 are computer plots of similar curves that were obtained from measurements made on gears (1) and (2). Procedures for making such measurements are well known — e.g., see pp. 77-78 of Ref. 6.

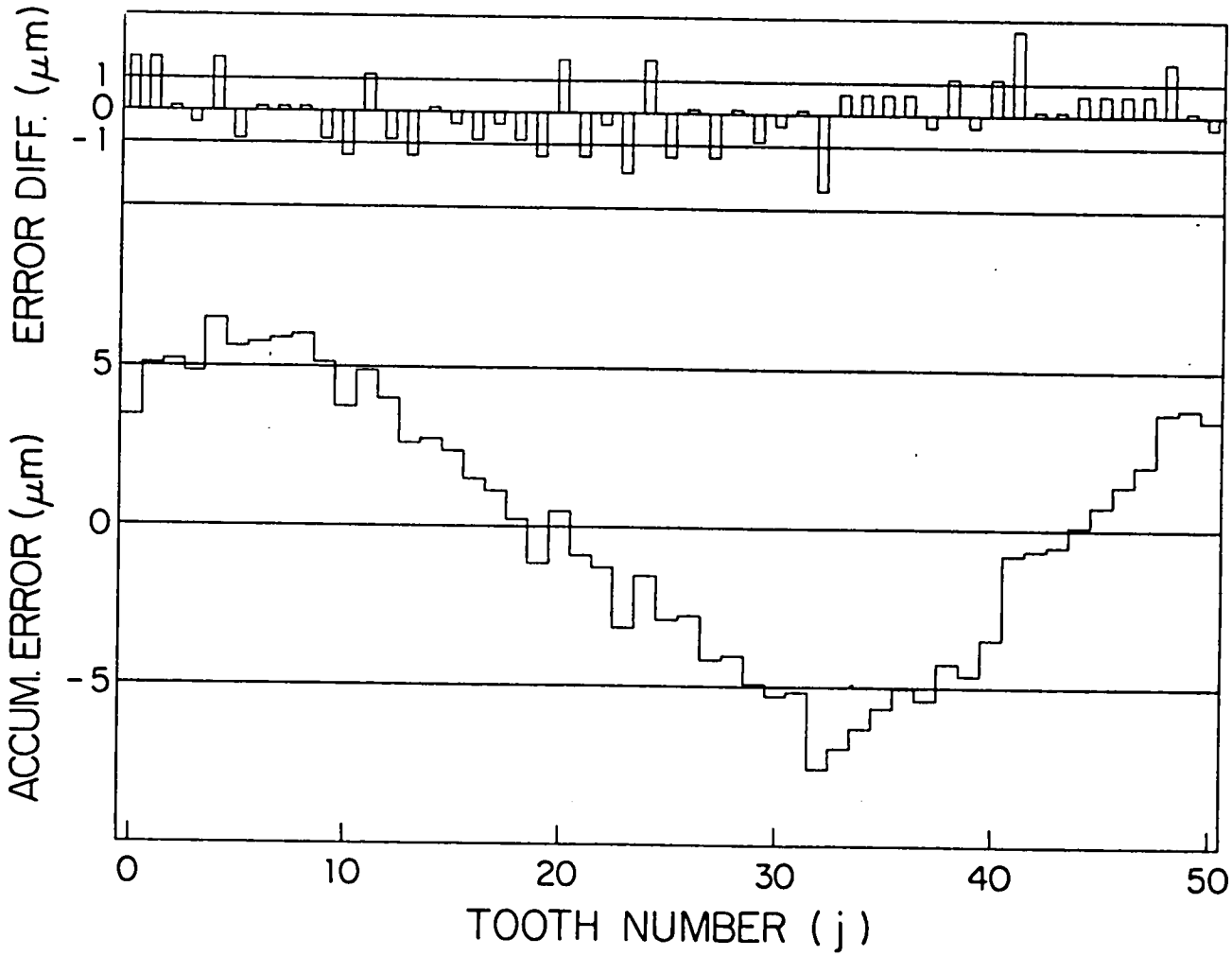

FIGURE 3. TOOTH-SPACING ERRORS OF GEAR (1).

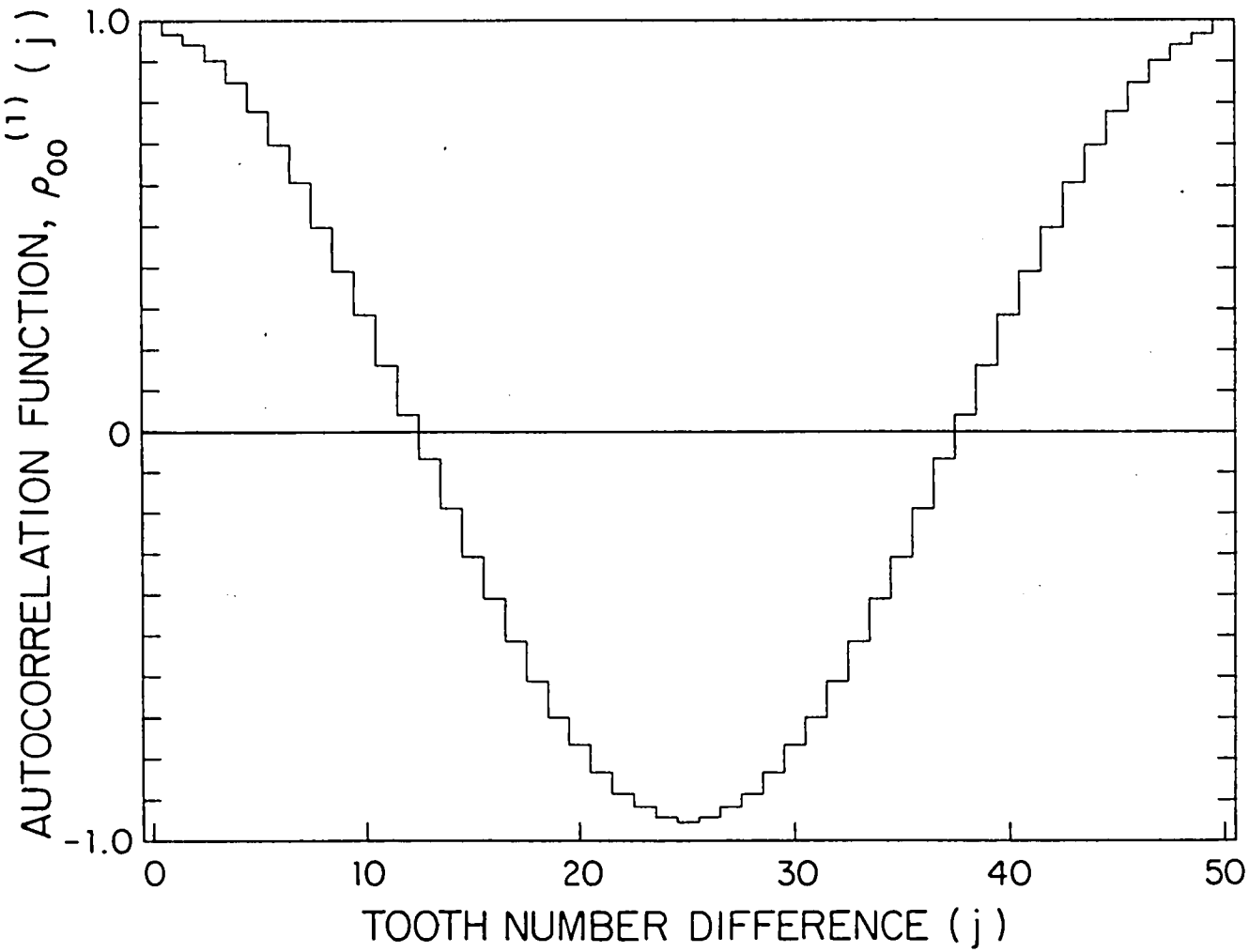

FIGURE 4. NORMALIZED TOOTH-SPACING ERROR AUTOCORRELATION FUNCTION OF GEAR (1).

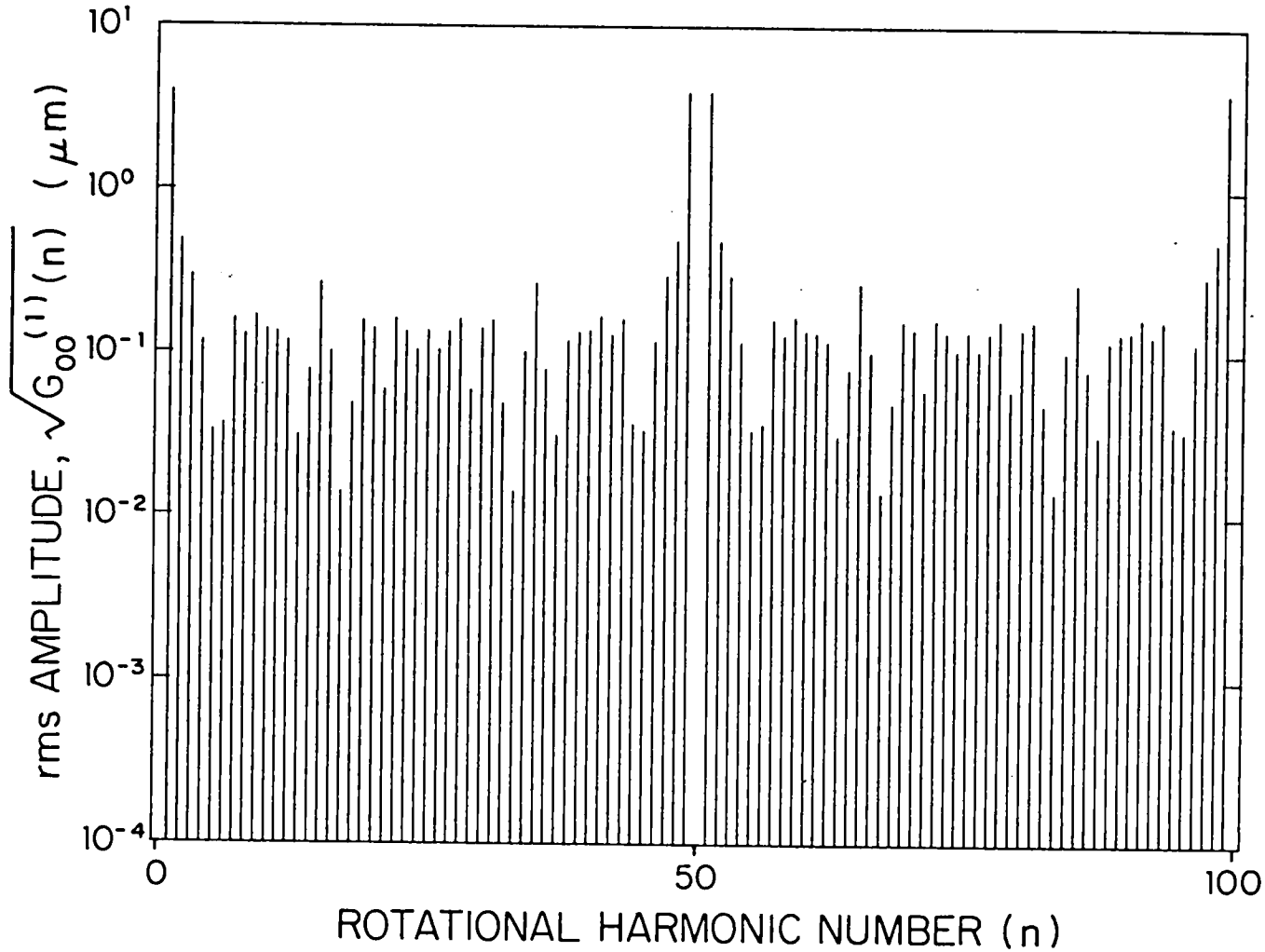

FIGURE 5. TOOTH-SPACING ERROR rms HARMONIC AMPLITUDES OF GEAR (1).

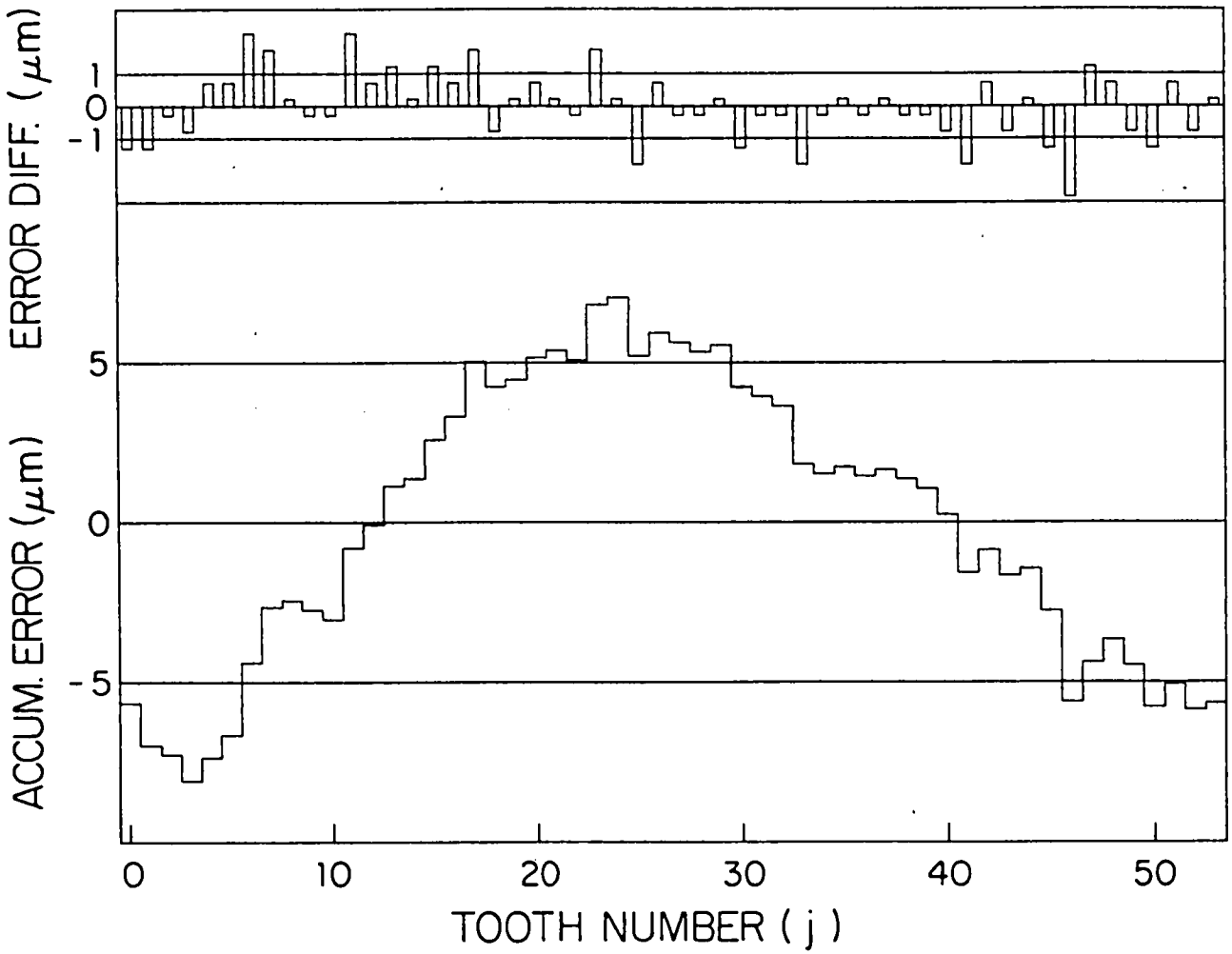

FIGURE 6. TOOTH-SPACING ERRORS OF GEAR (2).

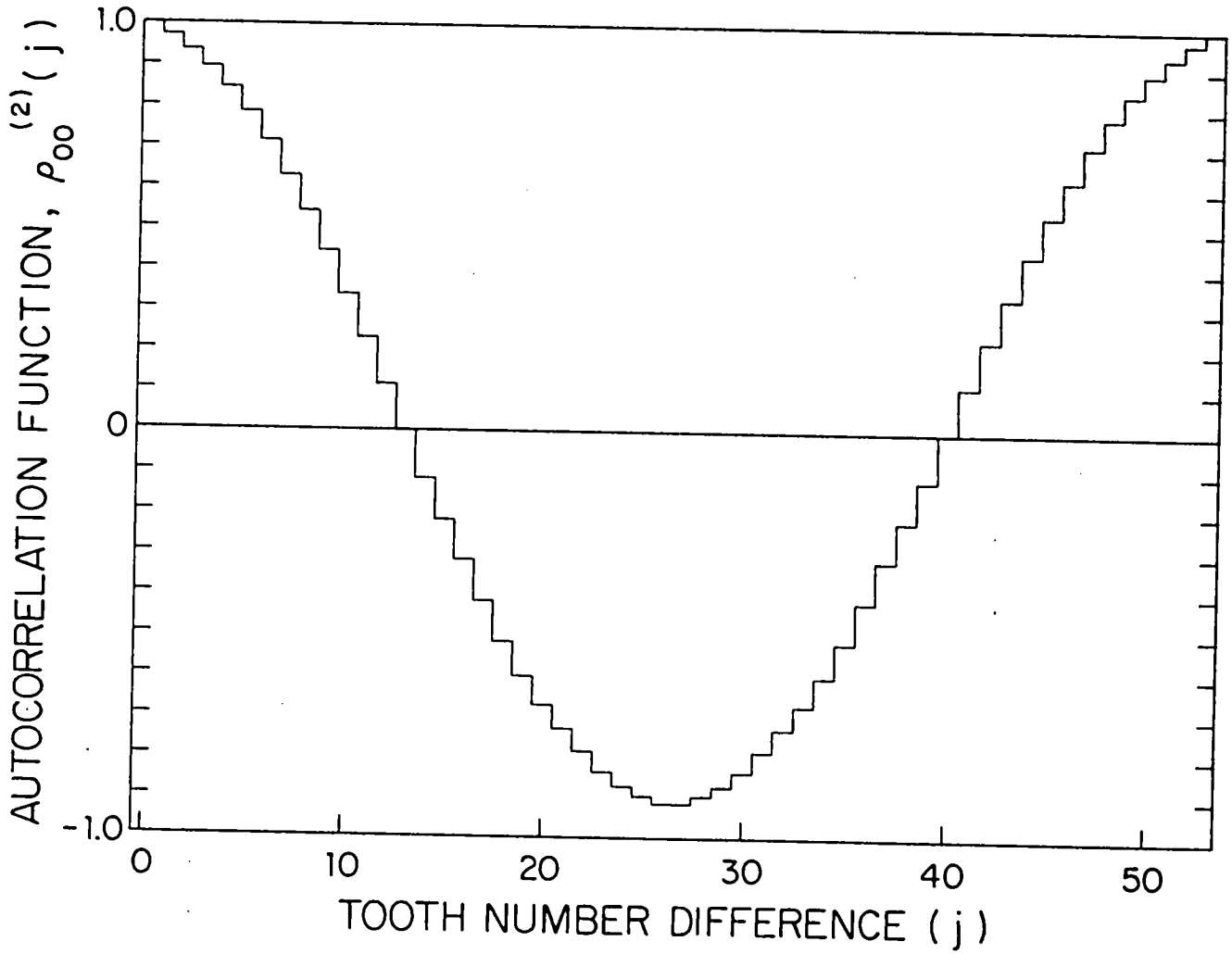

FIGURE 7. NORMALIZED TOOTH-SPACING ERROR AUTOCORRELATION FUNCTION OF GEAR (2).

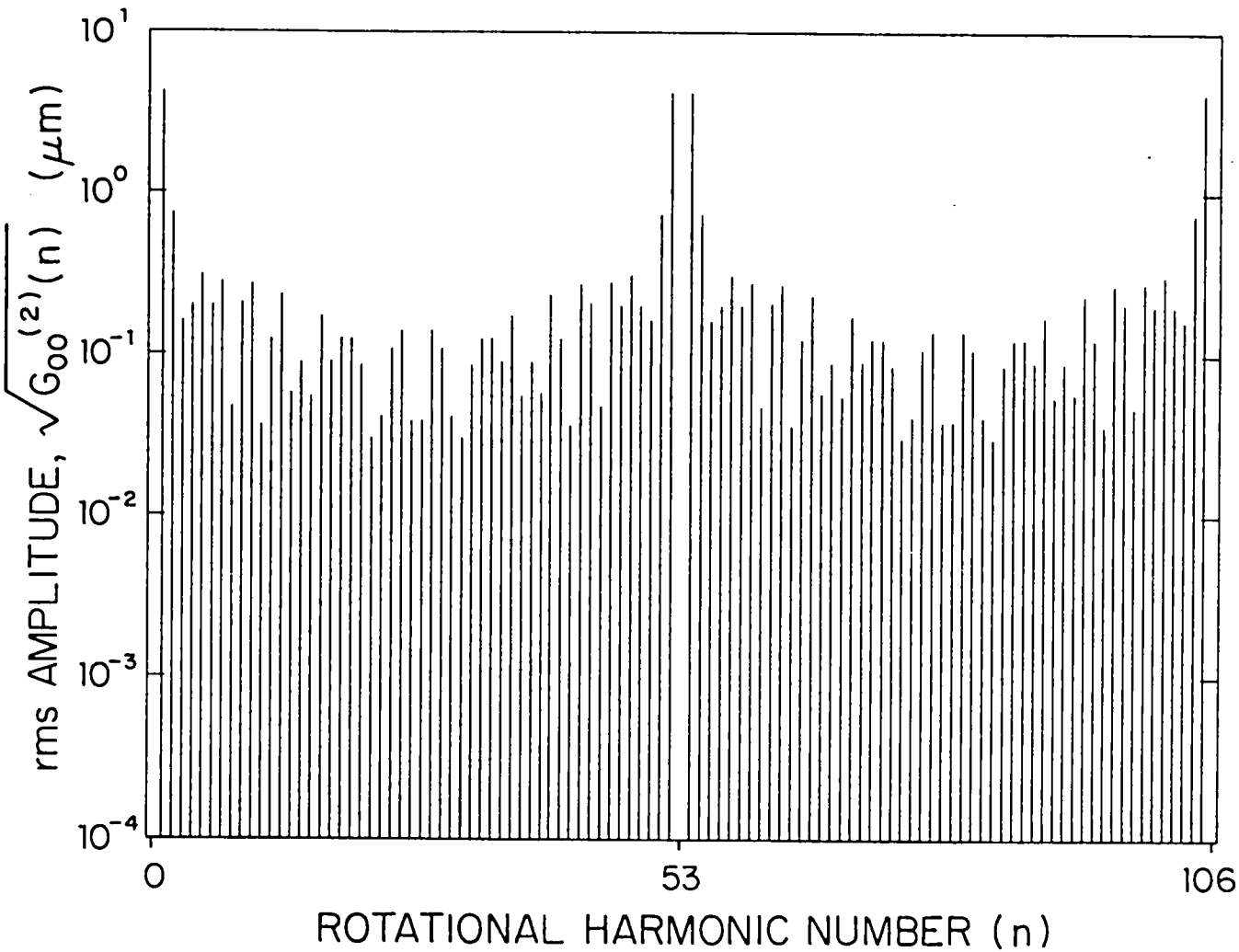

FIGURE 8. TOOTH-SPACING ERROR rms HARMONIC AMPLITUDES OF GEAR (2).

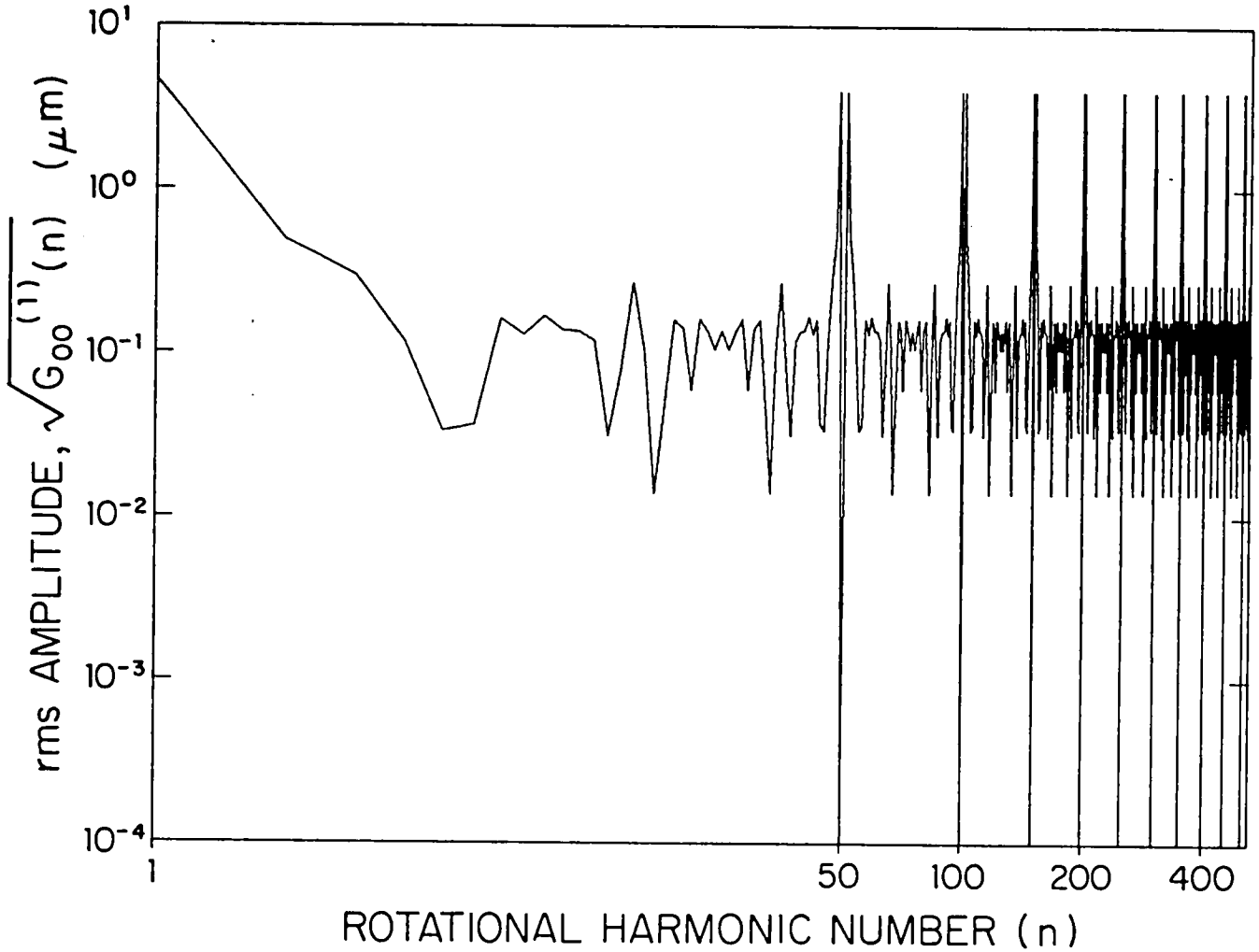

FIGURE 9. ENVELOPE OF TOOTH-SPACING ERROR rms HARMONIC AMPLITUDES OF GEAR (1) ON LOGARITHMIC COORDINATES.

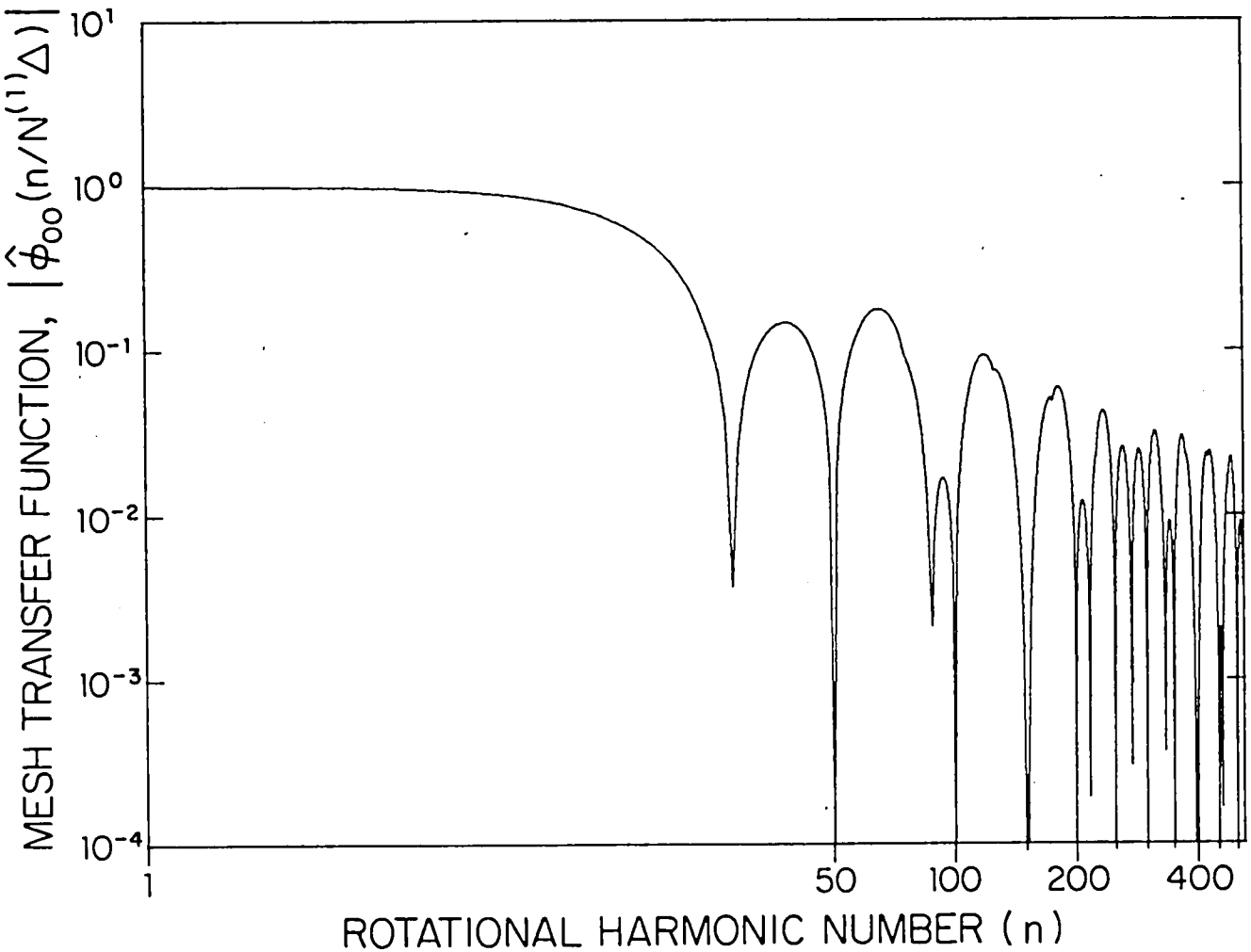

FIGURE 10. TOOTH-SPACING ERROR MESH TRANSFER FUNCTION OF GEAR (1).

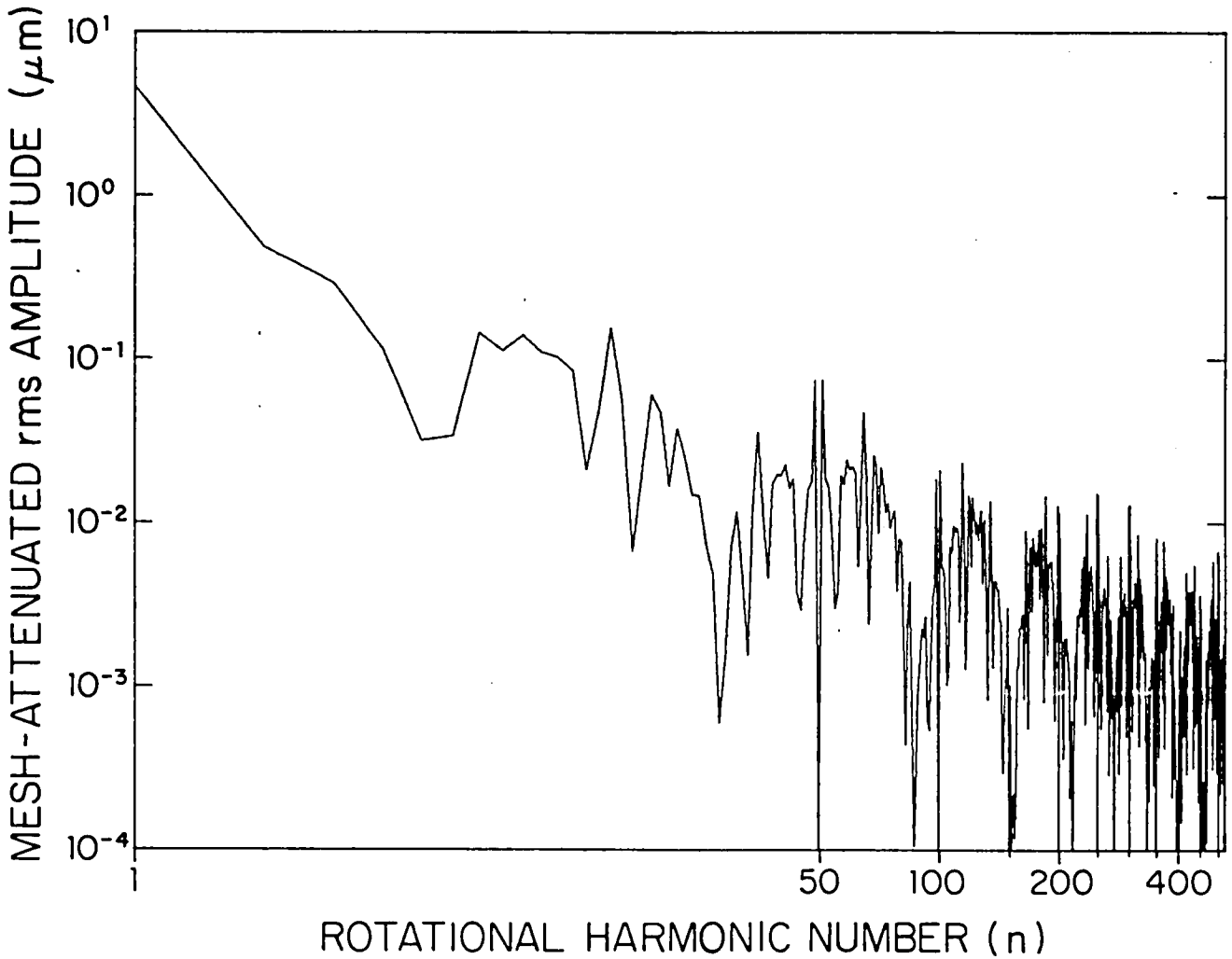

FIGURE 11. ENVELOPE OF MESH-ATTENUATED TOOTH-SPACING ERROR rms HARMONIC AMPLITUDES OF GEAR (1).

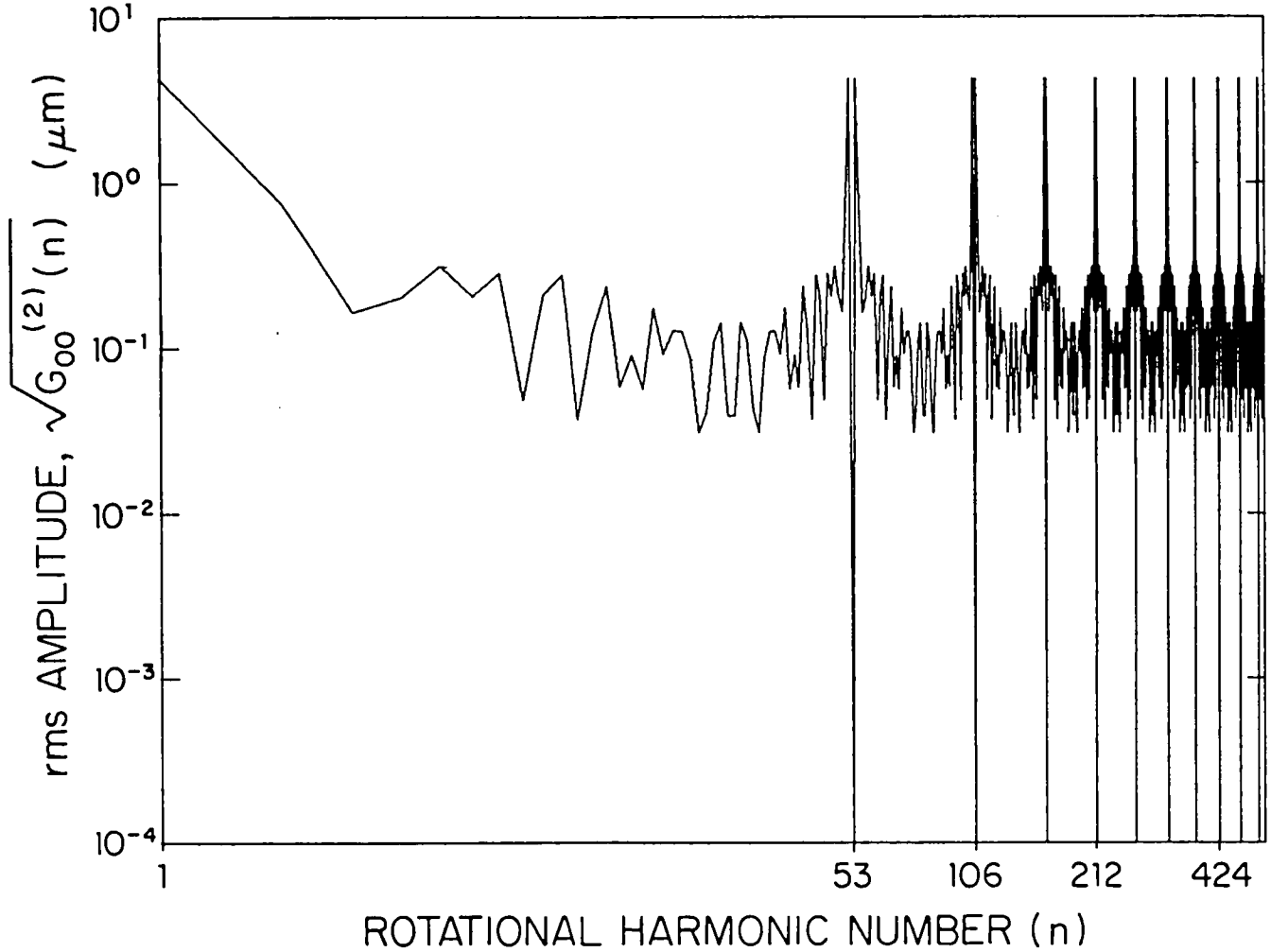

FIGURE 12. ENVELOPE OF TOOTH-SPACING ERROR rms HARMONIC AMPLITUDES OF GEAR (2) ON LOGARITHMIC COORDINATES.

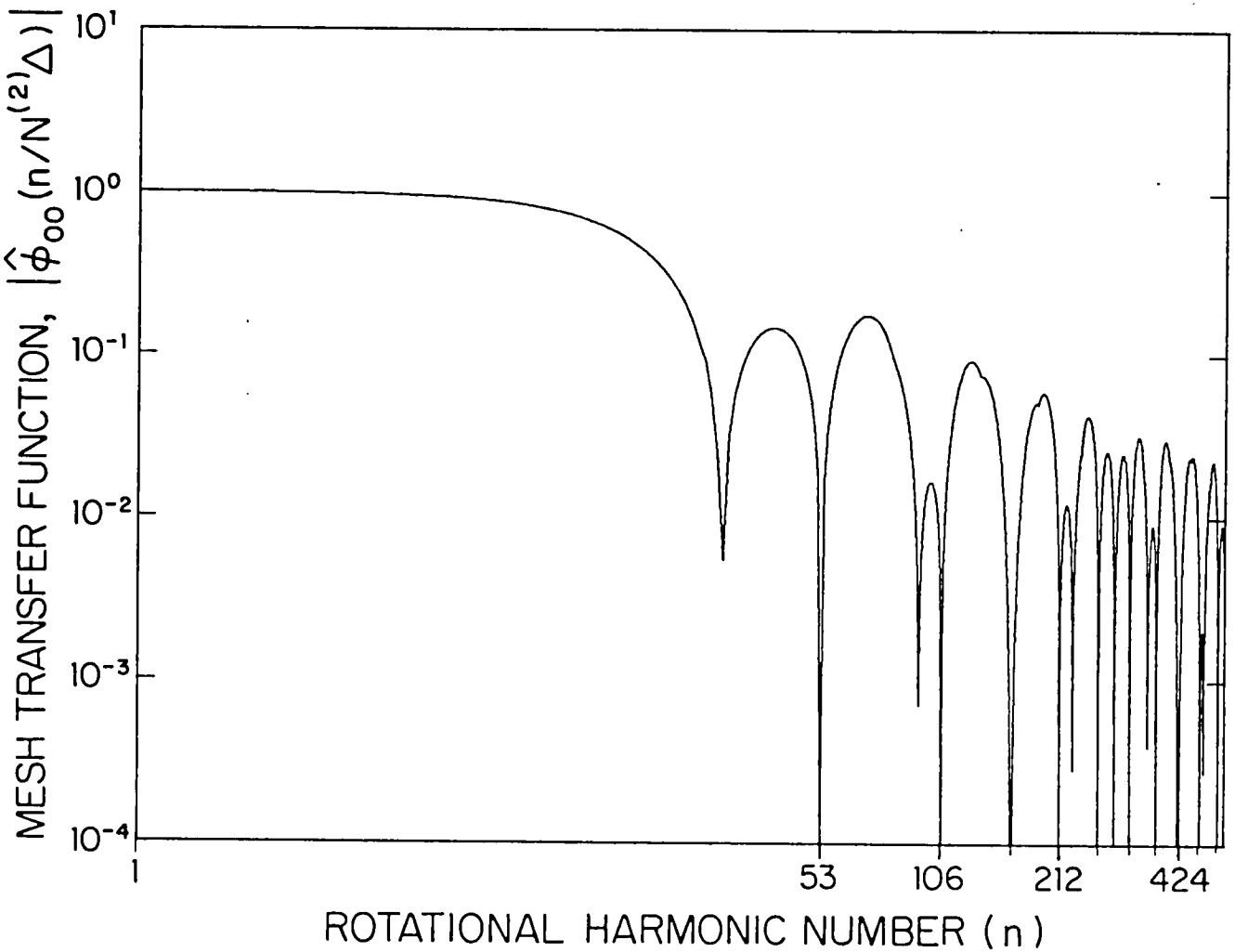

FIGURE 13. TOOTH-SPACING ERROR MESH TRANSFER FUNCTION OF GEAR (2).

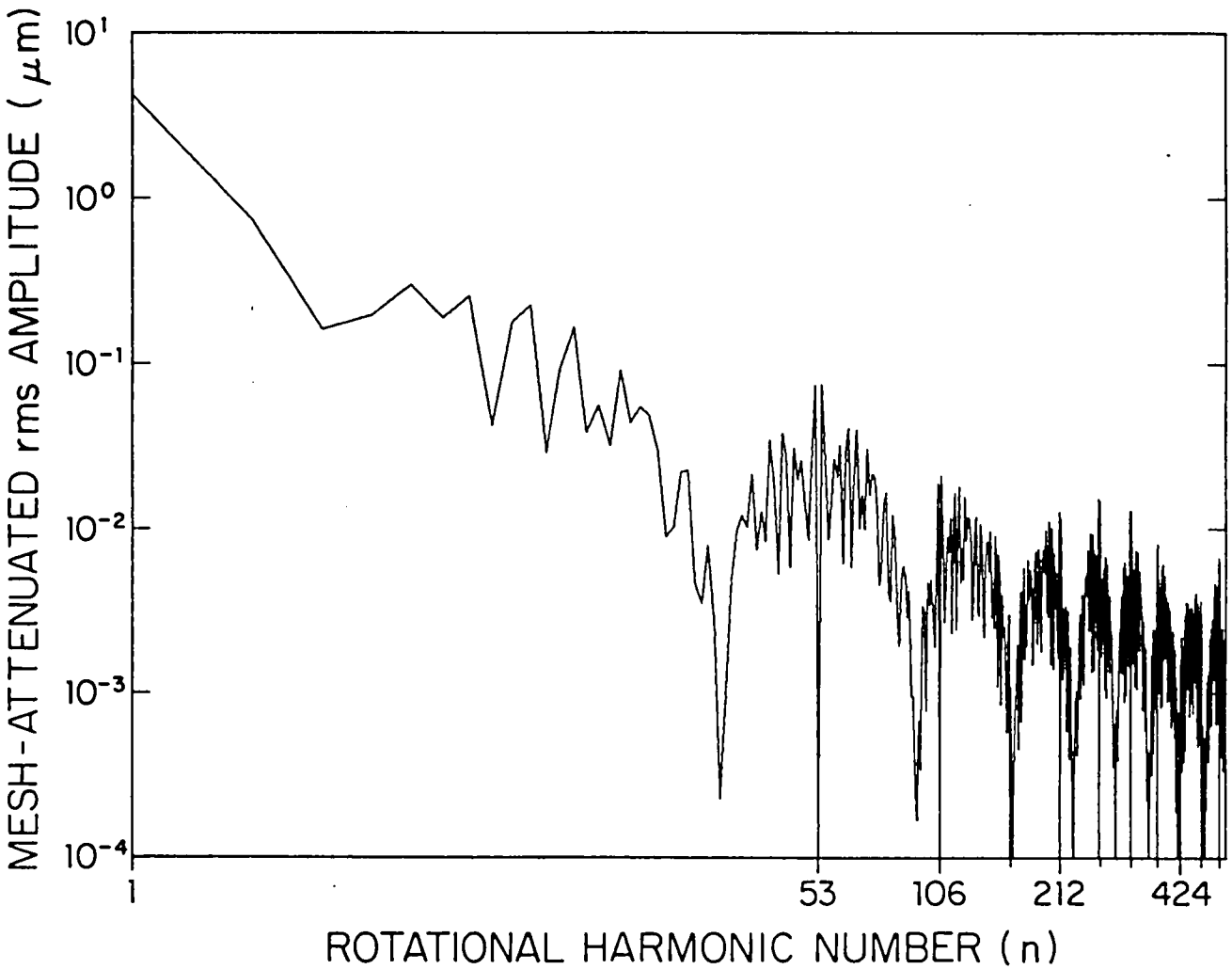

FIGURE 14. ENVELOPE OF MESH-ATTENUATED TOOTH-SPACING ERROR rms HARMONIC AMPLITUDES OF GEAR (2).

In Figs. 3 and 6, the origins of the ordinates of the accumulated error plots were chosen so that the average accumulated tooth-spacing error on each gear is zero. Thus, these plots represent *random* deviation components. In fact, if we interpret the tooth-spacing errors as measurements of the errors in the mean positions of the tooth faces, then we may identify the accumulated error of a generic tooth j on gear (•) with the expansion coefficient $b_{j,00}^{(\bullet)}$ – see Eqs. (82) and (107) and recall that $P_0(x) = 1$. Also see Eq. (50) of Ref. 1. Hence, the accumulated error plots in Figs. 3 and 6 satisfy

$$\frac{1}{N^{(\bullet)}} \sum_{j=0}^{N^{(\bullet)}-1} b_{j,00}^{(\bullet)} = 0 \ . \tag{114}$$

Because of the circular nature of the gears, we must define the tooth-spacing errors so that

$$b_{p\,N^{(\bullet)}+j,00}^{(\bullet)} = b_{j,00}^{(\bullet)}, \qquad p = 0, \pm 1, \pm 2, \cdots . \tag{115}$$

Equations (84) to (87) can be used with $k = 0$, $\ell = 0$ to compute the tooth-spacing error contribution $|\alpha_{rn}^{(\bullet)}|_{00}^2$ to the discrete spectrum of the static transmission error of gear (•). To carry out this computation, we require the mean-square tooth-spacing errors defined by Eq. (84) with $k = 0$, $\ell = 0$. These values were computed from the accumulated errors shown in Figs. 3 and 6 and are

$$\overline{(b_{00}^{(1)})^2} = 16.69 \text{ (Mu meters)}^2, \qquad \overline{(b_{00}^{(2)})^2} = 19.17 \text{ (Mu meters)}^2; \tag{116a,b}$$

hence, the corresponding rms accumulated errors are 4.085 and 4.378 mu meters respectively, which are consistent with the general appearance of Figs. 3 and 6.

Tooth-spacing error autocorrelation functions

We next require the normalized autocorrelation functions $\rho_{00}^{(\bullet)}(j)$ of the tooth-spacing errors, which are defined in terms

of the accumulated errors $b^{(\cdot)}_{j,00}$ by Eq. (85) with k = 0, ℓ = 0. Figures 4 and 7 show these autocorrealtion functions for gears (1) and (2) respectively. The ordinate of Figs. 4 and 7 is $\rho^{(\cdot)}_{00}(j)$ and the abscissa is tooth number *difference* j, as may be seen from Eq. (85). When the tooth number difference is zero, we may see from Eqs. (84) and (85) that $\rho^{(\cdot)}_{00}(0) = 1$. Moreover, because tooth number $N^{(\cdot)}$ is the same tooth as tooth number 0, we must have $\rho^{(\cdot)}_{00}(N^{(\cdot)}) = 1$, as we may also see from Figs. 4 and 7. Although the abscissas in Figs. 4 and 7 span only the range of values $0 \leq j \leq N^{(\cdot)}$, $\rho^{(\cdot)}_{00}(j)$ must satisfy

$$\rho^{(\cdot)}_{00}(pN^{(\cdot)}+j) = \rho^{(\cdot)}_{00}(j), \qquad p = 0, \pm 1, \pm 2, \cdots \tag{117}$$

because of the circular nature of the gears as indicated by Eq. (115). Furthermore, from Eq. (85) we see that

$$\rho^{(\cdot)}_{00}(-j) = \rho^{(\cdot)}_{00}(j) , \tag{118}$$

which when combined with Eq. (117) yields the symmetric character of Figs. 4 and 7. From Eqs. (85) and (114), we see that $\rho^{(\cdot)}_{00}(j)$ also must satisfy

$$\frac{1}{N^{(\cdot)}} \sum_{j=0}^{N^{(\cdot)}-1} \rho^{(\cdot)}_{00}(j) = 0. \tag{119}$$

The properties of Eqs. (114), (115), and (117) to (119) apply to all classes of random errors designated by the dual indices kℓ used in Eqs. (84) to (87).

Tooth-spacing error spectra

According to Eq. (87) applied to the case of tooth-spacing errors (k=0, ℓ=0), we require $\overline{(b^{(\cdot)}_{00})^2} S^{(\cdot)}_{00}(n)$ to characterize the tooth-spacing errors of gears (1) and (2) for later computation

of the mesh-attenuated error spectrum $|\alpha_{rn}^{(\cdot)}|_{00}^2$. However, since $|\alpha_{rn}^{(\cdot)}|_{00}^2$ is the tooth-spacing error contribution to a *two-sided* spectrum, as may be seen from Eqs. (109), (110), and (140) of Ref. 1, we have chosen to compute here for gears (1) and (2) the *one-sided* tooth-spacing error spectrum

$$G_{00}^{(\cdot)}(n) \triangleq 2\,\overline{(b_{00}^{(\cdot)})^2}\; S_{00}^{(\cdot)}(n) \;, \tag{120}$$

where $S_{00}^{(\cdot)}(n)$ is the finite discrete Fourier transform [*17*] of the normalized autocorrelation function $\rho_{00}^{(\cdot)}(j)$ as defined by Eq. (86) for $k = 0$ and $\ell = 0$. The *square roots* of $G_{00}^{(\cdot)}(n)$ for gears (1) and (2) are plotted in Figs. 5 and 8. Hence, the ordinate in Figs. 5 and 8 is a direct measure of the *rms values* of the various harmonic components of the tooth-spacing errors. To provide the capability for displaying a large range of values, we have plotted $[G_{00}^{(\cdot)}(n)]^{1/2}$ on a logarithmic scale of ordinates labeled in units of micrometers (mu m). The abscissa of Figs. 5 and 8 is rotational harmonic number n.

Figures 5 and 8 both are line spectra with fundamental harmonic number $n = 1$ corresponding to the fundamental rotational harmonic of each gear, which has a period equal to $N^{(\cdot)}\Delta$, the circumference of the base circle of gear $(\cdot)$. The spectra shown in Figs. 5 and 8 both are periodic in harmonic number with period equal to the number of teeth $N^{(\cdot)}$, which is $N^{(1)} = 50$ in the case of Fig. 5 and $N^{(2)} = 53$ in the case of Fig. 8. Two periods are shown in each figure. This periodic behavior is a general property of the spectra $S_{k\ell}^{(\cdot)}(n)$ defined by Eq. (86), which are periodic in n with period equal to the number of teeth $N^{(\cdot)}$. Periodic behavior of this type is a well-known property of the finite discrete Fourier transform [*17*] and follows from the fact that, for integer p, we have

$$\exp[-i2\pi(n+pN^{(\cdot)})j/N^{(\cdot)}] = \exp(-i2\pi nj/N^{(\cdot)}) \;, \tag{121}$$

which when substituted into Eq. (86) yields

$$S_{k\ell}^{(\cdot)}(n+pN^{(\cdot)}) = S_{k\ell}^{(\cdot)}(n) \;. \tag{122}$$

From Figs. 5 and 8, we notice that the harmonics located at $n = pN^{(\cdot)}$, $p = 0, \pm 1, \pm 2, \cdots$ are absent. This absence is a consequence of the periodic behavior of $S_{k\ell}^{(\cdot)}(n)$ described above, and the fact that for $n = 0$ we have from Eq. (86),

$$S_{k\ell}^{(\cdot)}(0) = \frac{1}{N^{(\cdot)}} \sum_{j=0}^{N^{(\cdot)}-1} \rho_{k\ell}^{(\cdot)}(j) \ , \tag{123}$$

which is zero for tooth-spacing errors, as may be seen from Eq. (119). This result is a special case of the general result proved in Appendix H of Ref. 1 — i.e., that the rotational harmonics from all random components of the static transmission error are zero at values of $n = pN^{(\cdot)}$, $p = 0, \pm 1, \pm 2, \cdots$, which are the fundamental and multiples of the *tooth-meshing* harmonics.

From Figs. 5 and 8, we notice that the fundamental harmonic $n = 1$ is nearly an order of magnitude larger than all other harmonics in the range $|n| < N^{(\cdot)}/2$, which is the point of symmetry in the first period of the spectra. This large fundamental reflects the fact that the accumulated tooth-spacing error curves in Figs. 3 and 6 appear almost sinusoidal with a single period — which also results in the almost sinusoidal behavior of the autocorrelation functions shown in Figs. 4 and 7. The almost sinusoidal appearance of the lower curves in Figs. 3 and 6 is typical of accumulated tooth-spacing error measurements — e.g., pp. 77-78 of Ref. 6 — and is the result of an eccentrically located axis of gear rotation in the error measurement or gear cutting operations.

The symmetric and periodic behavior of the discrete tooth-spacing error spectra shown in Figs. 5 and 8 gives rise to a repetition of the large low-order harmonics in the neighborhoods of the tooth-meshing harmonics, which occur at harmonic numbers $n = pN^{(\cdot)}$, $p = 0, \pm 1, \pm 2, \cdots$. The repetition of these low-order harmonics in the neighborhoods of the first two tooth-meshing harmonics, which occur in Figs. 5 and 8 at $n = 50$ and 100, and $n = 53$ and 106 respectively, is easily seen in the figures. This repetitive character of the spectra shown in Figs. 5 and 8 is a fundamental consequence of the mathematical form of Eq. (86) — which is a finite discrete Fourier transform. This form of Eq. (86) is a consequence of the fact that gears are circular with

finite numbers of discrete teeth — and is not the result of an approximate sampling procedure, which is the usual motivation for representing physical phenomena by the finite discrete Fourier transform. The repetition of the low-order harmonics in the neighborhoods of the tooth-meshing harmonics gives rise to the so-called sidebands, which are observed in experimentally obtained gear system vibration spectra [*18*].

The magnitudes of the strongest lines in Figs. 5 and 8 can be checked approximately using the Fourier mate to the finite discrete Fourier transform [*17*] of Eq. (86):

$$\rho_{k\ell}^{(\cdot)}(j) = \sum_{n=0}^{N^{(\cdot)}-1} S_{k\ell}^{(\cdot)}(n) \exp\left(\frac{i2\pi nj}{N^{(\cdot)}}\right) , \tag{124}$$

which gives, when evaluated at $j = 0$,

$$\rho_{k\ell}^{(\cdot)}(0) = \sum_{n=0}^{N^{(\cdot)}-1} S_{k\ell}^{(\cdot)}(n) = 1 , \tag{125}$$

where Eqs. (84) and (85) were used in arriving at the second equality. Let us suppose that all of the "power" in $S_{00}^{(\cdot)}(n)$ were in the fundamental $S_{00}^{(\cdot)}(1)$ and its equal sideband $S_{00}^{(\cdot)}(N^{(\cdot)}-1)$. From Eq. (125), we would have in this case $S_{00}^{(\cdot)}(1) = S_{00}^{(\cdot)}(N^{(\cdot)}-1) = 1/2$; hence, from Eq. (120), we have $G_{00}^{(\cdot)}(1) = G_{00}^{(\cdot)}(N^{(\cdot)}-1) = (b_{00}^{(\cdot)})^2$, which is the mean-square accumulated tooth-spacing error. The values of $[G_{00}^{(\cdot)}(1)]^{\frac{1}{2}}$ shown in Figs. 5 and 8 are slightly less than the rms errors $\left|(b_{00}^{(\cdot)})^2\right|^{\frac{1}{2}}$ of 4.085 and 4.378 Mu meters as predicted.

Figures 9 and 12 display the same infomration as Figs. 5 and 8, except that Figs. 9 and 12 show the *envelopes* of the line spectra shown in Figs. 5 and 8 on a logarithmic scale on the abscissa. Slightly over ten cycles of the periodic spectra are shown in Figs. 9 and 12. The ordinate axes of Figs. 5, 8, 9, and 12 all are plotted to the same logarithmic scale. Notice that Figs. 9 and 12 have discontinuous slopes with the discontinuities located at the positions of the rotational harmonics of each gear.

Mesh transfer functions for tooth-spacing errors

According to Eq. (87), we next require the mesh transfer function $\hat{\phi}_{00}(n/N^{(\cdot)}\Delta)$ in order to compute $|\alpha_{rn}^{(\cdot)}|_{00}^2$ for gears (1) and (2). Figures 10 and 13, which are nominally identical, display the magnitudes $|\hat{\phi}_{00}(n/N^{(\cdot)}\Delta)|$ of these transfer functions. The logarithmic scales of both axes in Figs. 10 and 13 are identical with those in Figs. 9 and 12.

Equation (109) was used to compute Figs. 10 and 13. Thus, we observe small discontinuities in Figs. 10 and 13 approximately midway (on linear coordinates) between rotational harmonics that are integral multiples of $N^{(\cdot)}$ – as expected from the discussion of Eq. (109). These discontinuities would not have been present if Eq. (110) had been used to evaluate $\hat{\phi}_{00}(n/N^{(\cdot)}\Delta)$.

As n tends to zero, Figs. 10 and 13 show that $|\hat{\phi}_{00}(n/N^{(\cdot)}\Delta)|$ tends to unity as required by Eq. (78). In addition, we see by comparing Figs. 9 and 12 with Figs. 10 and 13 respectively, that $\hat{\phi}_{00}(n/N^{(\cdot)}\Delta)$ is zero at the positions of the tooth-meshing harmonic numbers, which occur at rotational harmonic numbers that are integral multiples of $N^{(\cdot)}$ – i.e., $(n/N^{(\cdot)}\Delta) = p/\Delta$ where $p = \pm 1, \pm 2, \cdots$.

Examination of Figs. 10 and 13 shows that for large n, the envelope of the maxima of $|\hat{\phi}_{00}(n/N^{(\cdot)}\Delta)|$ decays linearly with increasing n. The maxima are controlled by the first term in the right-hand side of Eq. (109):

$$J_0\left(\frac{n}{N^{(\cdot)}}\,\frac{\pi L}{\Delta}\right) = \frac{\sin[(n/N^{(\cdot)})\pi L/\Delta]}{(n/N^{(\cdot)})\pi L/\Delta} \quad . \tag{126}$$

Hence, for large $n/N^{(\cdot)}$, the envelope of the maxima of $|\hat{\phi}_{00}(n/N^{(\cdot)}\Delta)|$ has a slope of -1 on logarithmic coordinates, which is equivalent to -6.02 dB per octave. In fact, the envelope of the maxima of $|\hat{\phi}_{00}(n/N^{(\cdot)}\Delta)|$ is very similar to the behavior of a first-order system – e.g., see pp. 12-17 of Ref. 19 – which can be approximated by two straight lines on logarithmic

coordinates. This approximation of the envelope of the maxima of $|\hat{\phi}_{00}(n/N^{(\cdot)}\Delta)|$ *in the case of spur gears* is

$$|\hat{\phi}_{00}(n/N^{(\cdot)}\Delta)|_{env} \approx \begin{cases} 1 & , (n/N^{(\cdot)}) < (\pi L/\Delta)^{-1} \\ [(\pi L/\Delta)n/N^{(\cdot)}]^{-1}, & (n/N^{(\cdot)}) > (\pi L/\Delta)^{-1} \end{cases} , \quad (127)$$

where we see that $(n/N^{(\cdot)}) = (\pi L/\Delta)^{-1}$ locates the breakpoint.

Mesh-attenuated tooth-spacing error spectra

When the tooth-spacing error spectrum $G_{00}^{(\cdot)}(n)$ of Eq. (120) is multiplied by the squared mesh transfer function $|\hat{\phi}_{00}(n/N^{(\cdot)}\Delta)|^2$, we obtain the one-sided mesh-attenuated tooth-spacing error spectrum $2|\alpha_{rn}^{(\cdot)}|_{00}^2$ – according to Eqs. (87) and (120). The *envelopes* of the square roots of these one-sided line spectra are plotted in Figs. 11 and 14 for gears (1) and (2) respectively. A line occurs at each discontinuity in slope in the two figures. Figures 11 and 14 are, respectively, the products of the functions plotted in Figs. 9 and 10 and Figs. 12 and 13. The same logarithmic scales are used in all of these plots.

Since the mesh transfer functions in Figs. 10 and 13 are essentially unity at the positions of the fundamental rotational harmonic, the fundamental rotational harmonics in Figs. 9 and 11 have the same value as do those in Figs. 12 and 14. Thus, the meshing action of the gears provides no attenuation of the fundamental rotational harmonic of tooth-spacing errors. However, the higher-order harmonics receive considerable attenuation – as may be seen by comparing Figs. 9 and 11 or Figs. 12 and 14. The asymptotic slopes of the envelopes of the maxima in Figs. 11 and 14 is -1, which corresponds to -6.02 dB per octave – as was the case for the mesh transfer functions.

It is particularly interesting to compare the strengths of the sidebands nearest to the tooth-meshing harmonics in Figs. 9 and 12 with the same mesh-attenuated sidebands appearing in Figs. 11 and 14. These mesh-attenuated sidebands are strongly attenuated in comparison with their neighboring harmonics, which

show much less attenuation. This strong attenuation occurs because the sidebands closest to the tooth-meshing harmonics partially fall into the nulls of the mesh transfer functions that occur at the tooth-meshing harmonics, as shown in Figs. 10 and 13.

Tooth-Meshing Harmonic Contributions and Effects of Different Axial Contact Ratios

Figures 15 to 17 illustrate contributions to the tooth-meshing harmonics of the static transmission error and Figs. 18 to 20 illustrate effects of different axial contact ratios for the case of tooth-spacing errors on helical gears.

Load-dependent component

In the case of spur gears with constant tooth-pair stiffnesses per unit length of line of contact, Eq. (98b) gives the Fourier-series coefficients of the tooth deformation component of the static transmission error for a *pair* of meshing gears. Figure 15 shows the normalized values of the corresponding rms amplitudes of these tooth deformation harmonics:

$$\sqrt{2}\left|\frac{\alpha_{Wn}}{W_0/\bar{K}_T}\right| = \sqrt{2}\left|\frac{\sin(n\pi L/\Delta)}{n\pi L/\Delta}\right| \quad . \tag{128}$$

Comparing the positions of the harmonics in Fig. 15 with Figs. 11 and 14, we see that the tooth-meshing harmonics of Fig. 15 occur at the positions of the nulls shown in Figs. 11 and 14, as noted earlier. Since the magnitudes of the harmonics shown in Fig. 15 are normalized by the mean deformation $W_0/\bar{K}_T$, no direct comparisons should be made between the heights of the lines in Fig. 15 and the envelopes shown in Figs. 11 and 14.

Mean deviation components

Equation (50) is our general expression for the Fourier-series coefficients of the mean deviation component of the transmission error from gear (•). In the present case, where we have assumed the tooth-pair stiffness to be constant, the expansion coefficients $a_{0\ell}^{(\bullet)}$ for use in Eq. (50) are given by Eq. (102), where $\bar{m}_C^{(\bullet)}(z)$ is the axial average of the mean deviation $m_C^{(\bullet)}(y,z)$ of the tooth-faces of gear (•) from perfect involute surfaces — as may be seen from Eq. (100).

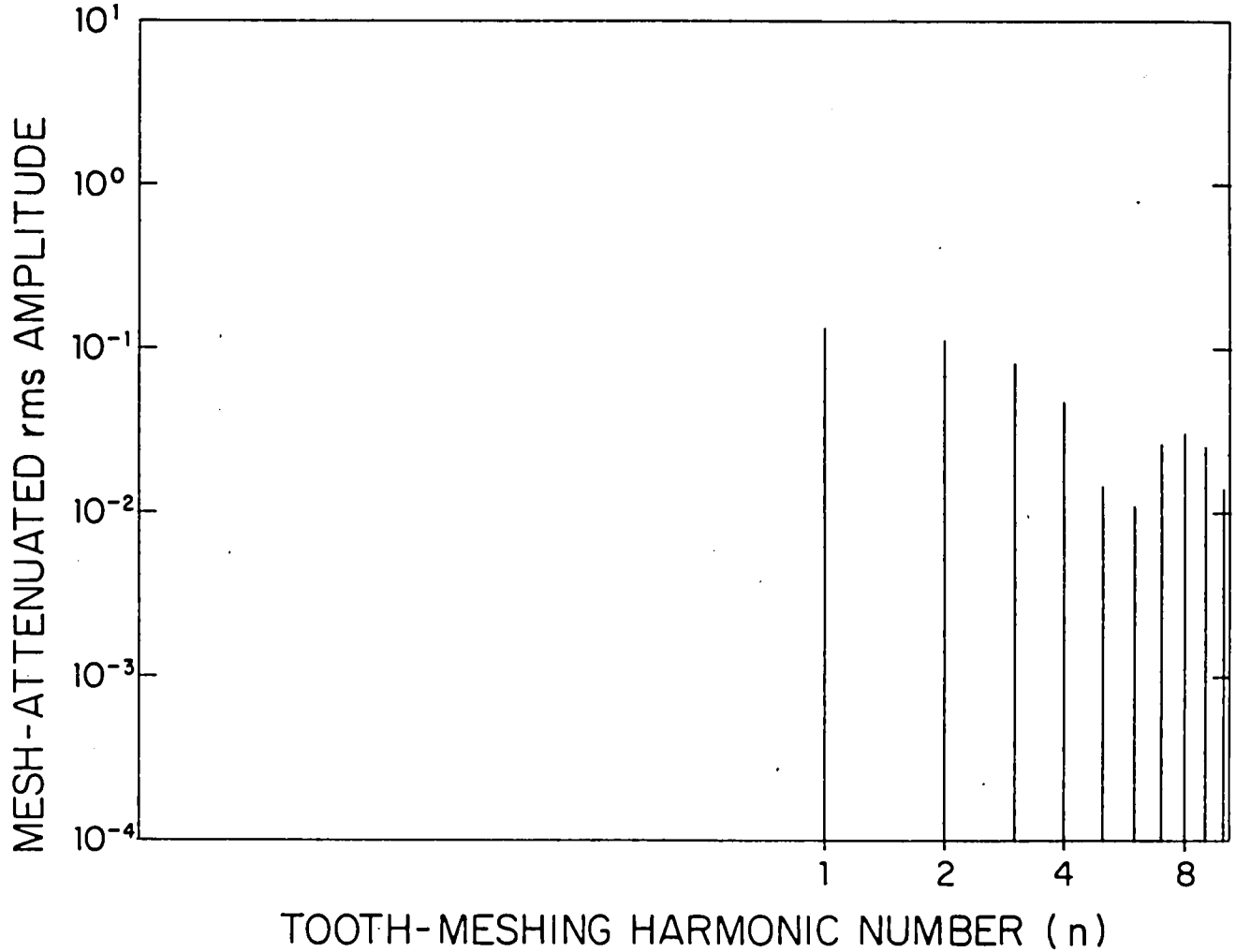

FIGURE 15. MESH-ATTENUATED TOOTH-PAIR DEFORMATION NORMALIZED rms HARMONIC AMPLITUDES.

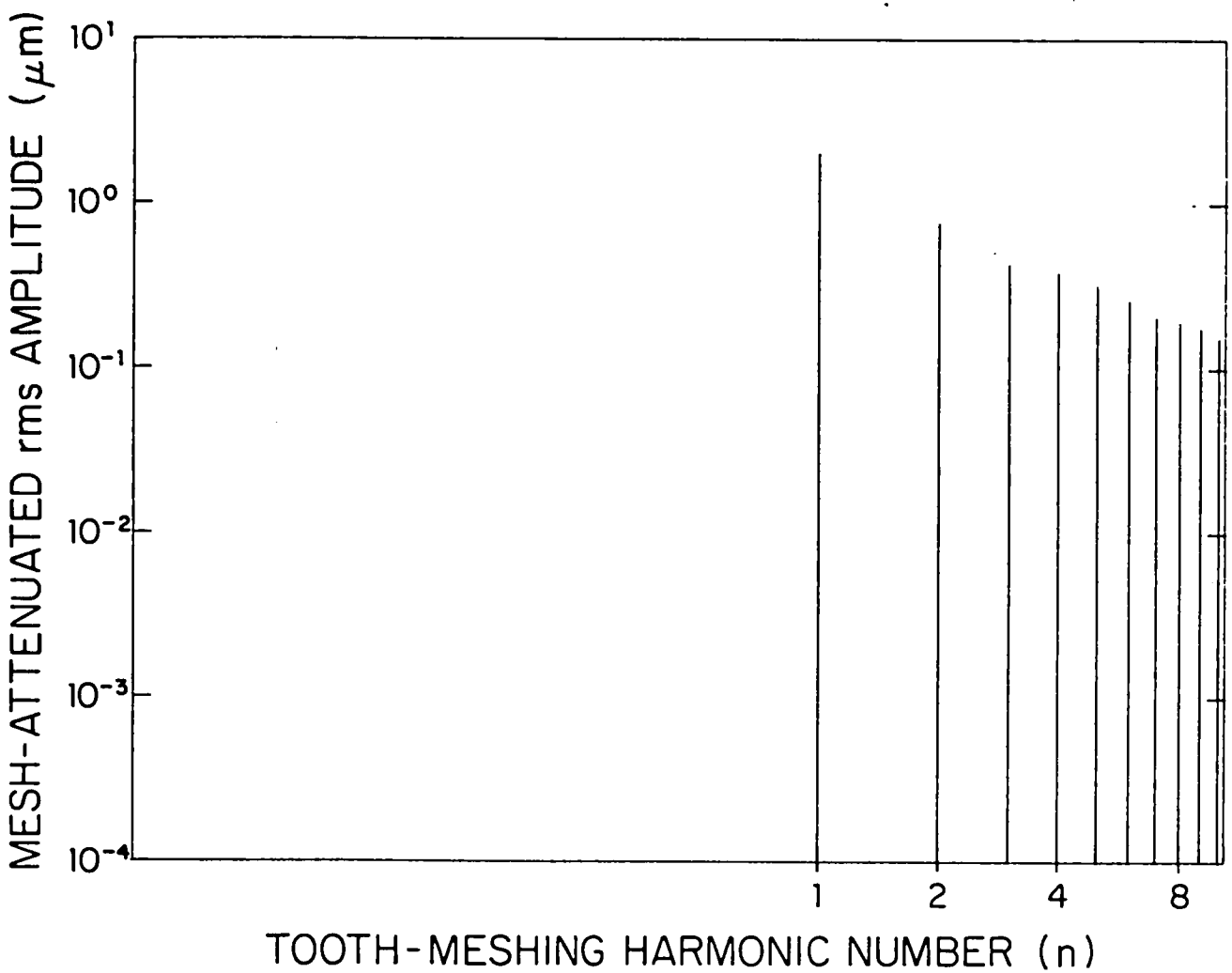

FIGURE 16. MESH ATTENUATED MEAN PROFILE DEVIATION rms HARMONIC AMPLITUDES OF GEAR (1).

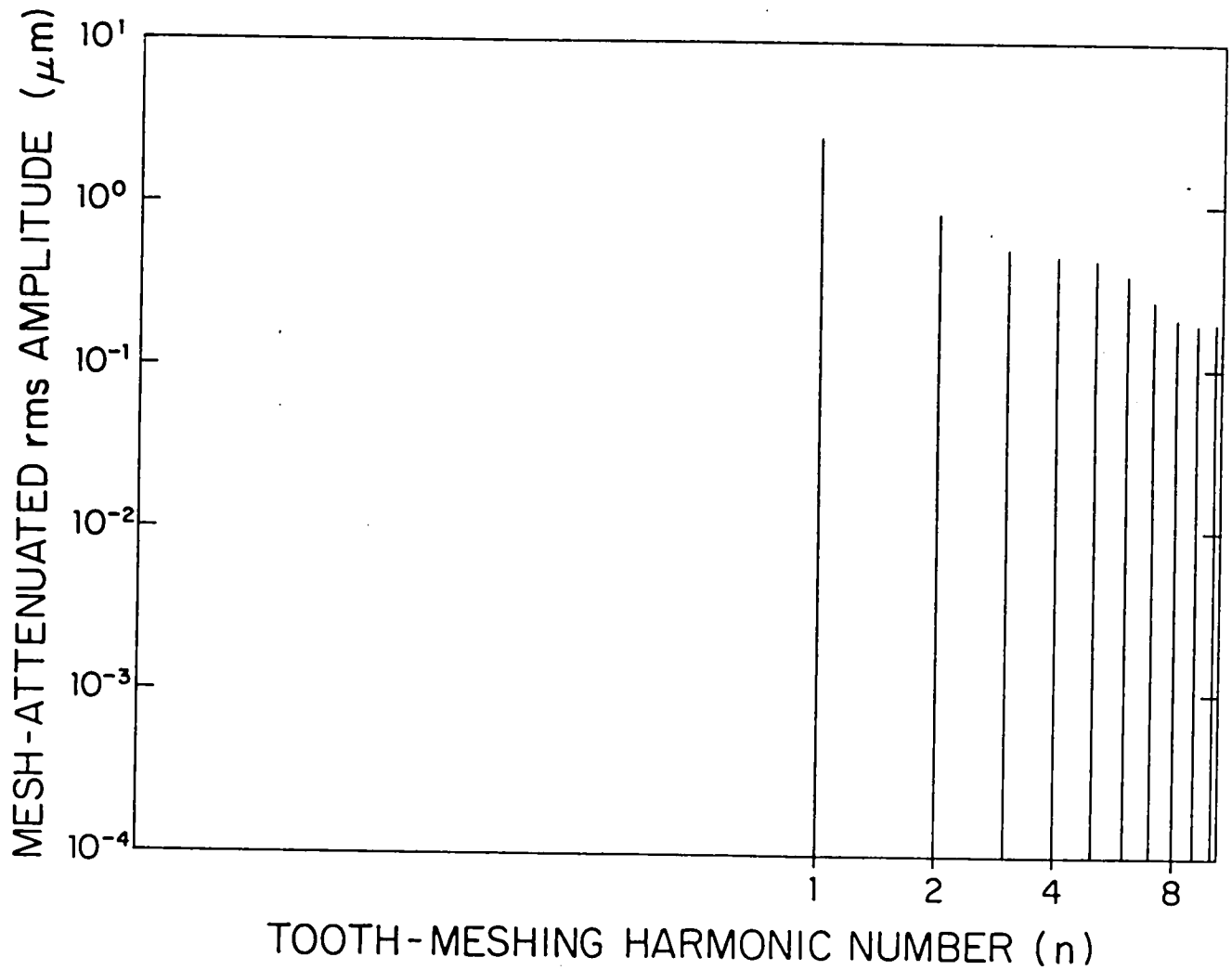

FIGURE 17. MESH-ATTENUATED MEAN PROFILE DEVIATION rms HARMONIC AMPLITUDES OF GEAR (2).

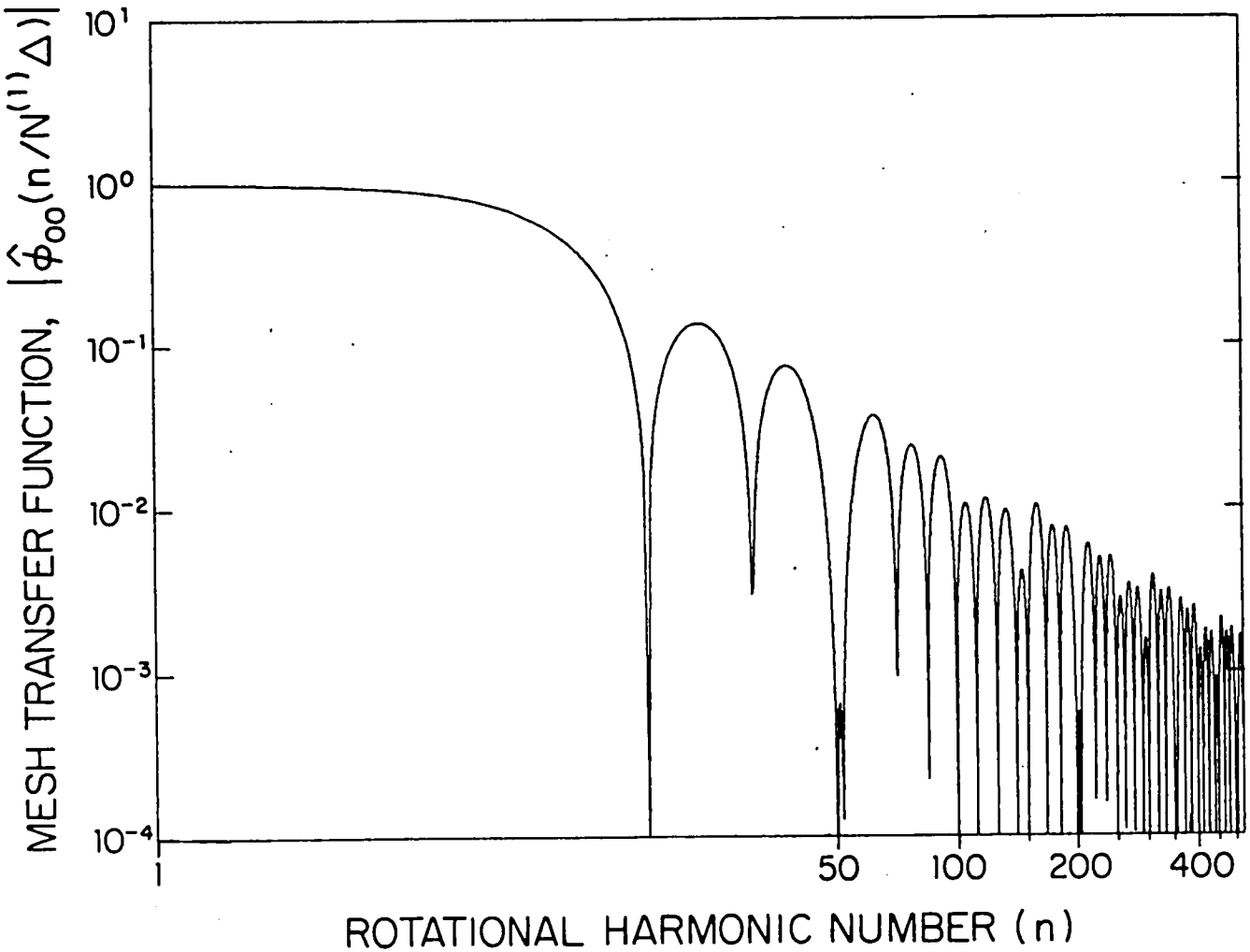

FIGURE 18. TOOTH-SPACING ERROR MESH TRANSFER FUNCTION OF HELICAL GEAR WITH $(L/\Delta) = 1.819$ AND $(FL/A\Delta) = 1.1$.

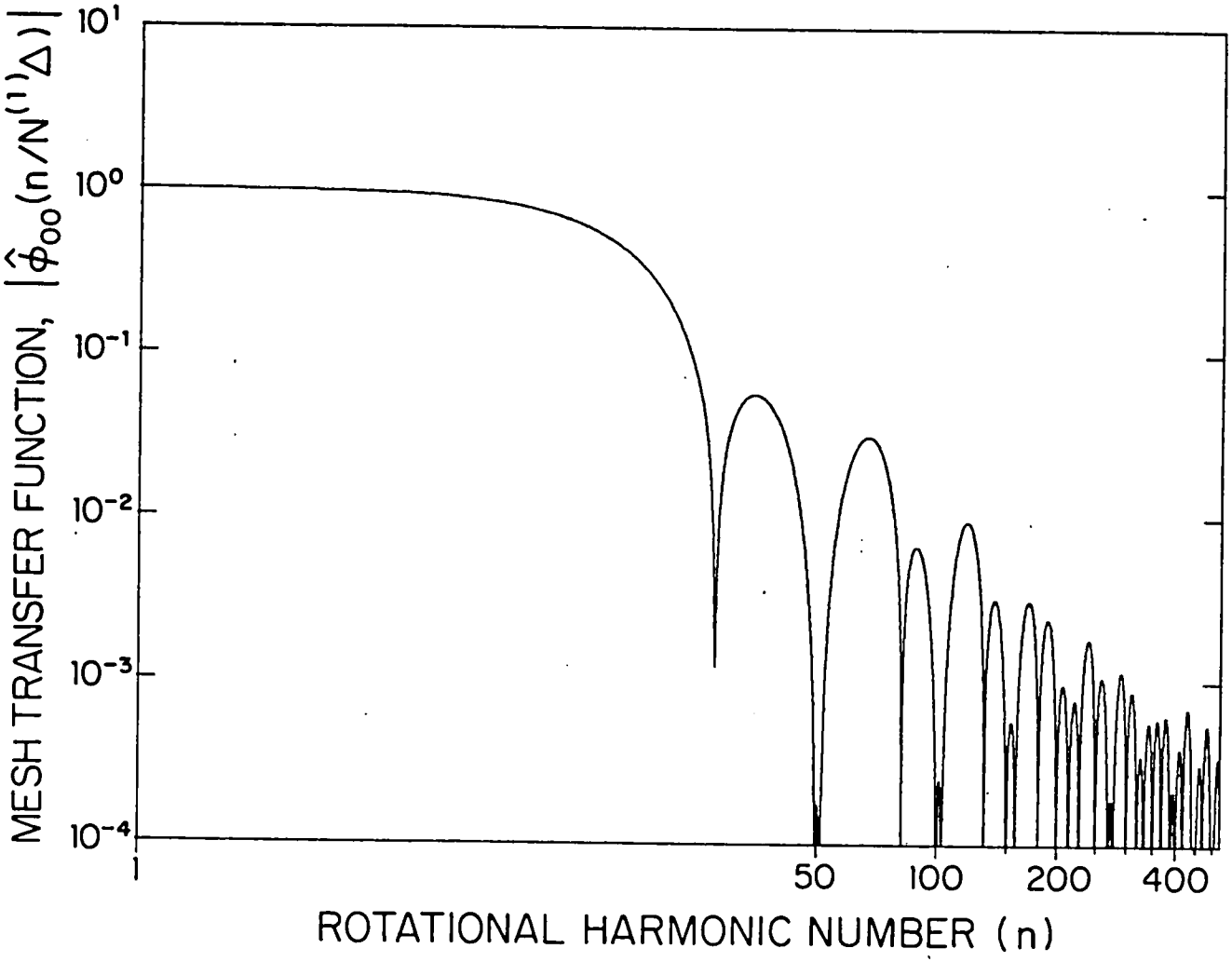

FIGURE 19. TOOTH-SPACING ERROR MESH TRANSFER FUNCTION OF HELICAL GEAR WITH $(L/\Delta) = 1.819$ AND $(FL/A\Delta) = 3.19$.

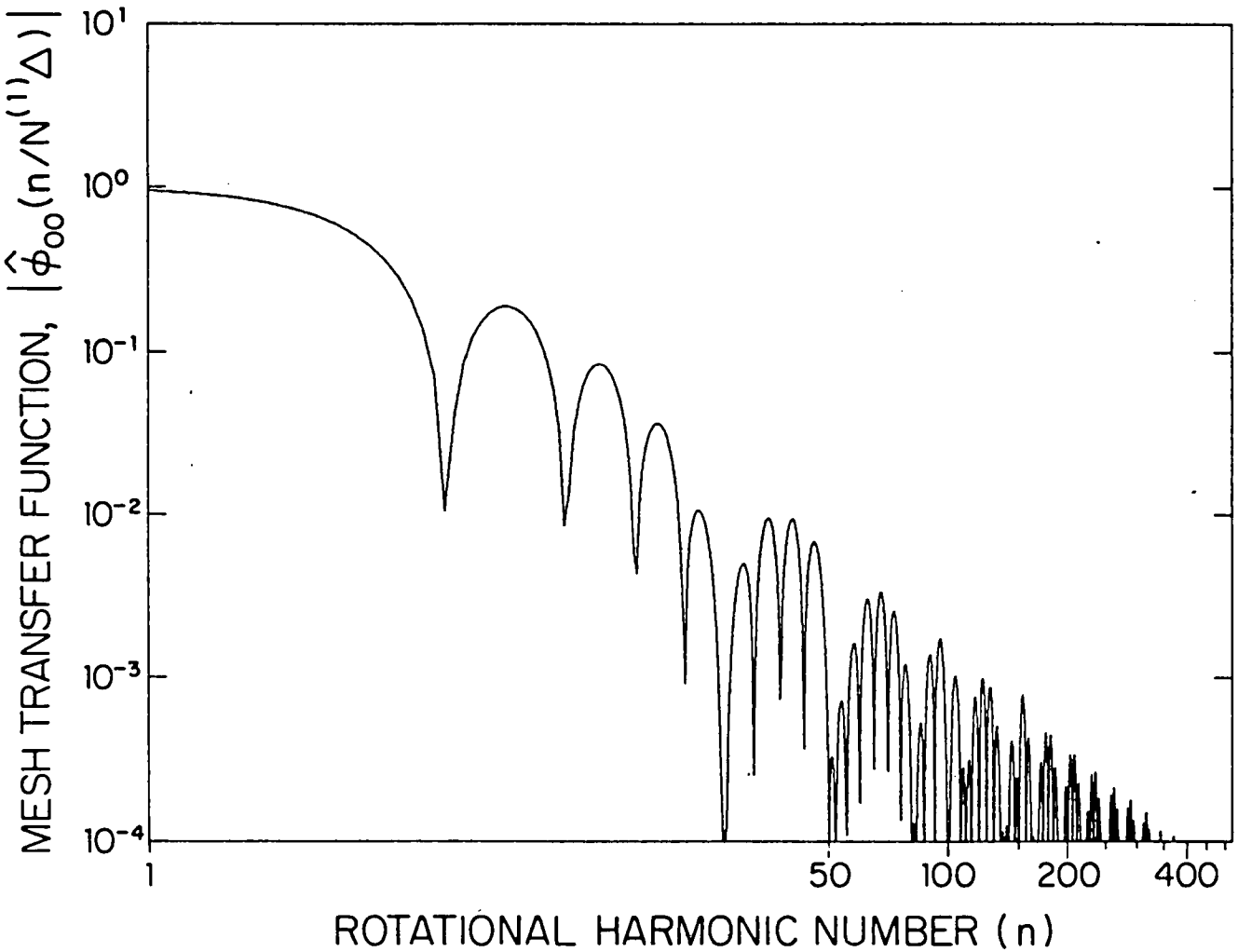

FIGURE 20. TOOTH-SPACING ERROR MESH TRANSFER FUNCTION OF HELICAL GEAR WITH $(L/\Delta) = 1.819$ AND $(FL/A\Delta) = 9.251$.

Four measurements of the deviations of the tooth profiles of the 50 tooth gear from perfect involute profiles are shown in Fig. 21. The four teeth measured were picked at approximately 90° intervals around the gear. The tips of the teeth are to the right and the roots are to the left. Distances along the abscissa in Fig. 21 are measured in the same units as the coordinate s in Ref. 1. Thus, the region of tooth contact along the abscissa in Fig. 21 is of length equal to the path of contact length given by Eq. (111) – as indicated in Fig. 21. Notice that one-half of the value cited earlier for tip rounding is accounted for in determining the region of contact in Fig. 21. The other one-half is accounted for in determining the region of contact on the teeth of the mating gear.

The variable of integration z in Eq. (102) is related to coordinate s by Eqs. (16) and (17) of Ref. 1, where $\gamma \equiv 0$ for spur gears since $\psi = 0$ in this case – see Eq. (18) of Ref. 1. Thus, for spur gears, we have $z = s \sin\phi$; hence, $D = L\sin\phi$, as may be seen from Eq. (C8) of Ref. 1 where D is the active tooth depth illustrated in Fig. 4 of Ref. 1: D = 0.004665 m (0.1837 in.). The abscissa in Fig. 21 therefore is proportional to the variable of integration z with origin centered in the region of contact, which is of width D when measured in units of z.

Values of the ordinates in Fig. 21 are *deviations* of the tooth profiles from perfect involute curves as defined in Fig. 3 of Ref. 1 and the accompanying discussion. Since these deviations are defined as positive when they are "equivalent" to *removal* of material from perfect involute tooth faces, the positive direction of the ordinate in Fig. 21 is downward. The location of the origin of the ordinate in Fig. 21 is irrelevant since the origin has an effect only on the zeroth order expansion coefficients $a_{00}^{(\cdot)}$ determined by Eq. (102), and we have seen that the corresponding expansion function $\hat{\phi}_{00}(n/\Delta)$ in Eq. (50) is zero except for n = 0 – see Eq. (78).

If we interpret each of the four profile deviation measurements in Fig. 21 as a measurement of the axial average of the tooth-face deviation, then the average value of these four curves (after removal of vertical separations) becomes our best estimate of the mean profile deviation $\bar{m}_C^{(1)}(z)$ for the 50-tooth gear. However, all four curves shown in Fig. 21 are virtually identical except for their vertical translations; hence, we computed the expansion coefficients $a_{0\ell}^{(1)}$ given by Eq. (102) from

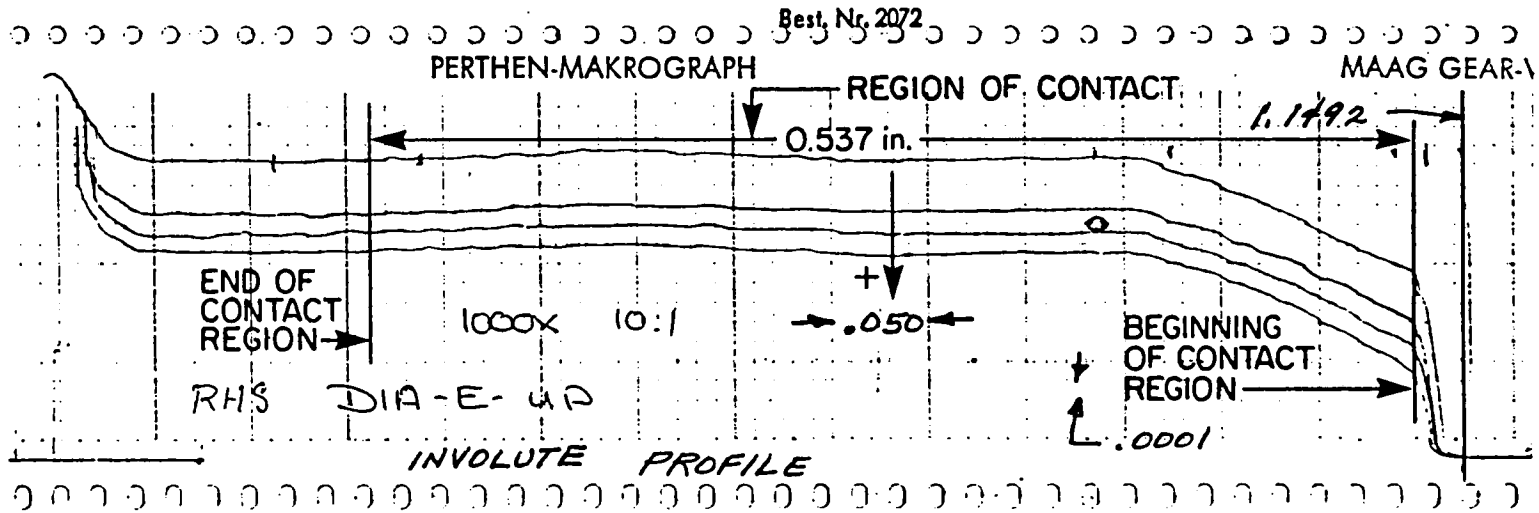

FIGURE 21. MEASURED DEVIATIONS FROM INVOLUTE PROFILES OF 4 TEETH SPACED APPROXIMATELY 90° APART ON GEAR (1).

only one curve – the second curve from the top shown in Fig. 21. This computation was begun by first reading 54 equi-spaced points off the second curve. To accommodate the fluctuations of the $P_\ell(2z/D)$ in Eq. (102), we then used linear interpolation to obtain five additional points on the second curve between each of the original 54. The integrals in Eq. (102) were then evaluated using the trapezoidal rule operating on the integrand evaluated at the resulting 319 points. Expansion coefficients $a_{0\ell}^{(1)}$ were computed through $\ell = 20$ in this manner. As a check, the profile was then reconstructed from these expansion coefficients using Eq. (101) – a fit to the original profile with negligible error was obtained. The expansion coefficients through $\ell = 20$ were then used together with Eq. (99a) to calculate the Fourier-series coefficients $\alpha_{mn}^{(1)}$ using Eq. (50). The corresponding rms amplitudes, which are $\sqrt{2}|\alpha_{mn}^{(1)}|$, are plotted in Fig. 16.

The same procedure was used with the mating gear (2), which has 53 teeth. The only difference in the procedure for this gear was our reversal of the direction of the z-axis – i.e., the tooth tips were on the negative side of the origin of the abscissa – because the tips of gear (2) mesh with the roots of gear (1). The rms amplitudes, which are $\sqrt{2}|\alpha_{mn}^{(2)}|$ for gear (2), are shown in Fig. 17. The harmonics shown in Figs. 15, 16, and 17 all occur at the same positions, which are positions of nulls in Figs. 11 and 14.

The total contribution of the mean profile deviation components from gears (1) and (2) would be obtained by adding the complex Fourier-series coefficients $\alpha_{mn}^{(1)}$ and $\alpha_{mn}^{(2)}$ from gears (1) and (2). Finally, the Fourier-series coefficients of all components of the tooth-meshing harmonics would be obtained by adding to the coefficients of the mean profile deviation components the complex Fourier-series coefficients of the load-dependent component as indicated by Eq. (57) or Eq. (65) of Ref. 1.

Mesh transfer functions for tooth-spacing errors on helical gears

So far, we have illustrated our results for spur gears only. Let us now compare some of these results with results that would be predicted for helical gears. We recall that the tooth-spacing error spectra shown in Figs. 5, 8, 9, and 12 are independent of all gear *design* parameters except number of teeth. Hence, these spectra could just as easily have been computed from measurements

made on helical gears. It follows that we can estimate differences in the *mesh-attenuated* tooth-spacing error spectra that would be observed in comparing spur and helical gears — and differences that would be observed in comparing helical gears with different axial contact ratios — by comparing differences in the mesh transfer functions for tooth-spacing errors between spur and helical gears, and among helical gears with different axial contact ratios.

Figures 18 to 20 show the magnitude of the tooth-spacing error mesh transfer functions $|\hat{\phi}_{00}(n/N^{(1)}\Delta)|$ for 50-tooth helical gears with three different values (1.1, 3.19, and 9.251) of the axial contact ratio $FL/A\Delta$. Each of Figs. 18, 19, and 20 was computed by Eq. (88) using $k = 0$, $\ell = 0$ and the same value of transverse contact ratio, $(L/\Delta) = 1.819$, that was used to compute the spur gear mesh transfer functions shown in Figs. 10 and 13. Furthermore, the logarithmic scales on the ordinates and abscissas of Figs. 18 to 20 are identical with those used in Fig. 10. Thus, Figs. 10, 18, 19, and 20 provide a direct illustration of the very substantial decrease in the tooth-spacing error vibratory excitation that is provided by helical gears in comparison with spur gears. The *attenuation* of the excitation is increased with increasing axial contact ratio, and the resulting improvements increase with increasing harmonic number. Notice the very substantial increase in attenuation in the higher harmonics predicted for the helical gear with the relatively small axial contact ratio of $(FL/A\Delta) = 1.1$ shown in Fig. 18 in comparison with the spur gear result shown in Fig. 10. Finally, we see that the mesh transfer functions shown in Figs. 18 to 20 all have nulls at the tooth meshing harmonics of $(n/N^{(1)}\Delta) = p/\Delta$ for $p = \pm 1, \pm 2, \cdots$. The tickmarks on the abscissas in the figures show the locations of the first ten tooth-meshing harmonics.

We may approximate the behavior of the envelopes of the maxima in Figs. 18 to 20 from the first term in Eq. (88) for $k = 0$, $\ell = 0$:

$$J_0\left(\frac{n}{N^{(\cdot)}}\frac{\pi FL}{A\Delta}\right)J_0\left(\frac{n}{N^{(\cdot)}}\frac{\pi L}{\Delta}\right) = \frac{\sin[(n/N^{(\cdot)})\pi FL/A\Delta]}{(n/N^{(\cdot)})\pi FL/A\Delta}\,\frac{\sin[(n/N^{(\cdot)})\pi L/\Delta]}{(n/N^{(\cdot)})\pi L/\Delta}\,. \tag{129}$$

Hence, for large $n/N^{(\cdot)}$, the envelope of the maxima of $|\hat{\phi}_{00}(n/N^{(\cdot)}\Delta)|$ has a slope of -2 on logarithmic coordinates,

which is equivalent to -12.04 dB per octave. This behavior is typical of second-order systems – e.g., see pp. 24-29 of Ref. 19 – and can be approximated by two straight lines on logarithmic coordinates. The resulting approximation of the envelope of the maxima of $|\hat{\phi}_{00}(n/N^{(\cdot)}\Delta)|$ *in the case of helical gears* is

$$|\hat{\phi}_{00}(n/N^{(\cdot)}\Delta)|_{env} \approx \begin{cases} 1 & , \ \frac{n}{N^{(\cdot)}} < \left(\pi^2 \ \frac{FL}{A\Delta} \ \frac{L}{\Delta}\right)^{-\frac{1}{2}} \\ \left[\pi^2 \ \frac{FL}{A\Delta} \ \frac{L}{\Delta}\left(\frac{n}{N^{(\cdot)}}\right)^2\right]^{-1} & , \ \frac{n}{N^{(\cdot)}} > \left(\pi^2 \ \frac{FL}{A\Delta} \ \frac{L}{\Delta}\right)^{-\frac{1}{2}} \end{cases} , \quad (130)$$

where we see that $(n/N^{(\cdot)}) = [\pi^2(FL/A\Delta)(L/\Delta)]^{-\frac{1}{2}}$ locates the breakpoint.

Mesh Transfer Functions for Higher-Order Error Contributions

Figures 18 to 20 have illustrated the effects of different axial contact ratios of helical gears for one particular error component – the tooth-spacing component $k = 0$, $\ell = 0$. Figures 22 to 27 illustrate the behavior of the magnitudes of the mesh transfer functions of different error components while holding the axial and transverse contact ratios at constant values:

$$\frac{FL}{A\Delta} = 3.19, \qquad \frac{L}{\Delta} = 1.819 \ . \quad (131)$$

The order of the indices k,ℓ in going from Figs. 22 to 27 is that indicated by Fig. 1. The logarithmic scales of the ordinates and abscissas in Figs. 22 to 27 are identical with those used in Figs. 18 to 20.

Equation (88) was used to compute the values of $|\hat{\phi}_{k\ell}(n/N^{(\cdot)}\Delta)|$ shown in Figs. 22 to 27. Thus, Fig. 22 is a repeat of Fig. 19 – and shows the nulls of $\hat{\phi}_{00}(n/N^{(\cdot)}\Delta)$ that occur at the tooth-meshing harmonics as discussed earlier. The other mesh transfer functions shown in Figs. 23 to 27 do not possess these nulls. However, the envelopes of the peaks of all of the mesh transfer functions have the same asymptotic slope (-12.04 dB per octave) in the large harmonic number region. Their behavior differs in the low harmonic number region.

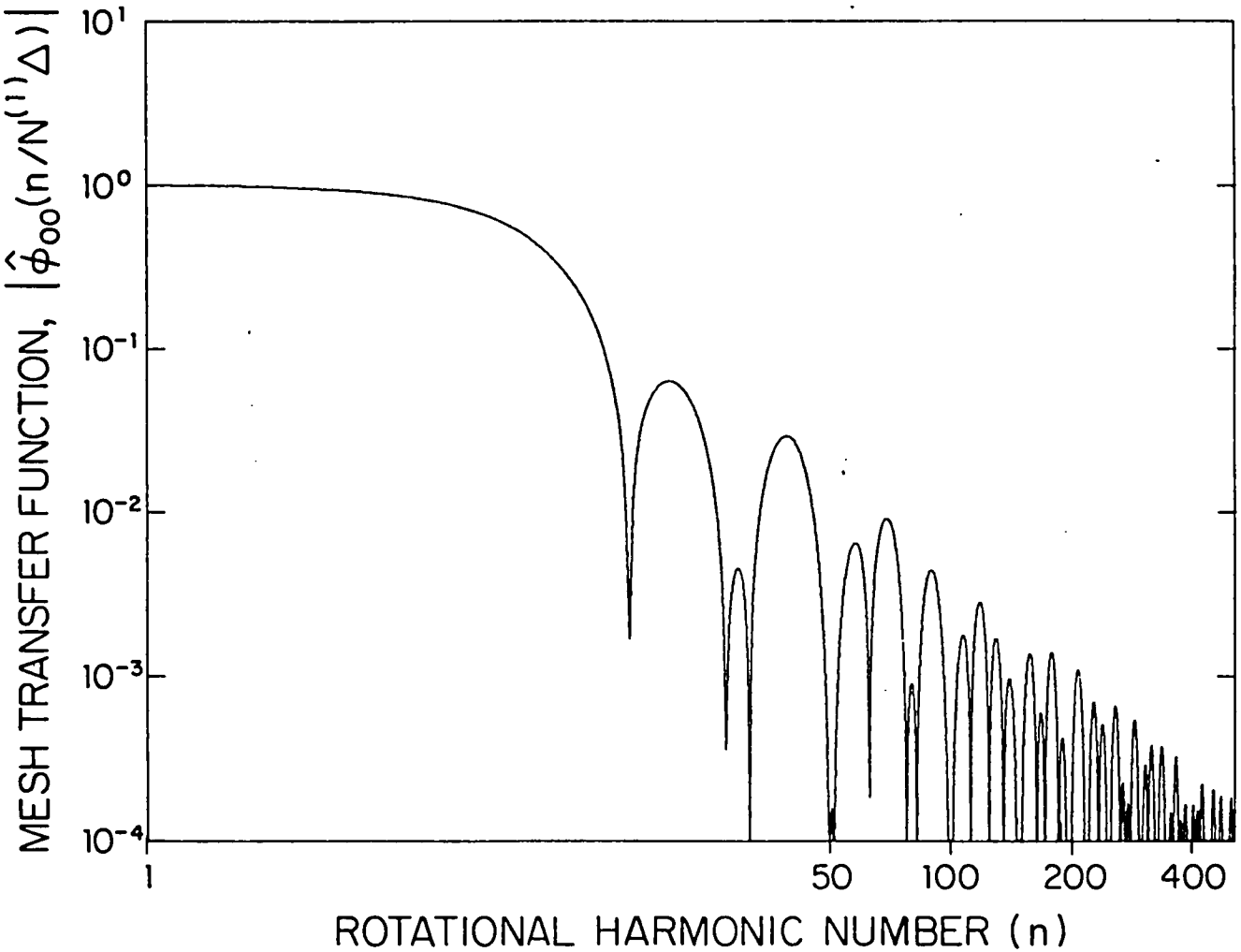

FIGURE 22. TOOTH-SPACING DEVIATION (k=0, ℓ=0) MESH TRANSFER FUNCTION OF HELICAL GEAR WITH (L/Δ) = 1.819 AND (FL/AΔ) = 3.19.

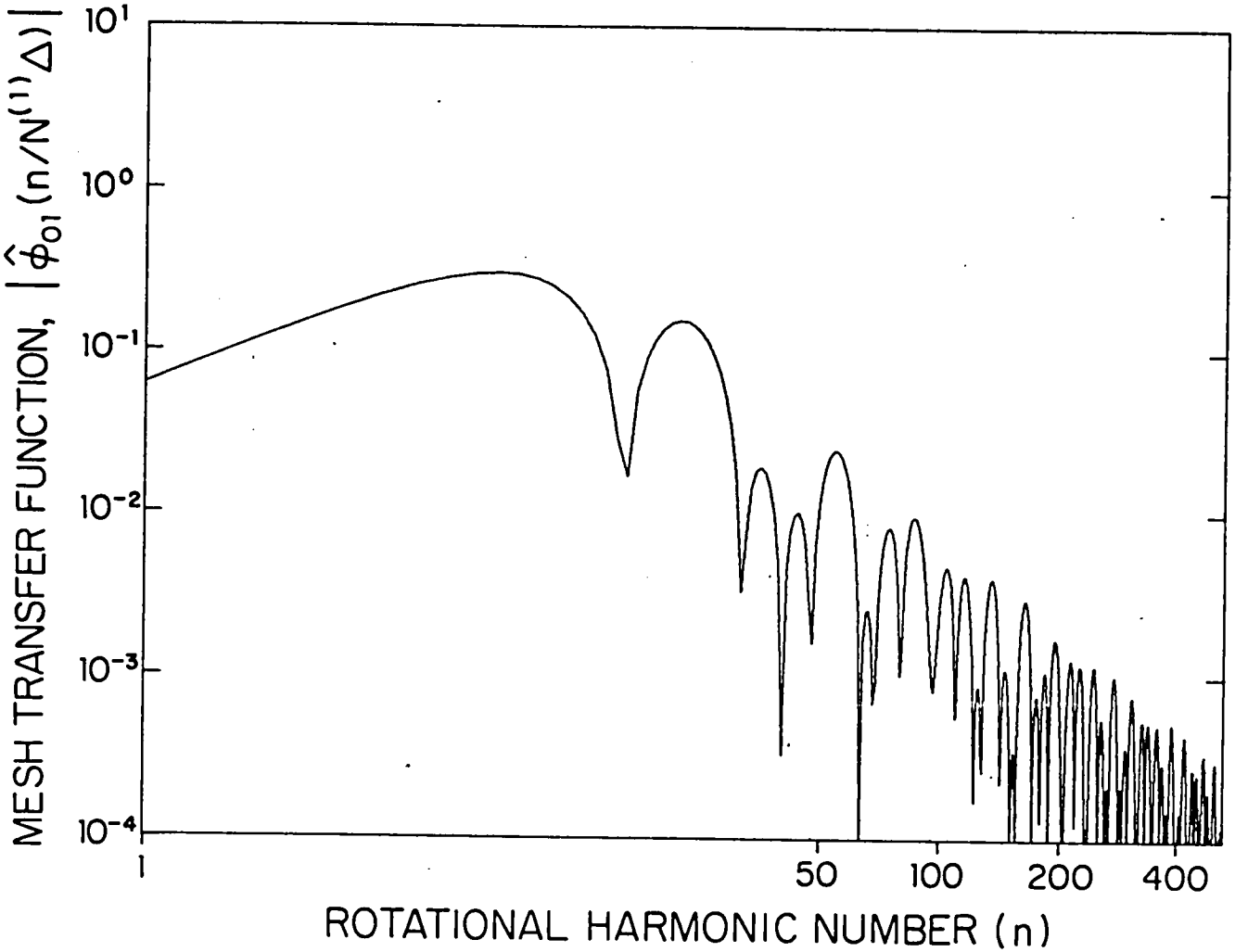

FIGURE 23. INVOLUTE SLOPE DEVIATION (k=0, ℓ=1) MESH TRANSFER FUNCTION OF HELICAL GEAR WITH (L/Δ) = 1.819 AND (FL/AΔ) = 3.19.

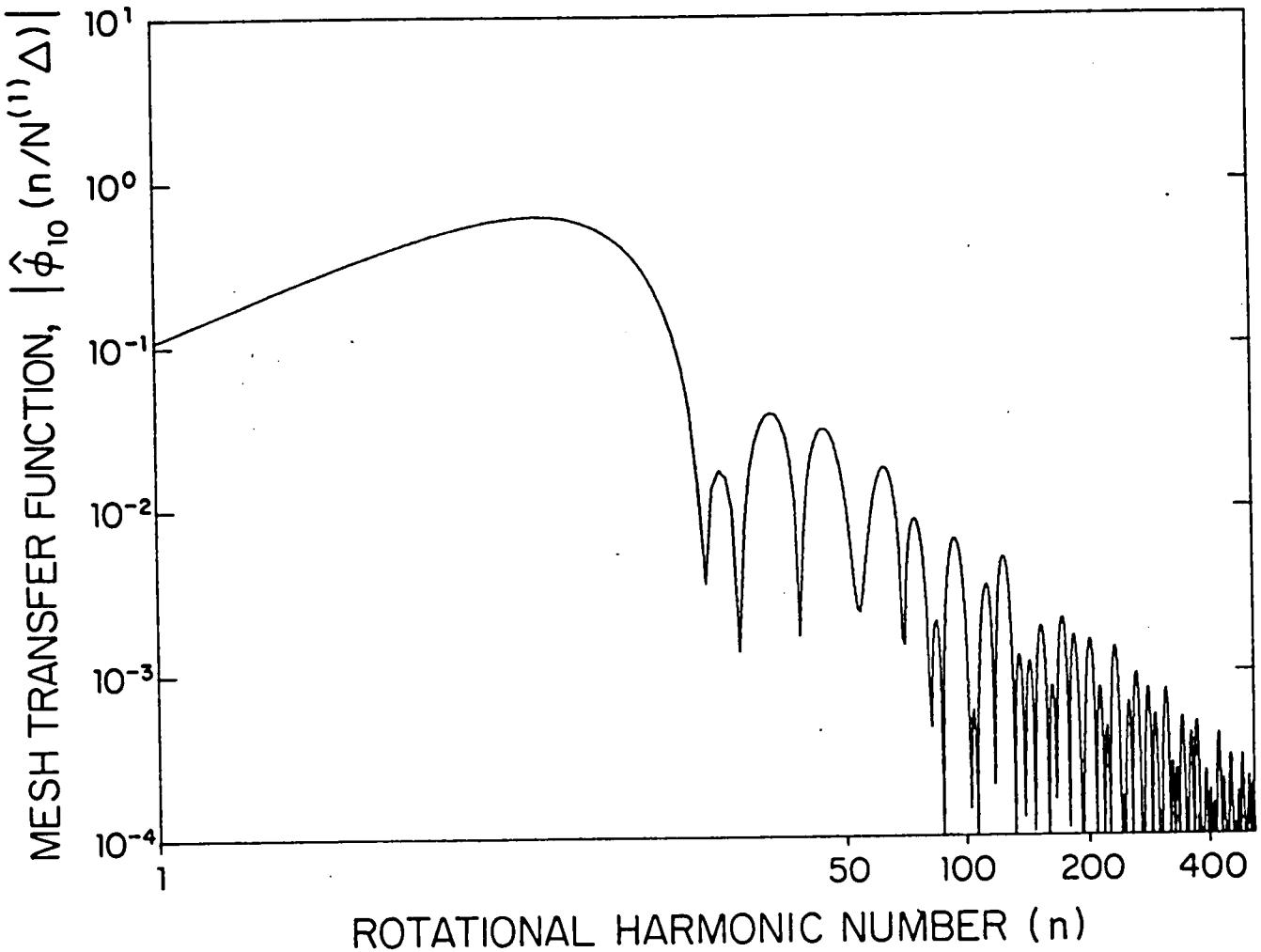

FIGURE 24. LEAD MISMATCH DEVIATION (k=1, ℓ=0) MESH TRANSFER FUNCTION OF HELICAL GEAR WITH $(L/\Delta) = 1.819$ AND $(FL/A\Delta) = 3.19$.

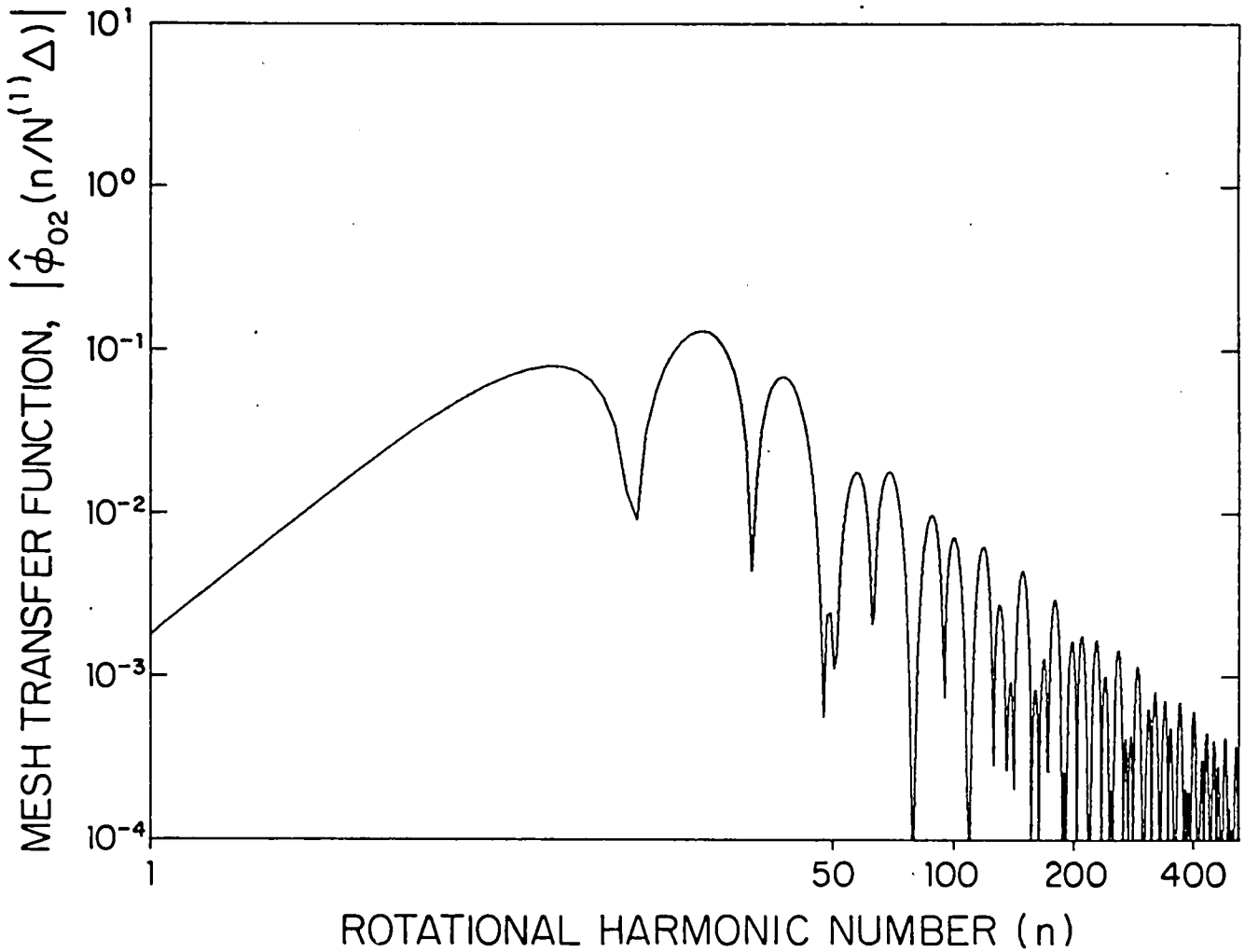

FIGURE 25. INVOLUTE HOLLOW (FULLNESS) DEVIATION (k=0, ℓ=2) MESH TRANSFER FUNCTION OF HELICAL GEAR WITH (L/Δ) = 1.819 AND (FL/AΔ) = 3.19.

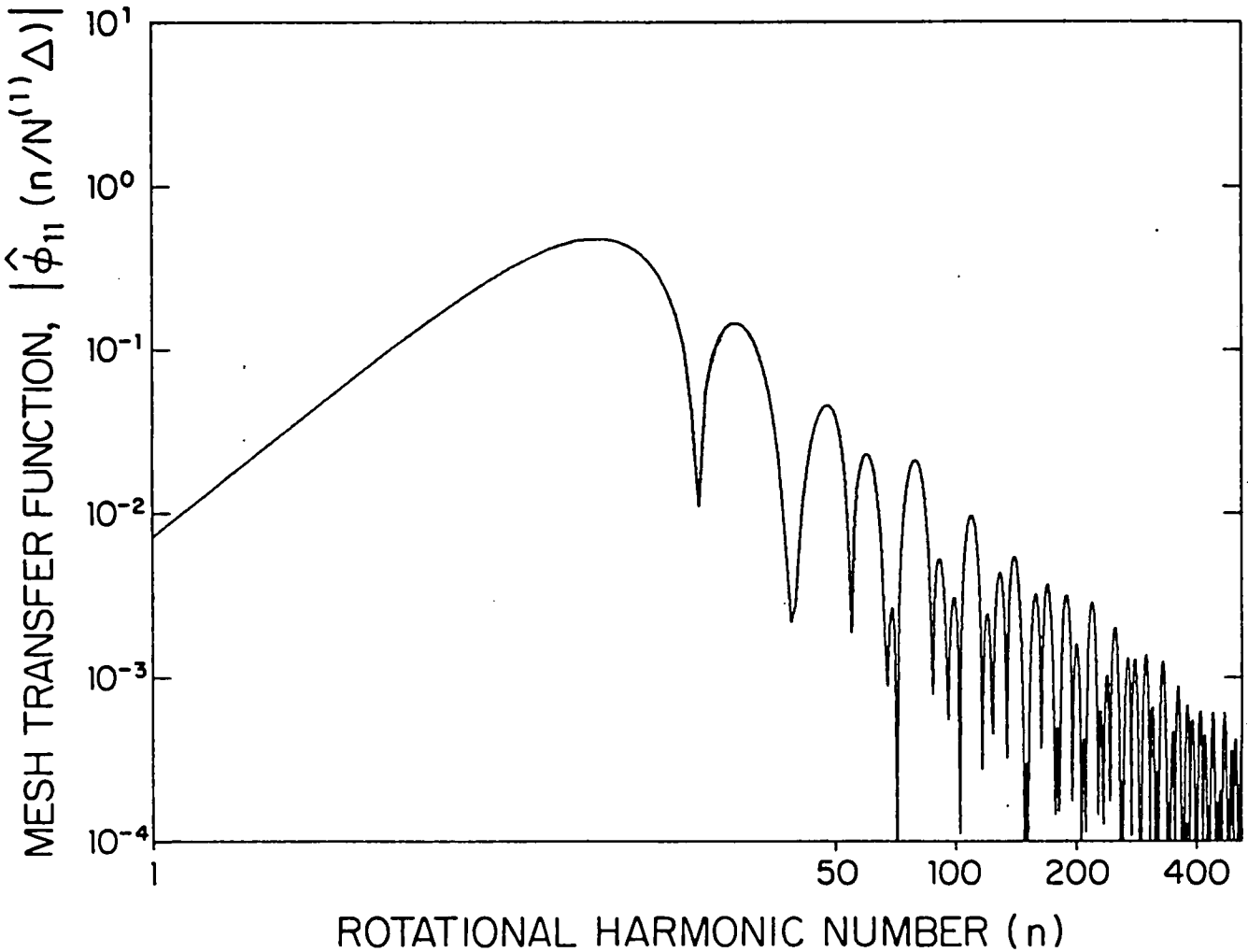

FIGURE 26. COMBINED LEAD MISMATCH-INVOLUTE SLOPE DEVIATION (k=1, ℓ=1) MESH TRANSFER FUNCTION OF HELICAL GEAR WITH (L/Δ) = 1.819 AND (FL/AΔ) = 3.19.

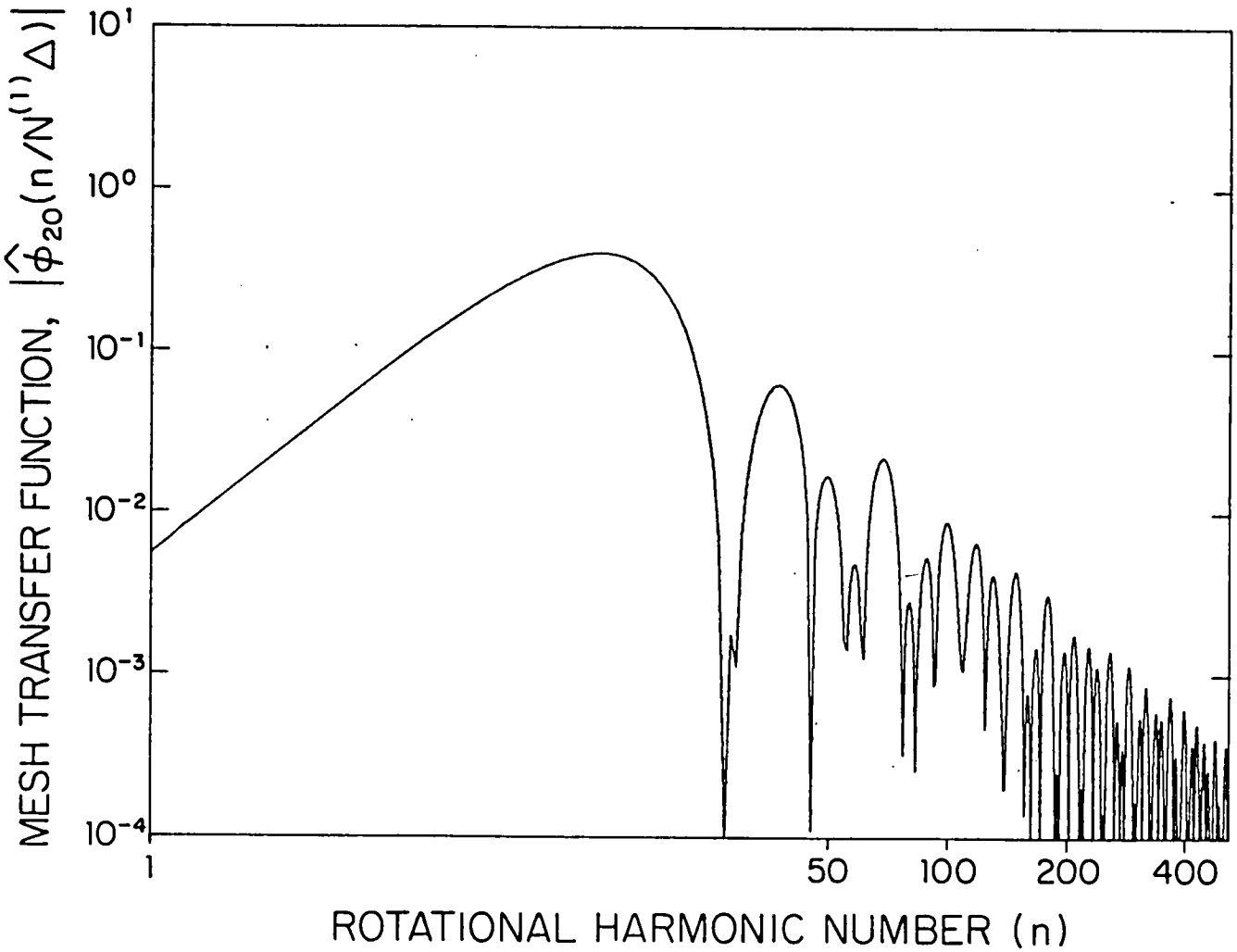

FIGURE 27. LEAD HOLLOW (CROWNING) DEVIATION (k=2, ℓ=0) MESH TRANSFER FUNCTION OF HELICAL GEAR WITH (L/Δ) = 1.819 AND (FL/AΔ) = 3.19.

Envelopes of mesh transfer functions for helical gears

We may quantify the envelope behavior of the maxima in Figs. 22 to 27 using the magnitude of the first term in Eq. (88):

$$[(2k+1)(2\ell+1)]^{\frac{1}{2}} \left| j_k\left(\frac{n}{N^{(\cdot)}}\,\frac{\pi FL}{A\Delta}\right) j_\ell\left(\frac{n}{N^{(\cdot)}}\,\frac{\pi L}{\Delta}\right)\right| .$$

From Eq. (36) and the above expression, we see that the envelope of the maxima in Figs. 22 to 27 must asymptotically approach *for large* $n/N^{(\cdot)}$ the form

$$\left|\hat{\phi}_{k\ell}(n/N^{(\cdot)}\Delta)\right|_{env} \sim \frac{[(2k+1)(2\ell+1)]^{\frac{1}{2}}}{\pi^2(FL/A\Delta)(L/\Delta)}\left(\frac{n}{N^{(\cdot)}}\right)^{-2} , \qquad (132)$$

which is independent of k and ℓ except for the term in the numerator. For small x, the first term in the Maclaurin series expansion of $j_m(x)$ gives — see, e.g., p. 437 of Ref. 4 —

$$j_m(x) = \frac{x^m}{1\cdot 3\cdot 5\cdots(2m+1)} + O(x^{m+2}) , \qquad (133)$$

which we may use to evaluate the magnitude of the first term in Eq. (88) to yield the behavior of $\left|\hat{\phi}_{k\ell}(n/N^{(\cdot)}\Delta)\right|_{env}$ *for small* $n/N^{(\cdot)}$:

$$\left|\hat{\phi}_{k\ell}(n/N^{(\cdot)}\Delta)\right|_{env} \sim \frac{\pi^{k+\ell}[(2k+1)(2\ell+1)]^{\frac{1}{2}}}{[1\cdot 3\cdot 5\cdots(2k+1)][1\cdot 3\cdot 5\cdots(2\ell+1)]}\left(\frac{FL}{A\Delta}\right)^k\left(\frac{L}{\Delta}\right)^\ell\left(\frac{n}{N^{(\cdot)}}\right)^{k+\ell} . \qquad (134)$$

Hence, for small $n/N^{(\cdot)}$, $\left|\hat{\phi}_{k\ell}(n/N^{(\cdot)}\Delta)\right|$ is linear on logarithmic coordinates with slope equal to $k+\ell$. This behavior predicts the zero slope for small $n/N^{(\cdot)}$ observed in Fig. 22; it also predicts that Figs. 23 and 24 should have the same asymptotic slope for small $n/N^{(\cdot)}$, and that Figs. 25, 26, and 27 all should have the same somewhat larger value of slope for small $n/N^{(\cdot)}$ — which is consistent with the behavior shown in the figures.

We see from Figs. 22 to 27 that we can obtain a reasonably good approximation to the envelope of the maxima of $|\hat{\phi}_{k\ell}(n/N^{(\cdot)}\Delta)|$ for all values of $n/N^{(\cdot)}$ by extending the large and small $n/N^{(\cdot)}$ approximations given by Eqs. (132) and (134) respectively, until they meet. The breakpoint $(n/N^{(\cdot)})_{bp}$ is obtained by equating the right-hand sides of Eqs. (132) and (134) and solving for $n/N^{(\cdot)}$:

$$\left(\frac{n}{N^{(\cdot)}}\right)_{bp} = \frac{1}{\pi}\left\{\frac{[1\cdot3\cdot5\cdots(2k+1)][1\cdot3\cdot5\cdots(2\ell+1)]}{(FL/A\Delta)^{1+k}(L/\Delta)^{1+\ell}}\right\}^{\frac{1}{2+k+\ell}} . \quad (135)$$

From Eqs. (75) and (83), we see that the squares of the expansion coefficients $a_{k\ell}^{(\cdot)}$ and $b_{j,k\ell}^{(\cdot)}$ are direct measures of the mean-square contributions of the various terms $k\ell$ in our expansions of the mean and random tooth-face deviations $m_C^{(\cdot)}(y,z)$ and $\varepsilon_{Cj}^{(\cdot)}(y,z)$. Hence, from Eq. (48) and Eqs. (84) to (87), it is apparent that the mesh transfer functions $\hat{\phi}_{k\ell}(\cdot)$ may be compared with one another to determine the relative attenuation provided by the meshing action of a gear pair on the various classes of errors defined by the dual index $k\ell$. In the large harmonic number region, we see from Eq. (132) that – except for tooth-spacing errors in the immediate vicinity of the tooth-meshing harmonics as noted earlier – the only systematic dependence of $|\hat{\phi}_{k\ell}(n/N^{(\cdot)}\Delta)|_{env}$ on k and ℓ is the factor $[(2k+1)(2\ell+1)]^{\frac{1}{2}}$ in the numerator of Eq. (132). Hence, the mesh provides somewhat less attenuation for the higher-order terms $k\ell$ than for the low-order terms. The differences in the low harmonic number region are more striking as k and ℓ are varied. In particular, we see from Eq. (134) that at $(n/N^{(\cdot)}) = 0$, all of the mesh transfer functions are zero except that associated with tooth-spacing errors, $k = 0$, $\ell = 0$.

Envelopes of mesh transfer functions for spur gears

To develop expressions for the envelopes of the mesh transfer functions for spur gears that are comparable to Eqs. (132), (134), and (135) – which apply to helical gears – we require the magnitude of the first term in Eq. (99a) evaluated at $g = n/N^{(\cdot)}\Delta$:

$$(2\ell+1)^{\frac{1}{2}}\left|J_\ell\left(\frac{n}{N^{(\cdot)}}\,\frac{\pi L}{\Delta}\right)\right| \quad .$$

Using Eq. (36), we see from the above expression that the envelope of the maxima of $|\hat{\phi}_{0\ell}(n/N^{(\cdot)}\Delta)|$ must asymptotically approach *for large* $n/N^{(\cdot)}$ the form

$$|\hat{\phi}_{0\ell}(n/N^{(\cdot)}\Delta)|_{env} \sim \frac{(2\ell+1)^{\frac{1}{2}}}{\pi(L/\Delta)}\left(\frac{n}{N^{(\cdot)}}\right)^{-1} \quad , \tag{136}$$

which corresponds to a slope of -6.02 dB per octave. We can use Eq. (133) to yield the behavior of $|\hat{\phi}_{0\ell}(n/N^{(\cdot)}\Delta)|_{env}$ *for small* $n/N^{(\cdot)}$

$$|\hat{\phi}_{0\ell}(n/N^{(\cdot)}\Delta)|_{env} \sim \frac{\pi^\ell(2\ell+1)^{\frac{1}{2}}}{[1\cdot3\cdot5\cdots(2\ell+1)]}\left(\frac{L}{\Delta}\right)^\ell\left(\frac{n}{N^{(\cdot)}}\right)^\ell \quad . \tag{137}$$

The breakpoint for spur gears $(n/N^{(\cdot)})_{bp}$ is obtained by equating the right-hand sides of Eqs. (136) and (137) and solving for $n/N^{(\cdot)}$.

$$\left(\frac{n}{N^{(\cdot)}}\right)_{bp} = \frac{[1\cdot3\cdot5\cdots(2\ell+1)]^{\frac{1}{1+\ell}}}{\pi(L/\Delta)} \quad , \tag{138}$$

which is used to divide the regions of application of Eqs. (136) and (137).

We may solve for the maximum value of the envelope $|\hat{\phi}_{0\ell}(n/N^{(\cdot)}\Delta)|_{env\ max}$ by evaluating Eq. (136) or Eq. (137) at $(n/N^{(\cdot)}) = (n/N^{(\cdot)})_{bp}$:

$$|\hat{\phi}_{0\ell}(n/N^{(\cdot)}\Delta)|_{env\ max} = \frac{(2\ell+1)^{\frac{1}{2}}}{[1\cdot3\cdot5\cdots(2\ell+1)]^{1/(1+\ell)}} \tag{139}$$

which is independent of L/Δ. Table III shows the dependence of $(n/N^{(\cdot)})_{bp}$ on ℓ computed from Eq. (138) and lists values $|\hat{\phi}_{0\ell}(n/N^{(\cdot)}{}_{bp}\Delta)|_{env\ max}$ computed from Eq. (139). We

TABLE III. - ENVELOPE BREAKPOINT POSITIONS AND MAXIMA FOR SPUR GEAR MESH TRANSFER FUNCTIONS

ℓ	0	1	2	4	8	16	32
$\frac{\pi L}{\Delta}\left(\frac{n}{N^{(\cdot)}}\right)_{bp}$	1	1.73	2.47	3.94	6.88	12.76	24.54
$\lvert\hat{\phi}_{0\ell}(n/N^{(\cdot)}\Delta)\rvert_{env\ max}$	1	1	0.907	0.762	0.599	0.45	0.329

see from the table that for any fixed value of L/Δ the breakpoint value of $n/N^{(\cdot)}$ increases monotonically with ℓ while the value of the envelope maximum decreases monotonically with ℓ.

Since the magnitude of the first term in Eq. (88) given by the expression preceding Eq. (132) has the form of the product of two terms each having the form of the expression preceding Eq. (136), it follows from the behavior shown in Table 3 that in the case of helical gears the maximum value of the envelope of $|\hat{\phi}_{k\ell}(n/N^{(\cdot)}\Delta)|$ will generally decrease monotonically in both k and ℓ and is strictly bounded above by the values shown in the table where ℓ should be replaced in this interpretation by the larger value of k or ℓ.

APPENDIX A: APPROXIMATE TRUNCATION ERRORS IN EXPANSION OF RECIPROCAL MESH STIFFNESS

In Appendix F of Ref. 1, an expression, Eq. (F12), was derived for the approximation $K_{TM}^{-1}(x)$ of the reciprocal mesh stiffness $K_T^{-1}(x)$ defined in Eq. (F3) of that reference:

$$K^{-1}(x) = \frac{1}{\bar{K}_T[1+\delta K_T(x)/\bar{K}_T]} \quad . \tag{A1}$$

From Eqs. (F1) to (F12) of Ref. 1, it follows that the approximation $K_{TM}^{-1}(x)$ can be expressed as

$$K_{TM}^{-1}(x) = \left(\bar{K}_T\right)^{-1} \sum_{m=0}^{M} [-\delta K_T(x)/\bar{K}_T]^m \quad . \tag{A2}$$

The metric of error that we shall use is the fractional error in our estimate $K_{TM}^{-1}(x)$ of $K_T^{-1}(x)$. According to Eqs. (A1) and (A2), this fractional error can be expressed as

$$\frac{K_T^{-1}-K_{TM}^{-1}}{K_T^{-1}} = 1 - \left\{[1+(\delta K_T/\bar{K}_T)]\left[\sum_{m=0}^{M} (-\delta K_T/\bar{K}_T)^m\right]\right\} \quad , \tag{A3}$$

which is a function only of $\delta K_T/\bar{K}_T$ and M. To a first approximation, $K_T(x)$ is proportional to the number of teeth in contact, where the proportionality constant is the stiffness of one tooth. Furthermore, to a first approximation, we may assume that the number of teeth in contact fluctuates by one tooth — i.e., fluctuates by plus and minus one-half about the mean number of teeth in contact. Hence, we may approximate the *magnitude* of $\delta K_T/\bar{K}_T$ by

$$\frac{\delta K_T}{\bar{K}_T} \approx \frac{1/2}{\text{contact ratio}} \quad , \tag{A4}$$

where, here, the contact ratio is interpreted as the mean number of teeth in contact. Table 1 was computed as a function of M and the contact ratio by combining Eqs. (A3) and (A4).

APPENDIX B: DOMINANT TERM IN SUMMATION IN EQ. (77)

Since the numerator of each term in the summation in Eq. (77) is a sine function, the magnitude of the overall numerator for a given value of n is very sensitive to the values of L/Δ and $FL/A\Delta$ – but always must fall between zero and unity. Thus, to determine the most important term in the summation for general values of L/Δ and $FL/A\Delta$, we shall consider only the denominator $D(n')$ of a typical term – i.e.,

$$D(n') \triangleq (\pi FL/A\Delta)^2(\pi L/\Delta)^2[n'(n-n')]^2. \tag{B1}$$

Differentiating Eq. (B1) with respect to n' and setting the resulting expression equal to zero yields three stationary points of $D(n')$, which fall at values of $n' = 0$, $n/2$, and n. Evaluating the second derivative of $D(n')$ at these three values of n' shows that $D(0)$ and $D(n)$ are minima, and that $D(n/2)$ is a maximum point. Therefore, maximum values of $[D(n')]^{-1}$ occur at $n' = 0$ and $n' = n$. However, from Eq. (77) we see that the term $n' = 0$ is excluded from the summation; hence, for a general range of values of L/Δ and $FL/A\Delta$, we conclude that the dominant term in the summation is the term $n' = n$.

REFERENCES

1. Mark, W.D.: Analysis of the Vibratory Excitation of Gear Systems: Basic Theory. J. Acoust. Soc. Am. 63, 1978, pp. 1409-1430.

2. Rainville, E.D.; Special Functions. MacMillan (New York), 1960.

3. Erdelyi, A.; Magnus, W.; and Oberhettinger, F.; Tables of Integral Transforms, Vol. I. McGraw-Hill (New York), 1954.

4. Arbramowitz, M.; and Stegun, I.A.; Handbook of Mathematical Functions with Formulas, Graphs, and Mathematical Tables. U.S. Government Printing Office (Washington, D.C.), 1964.

5. Buckingham, E.; Analytical Mechanics of Gears. McGraw-Hill (New York), 1949; republished by Dover (New York), 1963.

6. Merritt, H.E.; Gear Engineering. Halsted-Wiley (New York), 1971.

7. Furrow, R.W.; and Mabie, H.H.: The Measurement of Static Deflection in Spur Gear Teeth. Int. Mechanisms 5, 1970, pp. 147-168.

8. Hayashi, K.: Load Distribution on the Contact Line of Helical Gear Teeth. Bull. of Jap. Soc. Mech. Engnrs. 6, 1963; Part I: pp. 336-343; Part II: pp. 344-353.

9. Umezawa, K.: The Meshing Test on Helical Gears Under Load Transmission. Bull. of Jap. Soc. Mech. Engrs. 15, 1972, pp. 1632-1639.

10. Umezawa, K.; and Shikawa, J.I.: Deflection due to Contact Between Gear Teeth of Finite Width. Bull. Jap. Soc. Mech. Engnrs. 16, 1973, pp. 1085-1093.

11. Niemann, G.; and Unterberger, M.: Geräuschminderung bei Zahnrädenn. Verein Deutschen Ingenieure Zeitschrift 101, 1959, pp. 201-212.

12. Sheddon, I.N.; Special Functions of Mathematical Physics and Chemistry. Oliver and Boyd (Edinburgh and London), 1961.

13. Michalec, G.W.; Precision Gearing: Theory and Practice. Wiley (New York), 1966.

14. Crandall, S.H.; and Mark, W.D.; Random Vibration in Mechanical Systems, Academic Press (New York), 1963.

15. Bendat, J.S.; and Piersol, A.G.; Random Data: Analysis and Measurement Procedures. Wiley-Interscience (New York), 1971.

16. Woodward, P.M.; Probability and Information Theory with Applications to Radar. Second ed. Pergamon Press (Oxford), 1964.

17. Cooley, J.W.; Lewis, P.A.; and Welch, P.D.: The Finite Fourier Transform. IEEE Trans. Audio Electroacoustic. AU-17, 1969, pp. 77-85.

18. Kohler, H.K.; Pratt, A.; and Thompson, A.M.: Dynamics and Noise of Parallel-Axis Gearing. Proc. Inst. Mech. Eng. 184, 1969-1970, pp. 111-121.

19. Tsien, H.S.; Engineering Cybernetics. McGraw-Hill (New York), 1954.